Numerical modelling of local scour in rivers using Fluent 6.2

by

Margaret Cunninghame

A thesis submitted in partial fulfilment of the requirements for the degree of Master of Science in Engineering

Department of Civil Engineering
University of Cape Town

August 2005

Declaration

I, Margaret Cunninghame, understand the meaning of plagiarism and declare that all work in this dissertation, save for that which is properly acknowledged, is my own. Neither the whole work nor any part of it has been, or is to be submitted for another degree at this or any other university.

I empower the University of Cape Town to reproduce for the purpose of research the contents as a whole or in part in any manner whatsoever.

Margaret Cunninghame

30 - 08 - 2005

Date

Acknowledgements

I wish to thank the following for their support:

i) Associate Professor Neil Armitage for guidance

ii) Dr Chris Meyer for support in numerical modelling

iii) Danie de Kock for his patience and continued assistance with the use of Fluent software

iv) Prof. Willi Hager and Jens Unger for making available physical model data

v) The Harry Crossley Foundation for financial support

vi) My family for their support. Thank you to my father for proofreading this dissertation.

vii) Denton Smith, Alamgir Kabir, Benjamin Abban, Rukshani Heiyantuduwa, Nic Gibson and Case Bakker for their friendship and encouragement

Terms of Reference

This dissertation documents an investigation into the prediction of local scour around engineering structures in open channels using a three-dimensional numerical model. The computational fluid dynamics software Fluent V 6.1 and V 6.2 is employed for numerical modelling and the results are compared to those from small-scale physical models.

The study was commissioned by Associate Professor Neil Armitage in December 2004 and this dissertation is to be submitted by 31 August 2005.

Abstract

Scour and deposition are natural processes which take place in a river as the stream profile adjusts to changing flow rates, sediment loads and other environmental conditions. Man-made obstacles to the stream flow such as bridge piers and abutments and other hydraulic structures alter flow patterns causing local scouring and deposition. Excessive scour undermines the foundations of bridges and other fluvial structures which may ultimately cause their collapse.

Reliable methods are needed to model the complex flow features at bridge piers and abutments and hence predict the associated patterns of local scour. Empirical formulae are notoriously inconsistent in their predictions of local scour depth (Johnson, 1995) while physical modelling is time-consuming and therefore expensive.

Numerical modelling using Computational Fluid Dynamics (CFD) may offer an economical and reliable approach to scour depth estimation. Some development of these numerical models is, however, necessary before they can be used with confidence. The development of models capable of simulating, inter alia, three-dimensional flow with a free surface and scour hole development is still required. The general finite-volume CFD code Fluent 6.2 was applied to modelling flow and clear-water local scouring of uniform quartzitic sand at circular piers, a rectangular abutment and a semi-circular abutment. Scour and deposition were quantified using the Movability Number (Liu, 1957) and unit stream power approach (Armitage, 2002; Rooseboom, 1992).

Three-dimensional, steady state models were implemented in Fluent 6.2. The two-equation k-ε model was applied for turbulent closure as it offers a compromise between accuracy and computational cost and has been widely validated and applied to the numerical modelling of local scour (e.g. Nagata *et al.*, 2002; Olsen & Melaaen, 1993; Richardson & Panchang, 1998; Salehi Neyshabouri *et al.*, 2003). The Volume of Fluid (VOF) method was adopted for free surface tracking.

The initiation of sediment motion at a circular pier (Midgely, 2000) and rectangular abutment (Mitchell, 2000) was modelled. The numerical model predicted all the pertinent flow features at the pier such as downflow and the formation of a bow wave at the upstream face of the pier, flow separation and eddying in the pier wake and the initial development of the horseshoe vortex. The computed flow field around the rectangular abutment also appeared realistic although only eddying in the horizontal plane was clearly evident. The development of the downflow and formation of the principal vortex were not clear.

The numerical model indicated that scouring would commence at the pier sides, which is consistent with the theory of Breusers & Raudkivi (1991) and Raudkivi (1998). The shape of the region affected by scouring at the abutment compared fairly well to the that measured in the physical model (Mitchell, 2000) and an earlier numerical model (McGahey, 2001), however the extent of the scoured region was overestimated. It is suggested that the numerical model exaggerates the effects of the flow constriction caused by the abutment.

Flow in a developed scour hole at a semi-circular abutment (Unger & Hager, 2005) was simulated using the scour hole bathymetry measured in the physical model. As in the numerical models for incipient motion, the computed flow patterns appeared realistic from a qualitative point of view. The model shows the formation of a horseshoe vortex in the scour hole and associated helical flow patterns, which are key flow features required for the development of local scour holes. Although flow features were well replicated by the numerical model, the unit stream power model gave a poor prediction of scouring at the semi-circular abutment.

A model for local scour hole development at a circular pier, using incremental bed adjustment according to the unit stream power approach, was investigated. The flow field was computed by the numerical model and the scour and deposition calculated manually according to the stream power applied at the channel bed. Nodes on the channel bed were then moved vertically to create a deformed boundary to simulate the developing scour hole measured in a physical model by Ahmed (1995). This adjustment process was repeated for

six iterations. The scour hole initially developed at the pier sides and then migrated upstream around the upstream face of the pier as described in theory by Raudkivi (1998).

From this manual bed adjustment model it was concluded that automated procedures to simulate temporal scour hole development are required as bed manual adjustment is very tedious. The magnitude of bed deformation permitted at each adjustment must be limited to avoid generation of scour holes with unrealistically steep sides exceeding the angle of repose of the sediment.

Further research is required in the implementation of the unit stream power approach in numerical models for local scour prediction as the stream power computed at the circular pier of Ahmed (1995) and semi-circular abutment (Unger & Hager, 2005) was unrealistically low. Development of automated procedures for channel boundary adjustment to simulate temporal local scour hole evolution is required. Alternative formulations for the slope correction, which is implemented in deforming bed models, also require investigation.

Contents

List of Tables

List of Figures

Notation

Symbol	Unit	Description
a	m	Longest triaxial dimension of sediment particle
A	m^2	Cross-sectional area of channel
A_x	m^2	Boundary face area projected in the x-direction
A_y	m^2	Boundary face area projected in the y-direction
A_z	m^2	Boundary face area projected in the z-direction
b	m	Intermediate triaxial dimension of sediment particle
B	m	Channel width
B_r	-	Constant in log-law for velocity in the boundary layer
B_s	-	Standardised roughness constant in log-law for velocity
c	m	Shortest triaxial dimension of sediment particle
C_D	-	Drag coefficient
$C_{1\varepsilon}$	-	Constant in k-ε turbulence model
$C_{2\varepsilon}$	-	Constant in k-ε turbulence model
$C_{3\varepsilon}$	-	Constant in k-ε turbulence model
C_μ	-	Constant in k-ε turbulence model
C_{scour}	m^4/W	Relaxation factor for scour in bed adjustment model
C_{depo}	m^4/W	Relaxation factor for deposition in bed adjustment model
d	m	Dimension of sediment particle
d_p	m	Pier diameter
dx	m	Dimension of control volume in x-direction
dy	m	Dimension of control volume in y-direction
dz	m	Dimension of control volume in z-direction
d_{XX}	m	Sieve size through which XX% of particles pass by mass
D_*	-	Non-dimensional sediment grain size
Fr	-	Froude Number
F_D	N	Drag force on sediment particle
$F_{D,c,0}$	N	Critical drag force on a particle on a horizontal bed

$F_{D,c,\beta}$	N	Critical drag force on a particle on a longitudinal slope β
$F_{D,c,\gamma}$	N	Critical drag force on a particle on a transverse slope γ
F_L	N	Lift force on a sediment particle
F_R	N	Frictional resisting force on a sediment particle
g	m/s^2	Gravitational acceleration scalar
$\mathbf{g}$	m/s^2	Gravitational acceleration vector
G_b	N/s	Generation of k due to mean velocity gradients
G_k	N/s	Generation of k due to buoyancy
h	m	Flow depth
i	J/kg	Internal energy
I	s^{-1}	Intensity of particle motion
k	m^2/s^2	Turbulent kinetic energy
k_T	W/mK	Conduction coefficient
k_s	m	Roughness height
k_s^+	-	Dimensionless roughness height
k_β	-	Correction factor for longitudinal bed slope
k_γ	-	Correction factor for transverse bed slope
K	-	Constant in Bagnold's (1966) stream power model
L	m	Length scale in k-L turbulence model
L_a	m	Abutment length (in z-direction)
ℓ	m	Mixing length in Prandtl model
m	-	Number of particles displaced from a unit area
Mn	-	Movability Number
$Mn_{c,0}$	-	Critical Mn on horizontal channel bed
$Mn_{c,\beta\gamma}$	-	Critical Mn on bed with longitudinal slope angle β and transverse slope angle γ
n	-	Number of surface particles on a unit area
$\mathbf{n}$	m	Vector normal to the channel bed
n_x	m	Component of $\mathbf{n}$ in x-direction
n_y	m	Component of $\mathbf{n}$ in y-direction
n_z	m	Component of $\mathbf{n}$ in z-direction
p	N/m^2	Pressure
P	m	Wetted perimeter

P_i	W/m^3	Potential energy released by water flowing downhill
P_r	W/m^3	Unit stream power required for particle suspension
P_t	W/m^3	Applied unit stream power
$P_{t(l)}$	W/m^3	Applied stream power in smooth boundary
$P_{t(t)}$	W/m^3	Applied stream power in rough boundary
$P_{t,c,0}$	-	Critical P_t on horizontal channel bed
$P_{t,c,\beta\gamma}$	-	Critical P_t on bed with longitudinal slope angle β and transverse slope angle γ
q	m^2/s	Unit flow rate ($= Q / B$)
q_b	N/ms	Bed load transport rate per unit width
Q	m^3/s	Flow rate
R	m	Hydraulic radius ($= A / P$)
Re	-	Flow Reynolds Number
Re_s	-	Reynolds Number for a settling sediment particle
Re_*	-	Particle Reynolds Number
S	-	Average slope
S_0	m/m	Channel bed slope
S_{Mi}	N/m^3	Momentum source term in i-direction
S_i	J/m^{3}s	Energy source term
S_k	N/s	Source term in transport of k
S_ε	N/s	Source term in transport of ε
S_φ	-	Source term for φ
SF	-	Shape factor for sediment particles
t	s	Time
$\mathbf{t}$	m	Transverse vector
t_x	m	Component of $\mathbf{t}$ in x-direction
t_y	m	Component of $\mathbf{t}$ in y-direction
t_z	m	Component of $\mathbf{t}$ in z-direction
T	°C, K	Temperature
u	m/s	Velocity component in the x-direction
u_i	m/s	Velocity component in the i-direction
$\mathbf{u}$	m/s	Velocity vector
$\overline{u}$	m/s	Time-averaged component of u

u'	m/s	Fluctuating component of u
u_*	m/s	Shear or friction velocity
u^+	-	Dimensionless velocity
u_c	m/s	Critical velocity for incipient motion
U	m/s	Velocity magnitude or mean velocity magnitude
v	m/s	Velocity component in the y-direction
v_{max}	m/s	Maximum downflow velocity at pier or abutment
v_{ss}	m/s	Particle settling velocity
w	m/s	Velocity component in the z-direction
W_0	W/m	Rate of potential energy loss of the flow
W_c	W/m	Critical flow power for incipience in Bagnold's model
W_s	N	Submerged weight of sediment particle
x	m	Streamwise / longitudinal / mean flow direction
x_i	m	Co-ordinate in i-direction
y	m	Vertical / flow depth direction
y^+	-	Dimensionless depth
y_0	m	Depth at which velocity is mathematically equal to zero
y_s	m	Scour depth
Y	J/kg	Potential energy per unit weight of water
Y_M	N/s	Source term in transport of k
z	m	Transverse direction
z_0	m	Distance from channel wall to point where velocity is zero
α	degrees	Arbitrary slope angle
β	degrees	Longitudinal bed slope angle
δ_{ij}	-	Kronecker Delta
Δy	m	Bed adjustment
ε	m^2/s^3	Rate of viscous dissipation
ϕ	degrees	Angle of repose of sediment particle
Φ	W/m^3	Power dissipation function
γ	degrees	Transverse bed slope angle
Γ	-	Diffusion coefficient for transport of φ
η	-	Fraction of P_r required for incipience
η_l	-	Fraction of P_r required for incipience in smooth boundaries

η_t	-	Fraction of P_r required for incipience in rough boundaries
φ	-	Arbitrary scalar quantity
$\overline{\varphi}$	-	Time-averaged component of φ
φ'	-	Fluctuating component of φ
κ	-	Von Karman coefficient
λ	-	Coefficient of bulk viscosity
θ	-	Shields parameter or Shields stress
θ_c	-	Critical Shields parameter
μ	Ns/m^2	Total dynamic viscosity ($= \mu_l + \mu_t$)
μ_l	Ns/m^2	Laminar dynamic viscosity
μ_t	Ns/m^2	Turbulent dynamic viscosity
ν	m^2/s	Total kinematic viscosity of water
ρ	kg/m^3	Density of water
ρ_a	kg/m^3	Density of air
ρ_s	kg/m^3	Density of sediment
σ_g	-	Standard deviation of sediment size distribution
σ_k	-	Turbulent Prandtl number for k
σ_ε	-	Turbulent Prandtl number for ε
τ	N/m^2	Shear stress
τ_o	N/m^2	Shear stress on the channel bed
τ_c	N/m^2	Critical shear stress
τ_{ij}	N/m^2	τ in the i-direction on a plane normal to the j-direction
τ_l	N/m^2	Laminar component of total shear stress τ
τ_t	N/m^2	Turbulent component of total shear stress τ
Ω	W/m^3	Scour potential in terms of stream power
Ω_{scour}	W/m^3	Scour potential above which scour occurs
Ω_{depo}	W/m^3	Scour potential below which deposition occurs
ω	s^{-1}	Dissipation per unit kinetic energy ($= \varepsilon / k$)
ψ	-	Slope correction factor

Abbreviations

2D	Two-dimensional
3D	Three-dimensional
ASM	Algebraic Stress Model
CFD	Computational Fluid Dynamics
DES	Detached Eddy Simulation
DNS	Direct Numerical Simulation
FSM	Fractional Step Method; a pressure-velocity coupling method
k- ε	Two-equation turbulence model computing turbulent kinetic energy k and dissipation rate ε
k- L	Two-equation turbulence model computing k and length scale L
k- ω	Two-equation turbulence model computing k and dissipation per unit kinetic energy ω
LES	Large Eddy Simulation
PDE	Partial differential equation
PISO	A pressure-velocity coupling commonly used in transient simulations
PRESTO	Pressure interpolation scheme based on a staggered grid technique
QUICK	A quadratic upwind discretisation scheme
RANS	Reynolds-Averaged Navier-Stokes (equations)
RNG	Renormalisation Group method
RSM	Reynolds Stress Model
SIMPLE	A pressure-velocity coupling method
SIMPLEC	A pressure-velocity coupling method
SST	Shear stress transport k- ω model
VLES	Very Large Eddy Simulation
VOF	Volume of Fluid method for free surface tracking

Chapter 1
Introduction

Scour and deposition are natural processes that take place in rivers as the profile of a stream adjusts to changing flow rates, sediment loads and other environmental conditions. Human interference such as the construction of bridges, weirs, river training works and other fluvial structures may induce scouring and deposition by changing flow patterns.

Local scour occurs as a result of the formation of three-dimensional flow patterns and vortices at obstacles in rivers. Local scouring at obstacles such as bridge piers and abutments endangers the structural integrity of road, rail and pipe bridges over rivers as excessive scour undermines foundations ultimately causing the structure to collapse. In a recent survey of scour problems at South African road bridges, Armitage *et al.* (2005) found that local scour was the most prevalent mechanism of scour damage as it was evident at 60 % of the 121 bridges investigated. This study also indicated that local scour is very difficult to observe and measure particularly under extreme flood conditions. It is, however, these conditions which are of greatest concern to engineers as catastrophic bridge failures occur during large floods. Furthermore, the recurrent failure of vital transport links such as the N2 route though KwaZulu-Natal causes substantial economic losses.

Reliable methods are needed to predict the complex patterns of fluid flow around obstacles such as bridge piers and abutments and hence the associated local scouring. Empirical formulae for predicting scour depths are notoriously inconsistent and each has a limited range of application for which the formula was calibrated (Johnson, 1995). There is no universally-accepted procedure for calculating local scour depths. Physical modelling using scale models in the laboratory is time-consuming and expensive.

Numerical models for local scour prediction have undergone rapid development in the past two decades and may in the future offer a reliable alternative to physical modelling and empirical formulae for scour prediction. Once a working model has been developed sensitivity analyses can be carried out with little additional effort. In addition, numerical

models are ideal for simulating hazardous environments such as the scour occurring during large floods when it is too dangerous to make field measurements (Versteeg & Malalsekera, 1995).

McGahey (2001) investigated a Computational Fluid Dynamics (CFD) model for local scour at a weir, cylindrical pier and rectangular abutment based on the unit stream power approach and concluded that CFD shows potential as a tool for predicting local scour. McGahey simulated steady flow around piers and abutments on flat channel beds and around piers at which equilibrium scour holes had developed. A moving lid boundary was employed to represent the free surface. It was recognised that a better free surface routine was needed to account correctly for the pressure variations associated with three-dimensional flow around the obstacles. Furthermore, McGahey (2001) indicated that the model required further development to simulate temporal development of local scour holes using an automated procedure.

More sophisticated pre-processors and solvers combined with increased computing power now facilitate simulation of free surface flow with relative ease. There are also many options available for simulating deformation of the channel bed over time in the modelling of scour and deposition.

The objective of this study was to investigate the capability of the commercial CFD code Fluent 6.2 to simulate free surface flow around piers and abutments, and to model the development of local scour holes according to the unit stream power approach. The following were to be investigated qualitatively and, where possible, quantitatively:

- The effects of employing a multiphase model, which simulates the stratified flow of air and water to represent free surface flow, on river flow patterns and hence the initiation of local scouring on flat channel beds at piers and abutments.

- The performance of this free surface model in predicting realistic flow patterns in developed clear-water scour holes.

- The capabilities of the CFD code to simulate temporal development of a local scour hole from a flat channel bed to an equilibrium clear-water scour hole according to the unit stream power approach. Emphasis was placed on the exploratory development of a bed deformation model rather than a rigorous analysis of the model's performance.

Numerical simulations were carried out using the three-dimensional finite volume CFD code Fluent 6.2. Clear-water local scour of cohesionless quartzitic sand at circular cylinders, a semi-circular abutment and a rectangular abutment was investigated. The numerical output was compared to small-scale physical models (Ahmed, 1995; Midgely, 2000; Mitchell, 2000; Unger & Hager, 2005). The k-ε model was employed for turbulent closure and the Volume of Fluid (VOF) method was used for free surface tracking. Scour potential was assessed in terms of the Movability Number (Liu, 1957) and unit stream power approach (Armitage, 2002).

Manual bed adjustment was performed according to the applied stream power computed by the numerical model. The bed deformation used to simulate scour and deposition was calculated as a function of the scour potential on the channel bed.

This dissertation is structured as follows:

Chapter 2 gives a brief overview of the relevant characteristics of open channel flow and sediment transport theory including sediment properties, incipient sediment motion, mechanisms of particle motion and classification of the different types of scour. The Movability Number (Liu, 1957) and unit stream power approach (Armitage, 2002; Rooseboom, 1992; Yang & Song, 1979) are introduced as models for predicting incipient motion. Flow patterns and the temporal development of clear-water local scour holes at circular piers and rectangular abutments in open channels are discussed. The development of key features of the flow which influence scour hole development are addressed. Limitations of the empirical formulae commonly used to estimate local scour depths are highlighted and the need for reliable and consistent numerical models is emphasised.

The theoretical background to Computational Fluid Dynamics (CFD) modelling of fluid flow is discussed in Chapter 3. The Navier-Stokes equations governing fluid flow are

presented and the three-dimensional unit stream power equation is placed in the context of the energy equation. Options for simulating turbulence in open channels and methods for tracking the interface between two moving fluids in stratified or free surface flows are discussed. Past work in numerical modelling of local scour is reviewed.

In Chapter 4, the methods employed to model local scour in this study are discussed. The physical models, which were simulated numerically, are described. For the numerical models, the domain geometry and mesh generation, free surface and turbulence models, boundary conditions and solver controls are discussed. The method investigated for manual channel bed adjustment to simulate scour and deposition is also detailed.

Output from the numerical models is presented and evaluated in Chapter 5. The flow patterns and scour predictions are assessed qualitatively and, where possible, compared to more detailed quantitative physical model data. Problems encountered and limitations of the manual channel bed adjustment method are discussed.

The conclusions drawn in this research are presented in Chapter 6.

Chapter 7 gives recommendations for future work in local scour prediction using numerical methods.

Chapter 2
Sediment Transport in Open Channel Flow

The special case of clear-water local scouring at bridge piers and abutments in rivers is placed in the context of general sediment transport theory in this chapter. Pertinent characteristics of sediment particles are reviewed. Mechanisms of sediment motion and scouring at piers and abutments are discussed. Attention is paid to the definition of the threshold of sediment particle motion and quantifying incipience in terms of the Movability Number and unit stream power models used in the numerical model in this study. The development of clear-water local scour holes at piers and abutments is reviewed.

2.1 Characteristics of sediment particles

The following important characteristics of sediment particles are reviewed in this section: particle size and size distribution of sediment mixtures, particle shape, density, settling velocity, angle of repose and cohesion. This study was limited to investigation of non-cohesive, uniform, quartzitic sand and emphasis is therefore placed on characteristics relevant to this type of sediment.

2.1.1 Particle size and sediment size distribution

Size is the most important characteristic of a sediment particle (Chanson, 2004; Vanoni, 1977) and can be used to predict the physical properties of sediment for many practical engineering applications (Yang, 1996). Particle size may be measured according to the sieve diameter, sedimentation diameter, nominal diameter or triaxial dimensions. Details may be found in Chien & Wan (1999), Raudkivi (1998) or Vanoni (1977). Reference is made to the sieve diameter for measurement of particle sizes in this study.

The sieve size passed by 50% of sediment particles by mass, d_{50}, is frequently used as a characteristic sediment particle size (Chanson, 2004) and is adequate for describing narrow grain size distributions (Breusers & Raudkivi, 1991).

The uniformity of sediment may be measured by the geometric standard deviation σ_g based on a log-normal distribution of the grain sizes. Chanson (2004) and Breusers & Raudkivi (1991) define σ_g as follows:

$$\sigma_g = \sqrt{\frac{d_{84.1}}{d_{15.9}}} \tag{2.1}$$

where $d_{84.1}$ and $d_{15.9}$ are the sieve sizes passed by 84.1% and 15.9% of the sediment particles by mass respectively. The grain size distribution may also be represented parameters such as a sorting coefficient, sorting index, uniformity coefficient and effective grain size. Raudkivi (1998) indicates that the sediment may be considered "uniform" from a hydraulic point of view if the following conditions are met:

$$\frac{d_{95}}{d_5} < 5 \tag{2.2}$$

$$\sigma_g < 1.35 \tag{2.3}$$

The effects of armouring on channel bed roughness may thus be disregarded in sediment mixtures satisfying the conditions of Equations 2.2 and 2.3 above.

2.1.2 Particle shape

A shape factor *SF* is commonly used to describe the shape of sediment particles for calculations of the fall velocity (Breusers & Raudkivi, 1991; Vanoni, 1977; Yang, 1996). *SF* is defined as follows:

$$SF = \frac{c}{\sqrt{ab}} \tag{2.4}$$

where the triaxial dimensions a, b and c are, respectively, the longest, intermediate and shortest mutually perpendicular axes of the particle. A sphere has a shape factor of 1.0 and naturally-worn quartz particles typically have $SF \approx 0.7$ (Raudkivi, 1998; Yang, 1996).

There are more complex parameters describing the particle shape such as the *roundness* relating to the sharpness of the particle's edges and *sphericity* which is a ratio of the particle surface area to that of a sphere of equivalent volume. Details may be found in Chien &Wan (1999) and Vanoni (1977).

2.1.3 Particle density

The density of sediment particles depends on their mineral composition. Quartz and feldspar occur most commonly in the mineral composition of sediment and the particle density falls most often in the range $\rho_s = 2600$ to 2700 kg/m^3 (Chien & Wan, 1999). For quartzitic sand, a density of 2650 kg/m^3 is widely published in literature.

2.1.4 Settling velocity

The settling velocity v_{ss} of a sediment particle is the terminal velocity attained by the particle falling in an infinite body of quiescent water. This settling velocity is widely used

as a measure of the particle's response to flow (Yang, 1996) and is employed in the Movability Number model for incipient motion.

At terminal velocity, the downward force exerted on a particle by its submerged weight is equal to the upward fluid drag force. Equating these forces on a sphere, the following expression for v_{ss} is obtained:

$$v_{ss} = \sqrt{\frac{4}{3}\frac{gd}{C_D}\left(\frac{\rho_s}{\rho} - 1\right)} \tag{2.5}$$

where g is gravitational acceleration, d is the particle diameter, ρ is the density of water and C_D is the drag coefficient. C_D is a function of the particle Reynolds Number Re_s and particle shape. If ν is the kinematic viscosity of water, Re_s is defined as follows:

$$Re_s = \frac{v_{ss} d}{\nu} \tag{2.6}$$

The form of the relationship $C_D = f(Re_s)$ depends on whether the flow at the surface of the particle is smooth or rough in terms of boundary later theory (Section 2.4.2). Two relationships proposed for the calculation of C_D based on experimental data for sand and gravel with $Re_s < 10000$ are:

$$C_D = \frac{24}{Re_s} + 1.5 \qquad \text{(Engelund \& Hansen, 1967)} \tag{2.7}$$

$$C_D = \left[\left(\frac{24}{Re_s}\right)^{2/3} + 1\right]^{3/2} \qquad \text{(Cheng, 1997)} \tag{2.8}$$

A typical particle drag coefficient for natural coarse sand and gravel given by Raudkivi (1998) is $C_D \approx 1$ while Chien & Wan (1999) suggest $C_D \approx 1.1$.

The effect of particle shape on v_{ss} may be accounted for in the drag coefficient. Other factors affecting the settling velocity include the presence of boundaries, sediment concentration, fluid viscosity (temperature), turbulence, particle surface roughness and the flocculation of small sediment particles if applicable. Chien & Wan (1999) detail methods to quantify the effects of some of these factors on v_{ss}.

Many empirical equations and curves have been published for estimating settling velocities. Cheng (1997) fitted the following formulae to published data:

$$v_{ss} = \frac{\nu}{d}\left[\left(25 + 1.2D_*^{\,2}\right)^{1/2} - 5\right]^{3/2} \tag{2.9}$$

where the non-dimensional grain size D_* is given by

$$D_* = \left[\frac{(\rho_s - \rho)gd^3}{\rho\nu^2}\right]^{1/3} \tag{2.10}$$

2.1.5 Angle of repose

A sediment particle situated on a slope inclined at an angle α to the horizontal plane will become unstable and roll down the slope when a threshold value of α is reached. This critical slope angle is the angle of repose, ϕ. The angle of repose is an important parameter when considering incipience of sediment motion on a sloping channel bed as particles on a streamwise-sloping bed will move more readily than those situated on an adverse slope.

The angle of repose is a function of the particle shape and increases with angularity. Chanson (2004) indicates that for sand, ϕ is typically between 26° and 34°, while Migniot (1968) found that, for submerged sand, ϕ varies between 31° and 40°.

2.1.6 Cohesion

The motion of non-cohesive or granular sediment grains is governed primarily by the particle size and weight while cohesive sediments are influenced by electro-chemical interactions. Cohesive effects become significant at a clay content of as little as 10% (Breusers & Raudkivi, 1991; Raudkivi, 1998). The remainder of this study is concerned only with the motion of non-cohesive sediments.

2.2 Forces on a sediment particle on the channel bed

Many models for the initiation of sediment motion are initially developed from an analysis of the forces or stresses acting on a submerged sediment particle (Yang, 1996). A cohesionless sediment particle on the channel bed (Figure 2.1) is subjected to drag and lift forces F_D and F_L imparted by the moving fluid. It is also subject to the stabilising forces of its self-weight W_s and a frictional resisting force F_R due to contact with adjacent particles. The particle will move when the disturbing forces or moments about some point O instantaneously exceed the stabilising forces or moments (Raudkivi, 1998).

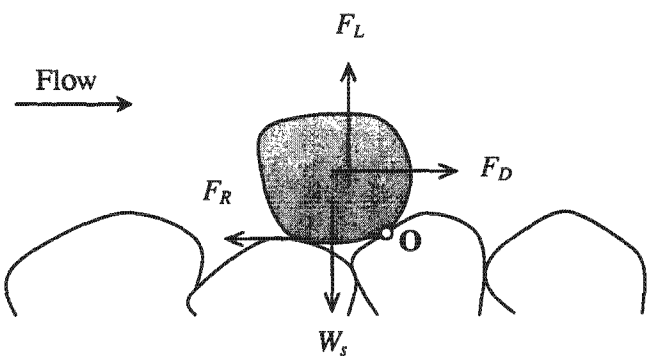

Figure 2.1: Forces acting on a prominent sediment particle on the channel bed

2.3 Concept and nature of incipient sediment motion

Incipient motion is the commencement of sediment motion. When forces imparted by the moving fluid on a sediment particle exceed its resistance to movement, the particle will be set in motion.

Incipient motion of a bed of sediment particles is stochastic in nature. If, for example, shear stress is used to predict incipient motion, the measure of sediment transport is the probability that the bed shear stress applied by the fluid instantaneously exceeds the critical shear stress required to mobilise a sediment particle (Hoffmans & Verheij, 1997). The applied bed shear stress τ_0 fluctuates as properties of the turbulent fluid flow vary in space and time. Similarly, the critical shear stress τ_c required to displace a particle varies as particles have different sizes, shapes, orientations and locations on the channel bed. The shear stresses τ_0 and τ_c can thus be represented by the probability distributions in Figure 2.2. Incipient motion depends on the interaction of the frequency distributions representing these two variables (Chien & Wan, 1999). The figure indicates that incipient motion will occur in the range where the two distributions overlap.

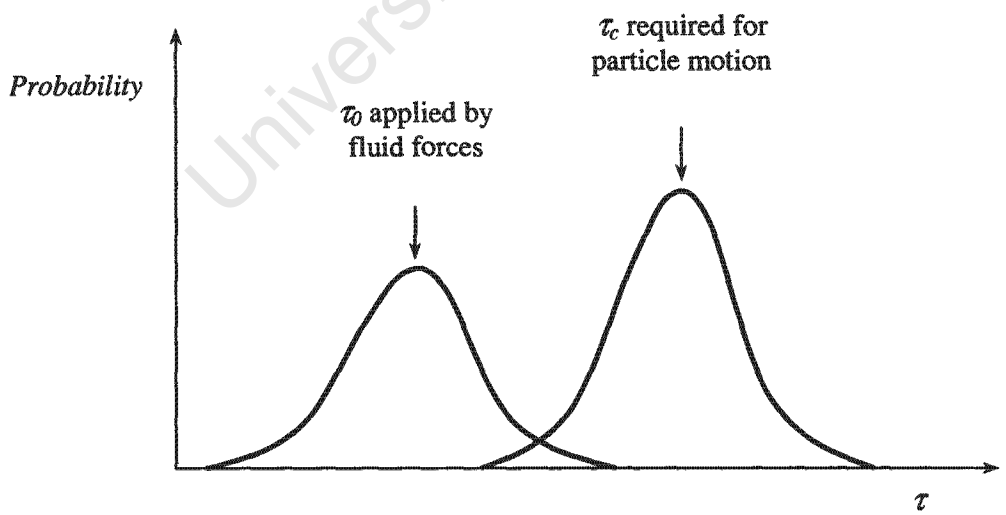

Figure 2.2: Probability distributions for the applied and critical shear stresses (Grass, 1970)

There is theoretically some probability that a particle will be mobilised given any flow conditions. It is, however, only at a certain flow threshold that the intensity of motion becomes significant. If m particles are displaced from a unit area over a time interval t and the unit area contains a total of n surface particles, Shvidchenko & Pender (2000a, 2000b) define the intensity of motion I as:

$$I = \frac{m}{nt} \tag{2.11}$$

Sediment motion may be classified in terms of the intensity of motion as "weak" "intermediate" or "general movement". Alternatively, Chien & Wan (1999) use the terms "sparse", "mean" and "strong" sediment motion. Van Rijn (1993) employs seven categories describing the intensity of motion ranging from "occasional particle movement at some locations" to "general transport and initiation of ripples".

For the purpose of selecting critical values of the Movability Number and unit stream power for incipience (Sections 2.5 and 2.6 respectively), Armitage (2002) defined "weak" sediment motion to be in the order of $I = 10^{-4}$ s^{-1}.

2.4 Common approaches to quantifying incipient motion

According to Chien & Wan (1999), the incipient motion of sediment was originally linked to flow velocity. Subsequent investigations analysed the balance of forces of particles. Shields (1936) later used dimensional analysis to estimate the threshold of motion. Other investigators (Einstein, 1942) then linked theories of probability and fluid mechanics to model the stochastic nature of sediment transport.

Three common parameters used to predict incipient sediment motion: bed shear stress, velocity and stream power are reviewed in this section. The Movability Number and unit stream power approaches adopted in this study are then presented.

2.4.1 Bed shear stress

Bed shear stress is frequently employed as a key variable to link stream flow properties to sediment transport in studies of local scour. Olsen & Melaaen (1993), Olsen & Kjellesvig (1998) and Ali & Karim (2002) employed bed shear stress to compute sediment concentration and hence changes in bed elevation. Nagata *et al.* (2002) incorporated the bed shear stress into a stochastic model for sediment movement at a cylindrical pier.

The distribution of shear stress in open channel flow and the widely used Shields diagram for incipient motion in terms of bed shear stress are reviewed below.

a) Shear stress distribution in open channel flow

In steady, uniform open channel flow, the shear stress τ increases linearly with depth y from zero at the free surface to a maximum of τ_0 at the channel bed as shown in Figure 2.3. If S_0 is a small bed slope and h is the water depth, τ is given by:

$$\tau = \rho g S_0 (h - y) \tag{2.12}$$

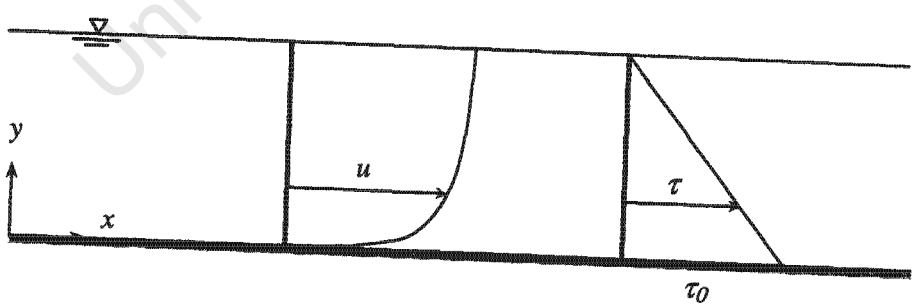

Figure 2.3: Velocity and shear stress in steady uniform two-dimensional flow

The total shear stress τ is comprised of a laminar component τ_l and turbulent component τ_t. Each is related to the shear deformation rate by the respective laminar or turbulent fluid

viscosity, μ_l or μ_t. The total shear stress may therefore be expressed as follows (Yalin, 1972):

$$\tau = \tau_l + \tau_t = (\mu_l + \mu_t)\frac{\partial u}{\partial y} \tag{2.13}$$

The total viscosity μ is the sum of the laminar and turbulent components, thus,

$$\tau = \mu\frac{\partial u}{\partial y} \tag{2.14}$$

Since the velocity gradient is very large near the channel bed and small at the free surface, and μ_l is constant for isothermal flow, τ_l increases rapidly towards the channel bed. The turbulent viscosity μ_t is, however, not constant with depth but is a function of the spatial and temporal turbulent fluctuations in the flow. The distributions of τ_l and τ_t with depth are illustrated schematically in Figure 2.4.

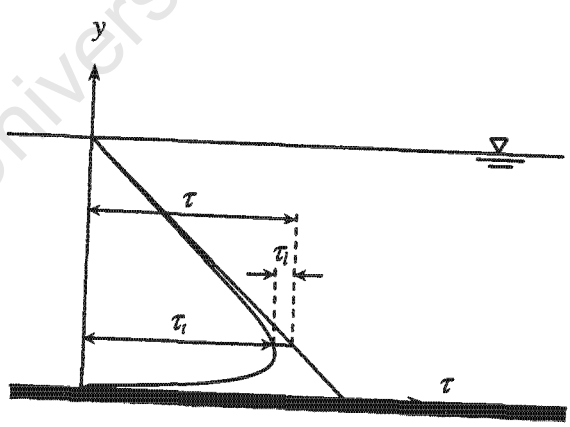

Figure 2.4: Laminar, turbulent and total shear stress in open channel flow

Close to the bed in the viscous sublayer, τ_l dominates as turbulent fluctuations are damped by the presence of the boundary. In the turbulent core of the flow, some distance from the

bed, the contribution of τ_l is negligible and $\tau \approx \tau_t$. A more detailed description of these shear stress distributions in given by Yalin (1972).

Many mathematical models have been proposed to simulate turbulent fluctuations in open channel flow to quantify the turbulent viscosity and hence turbulent shear stress. Two simple approaches, the Reynolds Stress Model and Prandtl Mixing Length Model, are introduced here.

In the Reynolds Stress Model, the instantaneous velocity is conceptualised as being composed of turbulent fluctuations superimposed upon a temporal mean value. The fluctuating velocity components are small relative to the temporal mean velocity (Graf, 1998). The x-component of the instantaneous velocity, u, for example, is the sum of a mean component $\overline{u}$ and fluctuating component u'.

$$u = \overline{u} + u' \tag{2.15}$$

The stress due to the turbulent fluctuations is termed a Reynolds stress and is given by the symmetrical stress tensor τ_{ij}.

$$\tau_{ij} = \rho \overline{u_i' u_j'} \tag{2.16}$$

Prandtl (1925) proposed a simple turbulence model based on the theory governing the molecular motion of gases. Fluid particles are displaced by a mean distance or "mixing length" ℓ perpendicular to the mean flow direction due to turbulent processes (Schlichting & Gersten, 2000). The turbulent viscosity and shear stress are the following:

$$\mu_t = \rho \ell^2 \frac{\partial u}{\partial y} \tag{2.17}$$

$$\tau_t = \rho \ell^2 \left(\frac{\partial u}{\partial y} \right)^2 \tag{2.18}$$

Yalin (1972) notes that ℓ may be interpreted as a quantity proportional to the average size of the macroturbulent eddies in the flow or the displacement of these eddies during turbulent mixing. The variation of ℓ with depth is unknown but may be reduced to a simple proportionality near the boundary:

$$\ell = \kappa y \tag{2.19}$$

where κ is the Von Karman coefficient which is constant and approximately 0.4 in clear, sediment-free water (Versteeg & Malalasekera, 1995; Yalin, 1972). Rooseboom (1992) proposed $\kappa = (1/2\pi)^{0.5}$ and experimental data has indicated values of κ fall between 0.36 and 0.43 in clear water (Hinze, 1962; Yalin, 1972). The value of κ is not constant for sediment-laden flows but depends on the sediment concentration.

The total shear stress according to the Prandtl model is thus

$$\tau = \mu_l \frac{\partial u}{\partial y} + \rho \kappa^2 y^2 \left(\frac{\partial u}{\partial y} \right)^2 \tag{2.20}$$

b) Shields diagram for incipient motion in terms of shear stress

Shields (1936) considered the bed shear stress τ_0, relative particle density $(\rho_s - \rho)$, particle diameter d, kinematic fluid viscosity ν and gravitational acceleration g to be the most important variables governing incipient motion. He then used dimensional analysis to group these variables and generate the Shields diagram (Figure 2.5) relating the dimensionless Shields stress θ to the particle Reynolds Number Re_*.

If a shear velocity u_* is defined at the channel bed as follows:

$$u_* = \sqrt{\frac{\tau_0}{\rho}} \tag{2.21}$$

then the Shields stress θ and particle Reynolds Number Re_* are given by:

$$\theta = \frac{\tau_0}{(\rho_s - \rho)gd_{50}} = \frac{\rho u_*^2}{(\rho_s - \rho)gd_{50}} \tag{2.22}$$

$$Re_* = \frac{u_* d}{\nu} \tag{2.23}$$

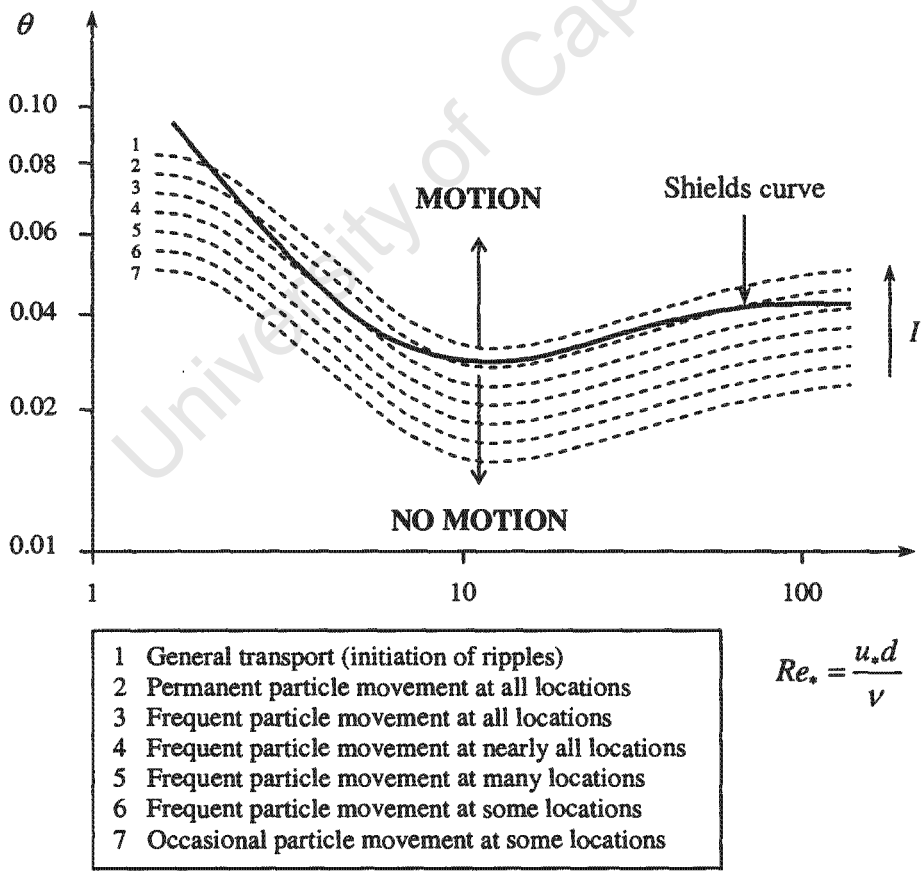

Figure 2.5: Shields diagram with intensities of motion superimposed (Hoffmans & Verheij, 1997; Van Rijn, 1993)

To obtain the critical Shields parameter for incipient motion θ_c, Shields measured decreasing sediment transport rates and extrapolated the results to zero to avoid the need to define critical conditions for incipience (Vanoni, 1977; Raudkivi, 1998). If τ_c is the critical shear stress then θ_c is given by:

$$\theta_c = \frac{\tau_c}{(\rho_s - \rho) g d_{50}} \tag{2.24}$$

The Shields curve corresponds to $I \approx 10^{-2}\ s^{-1}$ (Chien & Wan, 1999) which may be described visually as "permanent / frequent particle movement at all locations".

Although the Shields stress is a widely used parameter for incipient motion, Yang (1973) lists a number of criticisms of the Shields diagram.

Yang (1973) notes that in practice the bed shear stress is often conveniently calculated as $\tau_0 = \rho g h S_0$ which assumes a universal velocity distribution near the bed that is not valid in many instances. Yang also indicates that Shields took only the tangential (drag) force on sediment particles into account in the development of Shields' model and neglected the lift force. Furthermore, Yang suggests that the rate of sediment transport cannot be determined uniquely from the bed shear stress. In addition to Yang's comments above, the Shields diagram is criticised in literature as critical values must be determined by trial and error as the shear velocity u_* appears on both axes.

2.4.2 Flow velocity

Incipient motion may be quantified in terms of flow velocity. The structure of the boundary layer near the channel bed is very important in the prediction of incipience and must therefore be accurately represented in a numerical model. The velocity distribution in turbulent boundary layers and the role of roughness is discussed below. Models for incipient sediment motion in terms of flow velocity are then outlined.

a) Velocity distribution in the turbulent boundary layer

In the region immediately adjacent to the channel bed, viscous forces dominate the flow in the *viscous* or *laminar sublayer*. Further away from the boundary in the *turbulent zone*, viscous effects become small in comparison with inertial forces with increasing distance from the wall. Between these two regions is a *transitional zone*.

The distribution of velocity in the boundary layer is conventionally described in terms of a dimensionless velocity u^+ and depth y^+ which are defined as follows:

$$u^+ = \frac{u}{u_*} \tag{2.25}$$

$$y^+ = \frac{u_* y}{\nu} \tag{2.26}$$

The viscous sublayer is found in the region $0 \leq y^+ < 5$ (Chanson, 2004; Schlichting & Gersten, 2000; Yalin, 1972). In this layer the shear stress is constant and the velocity distribution is linear and may be described in terms of the dimensionless wall units as

$$u^+ = y^+ \tag{2.27}$$

In the turbulent or log-law layer the velocity distribution is logarithmic. By substitution of the wall units from Equations 2.25 and 2.26 into the function for total shear stress presented by Prandtl (Equation 2.20), the following expression for velocity in the turbulent layer may be obtained:

$$u^+ = \frac{1}{\kappa} \ln y^+ + B_r \tag{2.28}$$

The constant B_r depends on the roughness of the boundary. The lower limit of the turbulent sublayer lies between $y^+ = 30$ and $y^+ = 70$ and the upper bound lies at approximately $y^+ = 500$ (Chanson, 2004; Versteeg & Malalasekera, 1995).

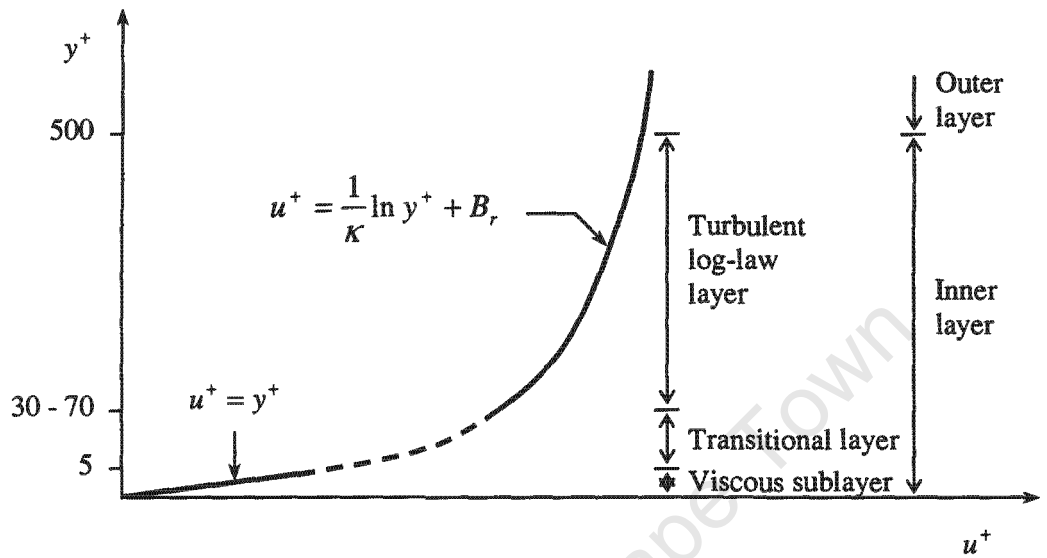

Figure 2.6: Velocity distribution in the turbulent boundary layer (Chanson, 2004; Schlichting & Gersten, 2000; Versteeg & Malalasekera, 1995)

As illustrated in Figure 2.6, between the viscous and turbulent sublayers is a transitional region in which there is no simple mathematical relationship between u^+ and y^+. Schlichting & Gersten (2000) present a "universal law of the wall" based on an indirect turbulence model. This law is valid throughout the inner boundary layer including the transitional region. Alternatively, the transitional region may be ignored and the curves for the viscous and turbulent sublayers, described by Equations 2.27 and 2.28 respectively, extrapolated to an intersection point found between $y^+ = 11$ and $y^+ = 13$ (Rooseboom, 1992; Yalin, 1972). A value of $y^+ \approx 11.8$ for this intersection point is generally accepted (Fluent, 2005; McGahey, 2001; Potter & Wiggert, 1997).

In the outer region where $y^+ > 500$, the velocity varies gradually and is influenced more by the bed slope, maximum flow velocity, flow depth and presence of large scale eddies rather than by viscous effects and wall roughness (Graf, 1998). The velocity distribution in

the outer layer for $0.2 \leq y/h < 1.0$ is still approximately logarithmic as in the turbulent region of the inner boundary layer, but contains modifications to account for the flow depth (Coles, 1956). Details of this "velocity defect law" may be found in Chanson (2004), Graf (1998) and Yalin (1972).

b) Role of bed roughness in boundary layer flows

Incorporation of the effects of bed roughness and bed forms such as ripples and dunes on he flow in the inner boundary layer are crucial in studies of sediment transport. The height of roughness elements on the channel bed relative to the depth of the viscous sublayer determines the velocity distribution near the bed which in turn affects the ability of the flow to mobilise sediment particles.

If the bed roughness height is k_s (Nikuradse, 1933), a dimensionless roughness parameter k_s^+ may be defined as follows:

$$k_s^+ = \frac{u_* k_s}{\nu} \tag{2.29}$$

The flow Reynolds number in a wide channel with mean flow velocity U is given by

$$Re = \frac{Uh}{\nu} \tag{2.30}$$

If Re is so low that the roughness height is small relative to the depth of the viscous sublayer, that is $k_s^+ < 5$, viscous effects dampen the impact of the bed roughness on the flow. In this instance the turbulent boundary layer is effectively flowing over a smooth boundary. This flow regime is shown in Figure 2.7a and is termed *smooth turbulence* (Featherstone & Nalluri, 1995).

At higher values of *Re*, the depth of the viscous sublayer decreases and the roughness elements may protrude into the turbulent zone of the boundary layer, that is $k_s^+ > 70$ (Figure 2.7b). Eddies develop at the boundary as flow separation occurs at the individual roughness elements. In this case, termed *rough turbulence*, the effects of viscosity on the flow are of little importance and the velocity distribution is independent of *Re*. There is, however, difficulty in determining the reference level $y = 0$ at which u is mathematically equal to zero owing to the logarithmic relationship (Schlichting & Gersten, 2000).

Between the smooth and rough turbulent regimes is a *transitional* region where $5 < k_s^+ < 70$.

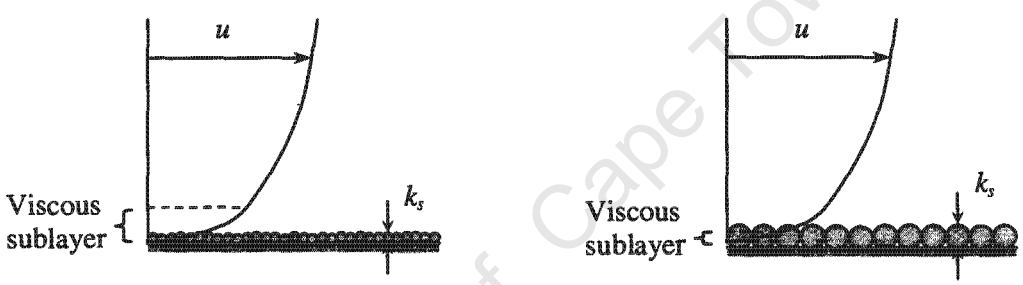

a) Smooth turbulence b) Rough turbulence

Figure 2.7: Relationship between the boundary layer and roughness height in smooth and rough turbulent flow regimes

The constant B_r in the log-law for velocity (Equation 2.28) in the turbulent sublayer is a function of the bed roughness. This log-law was given as:

$$u^+ = \frac{1}{K} \ln y^+ + B_r \tag{2.28}$$

The log-law law may be modified to account for bed roughness as follows:

$$u^+ = \frac{1}{\kappa}\ln\left(\frac{y^+}{k_s^+}\right) + B_s \tag{2.31}$$

The constant B_r in Equation 2.28 is replaced with a related constant B_s denoting a standardised sand roughness. The following relationships between B_s and k_s^+ are presented by Yalin (1972):

For smooth turbulence $B_s = \frac{1}{\kappa}\ln k_s^+ + 5.5$ where $k_s^+ < 5$ (2.32)

For rough turbulence $B_s = 8.5$ where $k_s^+ > 70$ (2.33)

The above relationships are represented graphically in Figure 2.8.

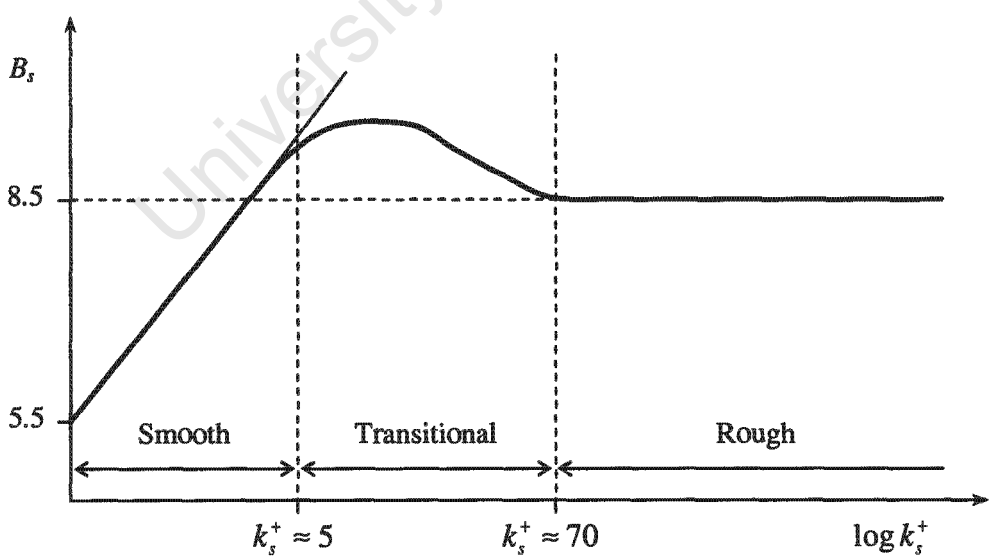

Figure 2.8: Effect of wall roughness on velocity distribution in the turbulent boundary layer (Yalin & Ferreira da Silva, 2001; Yalin, 1972)

c) Incipient sediment motion in terms of flow velocity

The flow velocity to which bed sediment particles are subjected may be used to estimate forces acting on these particles. It is, however, very difficult to measure the velocity near the bed or choose an appropriate depth at which to compute it according to the log-law (Equation 2.28) for example. Hjulstrom (1935) rather related the transportation of uniform sediment to the mean flow velocity as shown in Figure 2.9. Raudkivi (1998), however, notes that the problem with assuming some critical mean velocity is that, for a single mean velocity, the bed shear stress decreases with increasing flow depth.

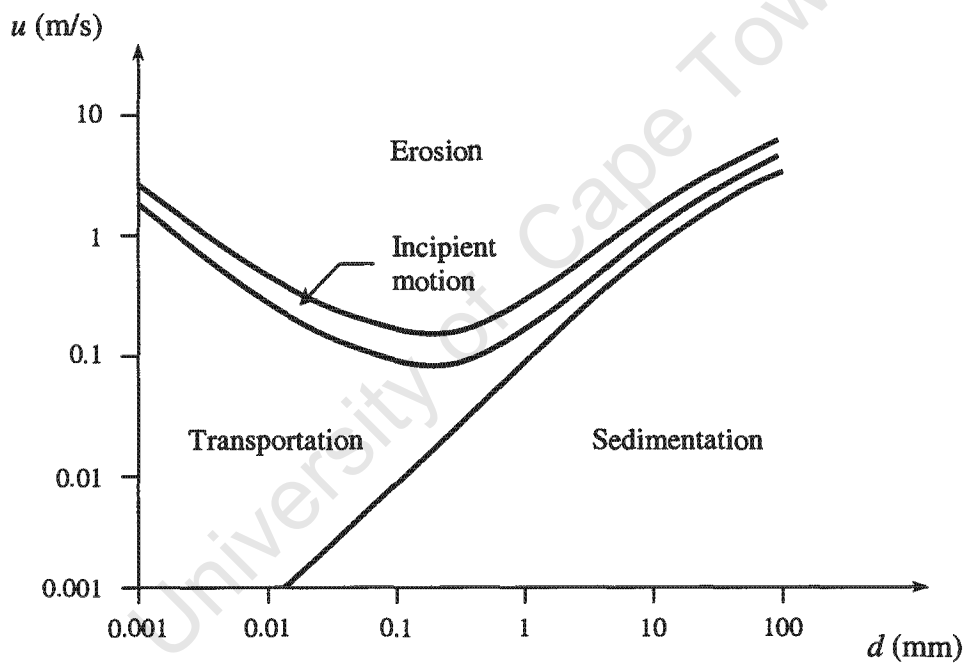

Figure 2.9: Velocity criteria for transport of uniform particles (Hjulstrom, 1935)

Chien & Wan (1999) considered an analysis of forces acting on a particle a more direct approach to incipient motion than the estimation of a mean critical velocity as the latter methods relies on assumptions linking the mean flow velocity to that to which particles on the bed are subjected.

Yang (1973) considered the balance of drag and lift forces, frictional resistance and particle self-weight acting on sediment grains. Yang used the log-law (Equation 2.28) to estimate the local velocity in the vicinity of the sediment particle, integrating this equation over the particle height to obtain a mean velocity near the bed.

From analysis of 153 sets of experimental data, Yang developed the relationship between the ratio of the critical and settling velocities, u_c and v_{ss} respectively, and particle Reynolds Number Re_* shown in Figure 2.10. The relationship is hyperbolic for $Re_* < 70$ and constant for $Re_* > 70$.

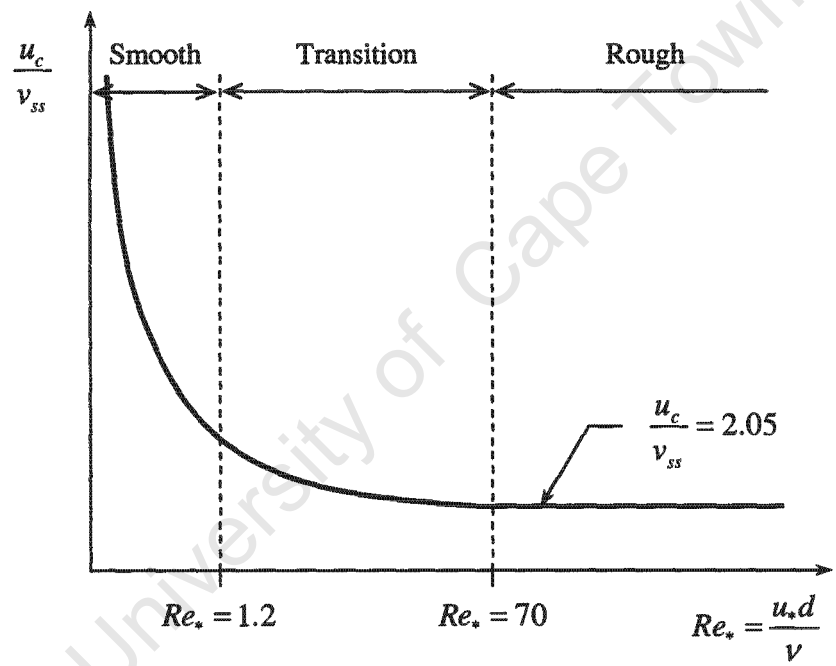

Figure 2.10: Critical velocity for incipient motion according to Yang (1973)

2.4.3 Stream power

To initiate and maintain sediment motion, energy is expended by the flow in doing work on the sediment particles. The intensity of sediment motion may thus be measured by the energy of the flow and that required to mobilise sediment. Bagnold (1966) presented a

stream power model for bedload transport. If q is the unit discharge, the rate at which potential energy is lost by the flow W_0 is

$$W_0 = \rho g q S_0 \tag{2.34}$$

Bagnold analysed experimental data and to find the following relationship between the work done by the flow and the bedload transport rate q_b:

$$\left(\frac{\rho_s}{\rho} - 1\right) g q_b = K(W_0 - W_c) \tag{2.35}$$

where K is a proportionality constant and W_c is the critical flow power required for incipience. The above relationship is illustrated in Figure 2.11.

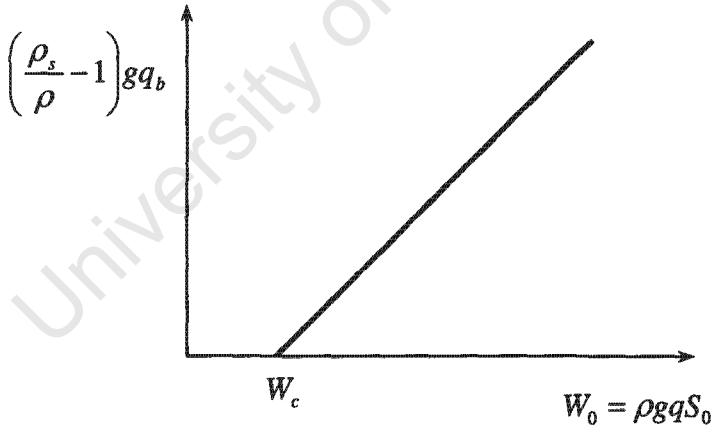

Figure 2.11: Stream power model for bedload transport (Bagnold, 1966)

The weakness of Bagnold's model is that the mean flow velocity is used to compute sediment transport. To measure incipient motion and accurately predict the conditions under which motion commences, a local velocity near the channel bed to which sediment

particles are subjected directly is more appropriate. The unit stream power approach employed in this study (Section 2.6) is based on local rather than mean flow velocities.

2.5 Movability Number for incipient motion

Liu (1957) introduced the Movability Number for prediction of sediment ripple formation. The Movability Number *Mn* is defined as the ratio of the shear velocity to the particle settling velocity.

$$Mn = \frac{u_*}{v_{ss}} \tag{2.36}$$

To quantify incipient motion in terms of *Mn*, Rooseboom (1992) analysed data from Grass (1970) and Yang (1973) and developed the following criteria for incipience:

$$\frac{u_*}{v_{ss}} = \frac{1.6}{Re_*} \quad \text{for smooth boundaries} \tag{2.37}$$

$$\frac{u_*}{v_{ss}} = 0.12 \quad \text{for rough turbulent boundaries} \tag{2.38}$$

Rooseboom (1992) did not attempt to determine critical Movability Number criteria for transitional values of Re_*. The curves for the smooth and rough turbulent regions were simply extrapolated to an intersection point in the transitional region.

Armitage (2002) adopted an approach similar to that of Rooseboom (1992) but analysed data representing the "weak" motion of uniform quartzitic sand in particular. Armitage analysed a large experimental data set containing a total of 529 data points from eight researchers with the objective of linking *Mn* to the intensity of particle motion. This data

fell in the range $3 \times 10^{-6} < I < 3 \times 10^{-4}$. Armitage then described the boundary between scour and deposition as follows:

$$\frac{u_*}{v_{ss}} = \frac{2.2}{Re_*^{1.4}} \quad \text{for smooth boundaries} \tag{2.39}$$

$$\frac{u_*}{v_{ss}} = 0.17 \quad \text{for rough turbulent boundaries} \tag{2.40}$$

Figure 2.12 illustrates the criteria for incipient motion developed by Armitage (2002). The value $Mn = 0.17$ for a rough boundary corresponds to approximately $I = 2 \times 10^{-5}$ s^{-1}. The critical value of Mn for sediment motion is sensitive to the intensity of motion chosen to represent incipience. A 9% increase in Mn increases I by a factor of 10 (Armitage & McGahey, 2003).

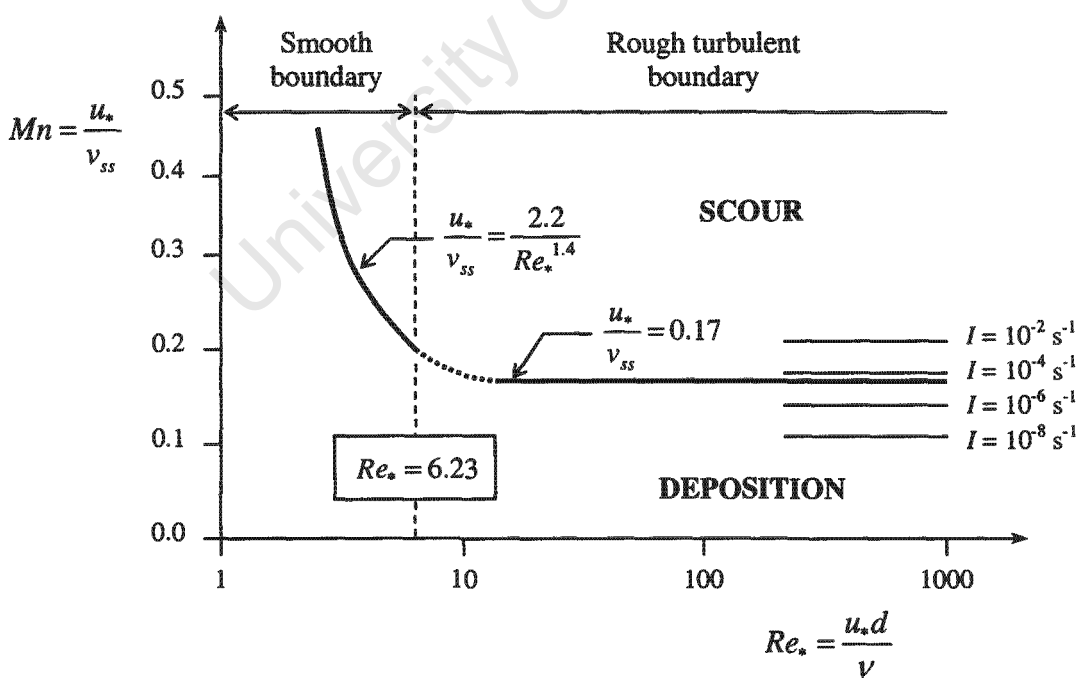

Figure 2.12: Critical Movability Number for incipient motion (Armitage, 2002)

The Movability Number criteria for different modes of particle motion determined by several investigators are presented in Table 2.1.

Table 2.1: Movability Number criteria for sediment particle motion

Reference	Criteria	Nature of sediment motion
Breusers & Raudkivi (1991)	$0.17 < Mn < 0.50$ $0.50 < Mn < 1.4$ $Mn > 1.4$	Bed load Saltation Suspension
Julien (1995)	$Mn > 0.20$ $Mn > 2.5$	Beginning of suspension Suspended load dominates
Graf (1998)	$Mn > 0.10$ $Mn > 0.40$	Beginning of bed load transport Beginning of suspended load transport
Raudkivi (1998)	$0.17 < Mn < 0.50$ $0.50 < Mn < 1.7$ $Mn > 1.7$	Bed load Saltation Suspension
Armitage & McGahey (2003)	$0.12 < Mn < 0.17$ $0.40 < Mn < 0.50$ $Mn > 2.5$	Sliding / rolling commences Suspension commences Suspended load dominates

2.6 Unit stream power model for incipient motion

The principles of conservation of mass, momentum and energy are frequently applied to the solution of hydraulic problems. Similarly, thermodynamic principles may be applied to the prediction of sediment transport by considering the "stream power" available for and dissipated in moving sediment (Yang, 1972; Rooseboom, 1975, 1992). Yang & Stall (1976) proposed that a river adjusts its hydraulic, sediment and geometric properties to achieve a minimum rate of energy dissipation, given by the product of the mean velocity U and average slope S. If Y is the potential energy per unit weight of water, the theory of minimum rate of energy dissipation may be stated as follows (Yang & Song, 1979):

$$\frac{\partial Y}{\partial t} = \frac{\partial x}{\partial t}\frac{\partial Y}{\partial x} = US \tag{2.41}$$

The weakness of such one-dimensional models which link sediment transport to a mean rather than a local velocity have been discussed in previous sections. Rooseboom (1975) developed expressions for the stream power made available through the loss of potential energy by the flow and the variation of power dissipated through shearing action with depth (Figure 2.13). The power input per unit volume, from the potential energy released by water flowing downhill, P_i, and power dissipated through shear, P_t,are given by

$$P_i = \rho g S_0 u \tag{2.42}$$

$$P_t = \tau_{xy}\frac{\partial u}{\partial y} \tag{2.43}$$

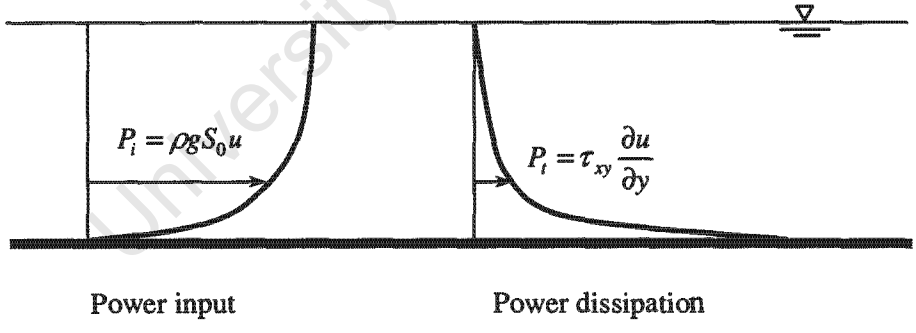

Figure 2.13: Unit stream power input and dissipation (Rooseboom & Mülke, 1982)

For conservation of power the areas enclosed by the two graphs in Figure 2.13 for power input and dissipation must be equal.

Incipient sediment motion may be measured according to the power dissipation P_t in the unit stream power model. Close to the channel bed, $\tau_{xy} \approx \tau_0 = \rho g h S_0$ (Equation 2.12) for uniform flow and $\tau_0 = \rho u_*^2$ (Equation 2.21). If the boundary is hydraulically smooth, the velocity gradient and hence stream power dissipation $P_{t(l)}$ are computed as follows:

$$\frac{\partial u}{\partial y} = \frac{u_*^2}{\nu} \tag{2.44}$$

$$P_{t(l)} = \tau_{xy} \frac{\partial u}{\partial y} = \frac{\rho u_*^4}{\nu} \approx \frac{(\rho g h S_0)^2}{\mu} \tag{2.45}$$

If the boundary is hydraulically rough, the velocity gradient and stream power dissipation $P_{t(t)}$ are given by:

$$\frac{\partial u}{\partial y} = \frac{u_*}{\kappa y} \tag{2.46}$$

$$P_{t(t)} = \tau_{xy} \frac{\partial u}{\partial y} = \frac{\rho u_*^3}{\kappa y} \approx \frac{\rho (g h S_0)^{3/2}}{\kappa y} \tag{2.47}$$

The power required to suspend a sediment particle, P_r, is given by the following:

$$P_r = (\rho_s - \rho) g v_{ss} \tag{2.48}$$

For sediment particle suspension, the applied stream power must instantaneously exceed that required for particle suspension, which implies

$$P_t \geq P_r \tag{2.49}$$

It is, however, not necessary for a particle to be suspended for incipient motion to take place. Rolling and sliding occur at lower threshold values of P_t. Thus for bedload transport, the average applied power need only be some fraction η of the power required for suspension P_r (Armitage, 2002):

$$P_t = \eta P_r \tag{2.50}$$

where $\eta < 1$. From the Rooseboom (1992) criteria for incipient motion according to the Movability Number (Equations 2.37 and 2.38), Armitage (2002) determined the following values for η for hydraulically smooth (η_l) and rough (η_t) conditions:

$$\eta_l = \frac{1}{9} \qquad \text{for smooth boundaries} \tag{2.51}$$

$$\eta_t = \frac{1}{190} \qquad \text{for rough boundaries} \tag{2.52}$$

If the boundary is hydraulically smooth, the velocity fluctuations to which sediment particles are subjected are damped and the average applied power required for incipience is greater than that required under rough conditions where velocity fluctuations are much greater.

As discussed in Section 2.3, sediment motion is stochastic in nature and it is convenient to describe incipience in terms of an intensity of motion. Following the Movability Number criteria for incipience given by Armitage (2002) in Equations 2.39 and 2.40, Armitage determined that the stream power fractions yielding an equivalent intensity of motion of $I = 2 \times 10^{-5}\ s^{-1}$ are

$$\eta_l = \frac{1}{6} \qquad \text{for smooth boundaries} \tag{2.53}$$

$$\eta_t = \frac{1}{67} \qquad \text{for rough boundaries}$$

(2.54)

Thus for incipience in turbulent boundaries in terms of the unit stream power model, Armitage (2002) proposed the following criterion:

$$P_t \geq \frac{P_r}{67}$$

(2.55)

For implementation of the unit stream power approach in a numerical model, a general three-dimensional form of the power dissipation function P_t is more useful than the one- and two-dimensional models presented thus far. The three-dimensional power dissipation function and its link to the energy equation (First Law of Thermodynamics) are presented in Section 3.2.3.

2.7 Incipient motion on sloping channel beds

The criteria for incipient motion discussed in the preceding sections have been developed for sediment particles lying on a horizontal bed. For small channel bed slopes the weight component of the particles in the direction of flow is often neglected. On steeper slopes and inclined river banks, however, neglecting the effects of bed slope on incipience may introduce appreciable errors (Chien & Wan, 1999).

For a particle on a longitudinal bed slope of β, the ratio of the critical drag force on the inclined bed $F_{D,c,\beta}$ to the critical drag force on a horizontal bed $F_{D,c,0}$ is given by (Chiew & Parker, 1994):

$$\frac{F_{D,c,\beta}}{F_{D,c,0}} = k_\beta = \cos\beta\left(1 - \frac{\tan\beta}{\tan\phi}\right)$$

(2.56)

A streamwise slope is indicated by a positive value of β while β is negative for adverse longitudinal bed slopes. Similarly, for a particle situated on a transverse slope (normal to the flow direction) inclined at an angle, γ, the following applies:

$$\frac{F_{D,c,\gamma}}{F_{D,c,0}} = k_\gamma = \cos\gamma\sqrt{1-\frac{\tan^2\gamma}{\tan^2\phi}} \tag{2.57}$$

The slope correction factors for longitudinal and transverse bed slopes, k_β and k_γ respectively, may be combined into a single slope correction factor ψ as follows:

$$\psi = \sqrt{k_\beta k_\gamma} = \sqrt{\cos\beta\left(1-\frac{\tan\beta}{\tan\phi}\right)\cos\gamma\left(1-\frac{\tan^2\gamma}{\tan^2\phi}\right)}^{1/2} \tag{2.58}$$

The critical Movability Number on a bed inclined at an angle β to the horizontal in the longitudinal direction and γ in the transverse direction is thus:

$$Mn_{c,\beta\gamma} = \psi Mn_{c,0} \tag{2.59}$$

where $Mn_{c,\beta\gamma}$ is the critical value of Mn on the sloping bed and $Mn_{c,0}$ is the critical Movability Number for a horizontal channel bed as discussed in Section 2.5.

To compute the critical stream power for incipience on an inclined channel bed, the following relationships apply:

$$P_{t,c,\beta\gamma} = \psi^2 P_{t,c,0} \qquad \text{for smooth boundaries} \tag{2.60}$$

$$P_{t,c,\beta\gamma} = \psi^3 P_{t,c,0} \qquad \text{for rough boundaries} \tag{2.61}$$

Since $P_{t(l)} \propto u_*^2$ for hydraulically smooth boundaries (Equation 2.45) and $P_{t(l)} \propto u_*^3$ for rough turbulent boundaries (Equation 2.47), the respective correction factors ψ^2 and ψ^3 must be applied to the critical stream power required to mobilise a particle on a flat channel bed $P_{t,c,0}$ to obtain the critical value for a particle on a slope $P_{t,c,\beta\gamma}$.

A limitation of the slope correction function (Equation 2.58) is that ψ becomes undefined when the bed slope angle exceeds the sediment angle of repose. Implicit in this formulation, therefore, is that a particle on a slope angle equal to or exceeding ϕ is unstable and will be mobilised under any infinitesimal force. Dey *et al.* (1995), however, studied flow fields in clear-water scour holes at circular piers and found that the average upstream slope of the equilibrium scour hole exceeded the sediment angle of repose by 10 to 20%. This so-called "dynamic angle of repose" is sustained by turbulent fluctuations in the flow and is not accounted for in the formulation presented above.

Lysne (1969) studied the initial motion of sand on sloping beds and commented that the angle ϕ in the slope correction formula (Equation 2.58) should not be set equal to the geotechnical angle of repose. Instead, Lysne suggested that ϕ should be chosen to represent the frictional or rolling resistance of particles. He proposed values of ϕ between 37° and 52° which provided a better fit with his experimental data for incipience.

2.8 Mechanisms of sediment particle motion

Separation of a stream's sediment load into different components is artificial. It is, however, convenient to classify the load components according to the mechanisms of particle motion as it is from these mechanisms that models of incipient motion are developed. Vanoni (1977) separates the different types of sediment load into *contact*, *saltation* and *suspended load.* The contact and saltation loads together constitute the *bedload.*

At low flow velocities, the destabilising forces acting on a particle may overcome the stabilising forces causing the particle to roll or slide along the channel bed as *contact load* which is frequently in contact with the bed. If flow velocities are slightly greater, particles

are subjected to larger lift and drag forces which may displace them small distances above the bed for short time periods. These particles move in small "jumps" as *saltation load.* At higher flow velocities, saltating particles are carried further from the bed into the main body of the flow and may be transported in suspension for considerable distances and lengths of time. Turbulent eddies maintain the motion of these particles which constitute the *suspended load* (Chien & Wan, 1999).

As this study is concerned with clear-water scour (Section 2.9.5), the flow conditions under which sediment motion commences and when bedload predominates are of interest. Under these conditions, suspended load constitutes an extremely small fraction of the stream load. The effects of the suspended particles on properties of the fluid are therefore neglected.

2.9 Types of scour

The separation of scour into different types is also artificial as these types of scouring take place simultaneously in the fluvial environment and the effects of different scouring mechanisms are superimposed upon each other. It is nevertheless convenient to classify scour according to the mechanism causing each type to facilitate the study of processes associated with local scour in particular.

Five types of scouring are discussed here, namely: *overall degradation*, *constriction scour*, *bend scour*, *confluence scour* and *local scour*. The classification and grouping of different types of scouring varies in literature. Hoffmans & Verheij (1997) identify only two categories: *general* and *local* scour, where the category *general scour* encompasses the first four scour types listed above. Raudkivi (1998), however, considers three forms of scouring: *general*, *constriction* and *local* scour. A brief description of each of the five types of scouring considered in this study is given below.

2.9.1 Overall degradation

Overall degradation, and indeed the opposite process of aggradation, occurs when there is an imbalance between the sediment load and sediment carrying capacity of a stream. This type of scouring is a response to the flow regime and occurs irrespective of whether there is a structure present or not. It may, however, take place as a result of man-made interventions in the fluvial environment (Breusers & Raudkivi, 1991; Raudkivi, 1998).

2.9.2 Constriction scour

Constriction scour occurs where the width of a stream is restricted by, for example, the encroachment of road embankments at a bridge on the floodplain or river channel. The reduced cross-sectional area of the stream increases the flow velocity and thus the potential for scour.

The magnitude of constriction scour in "long" constrictions, where the length of the contraction exceeds the approach channel width (Komura, 1966; Lim & Cheng, 1998), is conventionally computed from continuity equations for the movement of sediment and water. Details may be found in Raudkivi (1998).

2.9.3 Bend scour

Both the water surface elevation and channel bed bathymetry vary laterally across bends. The water surface rises towards the outside of the bend due to centrifugal forces. Secondary currents generate helical flow patterns and the bed tends to scour more deeply near the outside of the bend as a result of this spiralling flow (Breusers & Raudkivi, 1991). Bend scour is a function of local variables such as the bend curvature, flow depth and sediment grain size distribution (Hoffmans & Verheij, 1997).

2.9.4 Confluence scour

Two intercepting streams invariably have different flow rates, slopes and sediment loads. The patterns of scour and deposition around a confluence depend on the flow and sediment characteristics of the two streams and the angle of confluence.

2.9.5 Local scour

Local scour occurs where the flow is obstructed by the presence of, for example, a bridge pier, abutment or river training works. The structure modifies local flow patterns, producing complex three-dimensional vortical flow structures and corresponding patterns of scour and deposition. The time scale of local scour is short relative to that of general scour (Hoffmans & Verheij, 1997).

Local scour may be further classified as *clear-water* or *live-bed* scour depending on whether or not the oncoming flow carries sediment. *Clear-water* local scour occurs when the flow approaching a structure is free of sediment, that is, in the absence of general scour. The conditions upstream of the obstacle are thus below the critical conditions required to mobilise sediment. Sediment removed from the scour hole is not replaced by material carried by the approaching flow (Graf, 1998). When *live-bed* scour occurs, critical conditions for sediment transport have been reached upstream of the obstacle so that the approach flow carries sediment. Live-bed local scour thus takes place simultaneously with general scour.

Figure 2.14 illustrates the variation of local scour depth y_s with time t for clear-water and live-bed scour. A clear-water scour hole develops less rapidly than a live-bed scour hole and the maximum clear-water scour depth is approached asymptotically. A live-bed scour hole does not reach a fixed equilibrium depth as the scour depth fluctuates continuously with the passage of bedforms such as ripples and dunes. The equilibrium clear-water scour depth exceeds the time-averaged "equilibrium" live-bed scour depth (Breusers & Raudkivi, 1991).

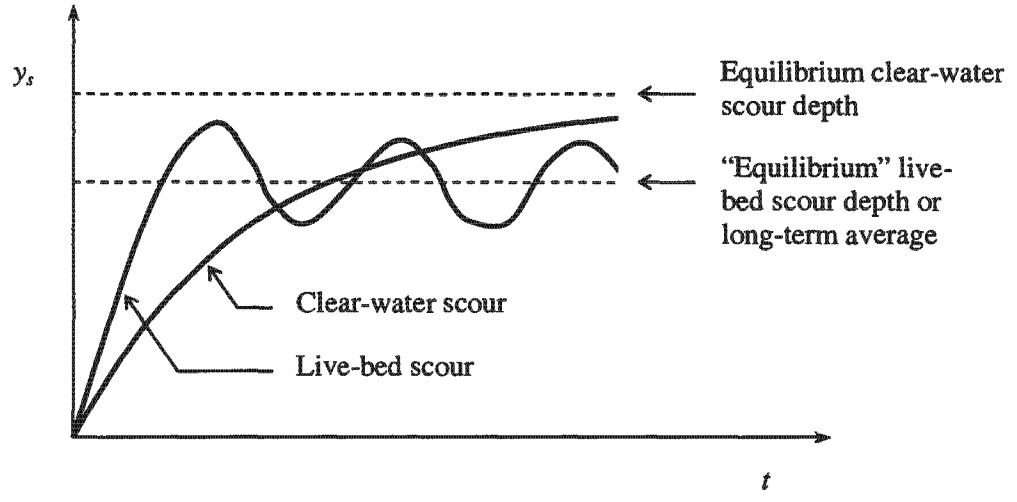

Figure 2.14: Temporal development of clear-water and live-bed local scour (Graf, 1998; Raudkivi, 1998)

This study is concerned with the modelling of clear-water local scour. Not only is the analysis of clear-water scour simpler than that of live-bed scour, but the greater equilibrium scour depths attained under clear-water conditions are important for engineering design.

2.10 Local scour at piers and abutments

The flow patterns around an obstacle such as a pier or abutment are complex and strongly three-dimensional (Graf, 1998). The complexity of these flow patterns increases with the development of a local scour hole (Dey *et al.*, 1995; Raudkivi, 1998).

The flow features at a circular pier and rectangular abutment and the associated clear-water scour and deposition patterns are discussed in the following sections. The reliability of empirical formulae which are commonly used for local scour depth calculation is also discussed.

2.10.1 Flow features and scour hole development at a circular pier

a) Flow features at a circular pier

The flow at a cylindrical pier is characterised by a *downflow* and *bow wave* at the upstream face of the pier, a *horseshoe vortex* around the pier base and *wake vortices* behind the obstacle (Figure 2.15).

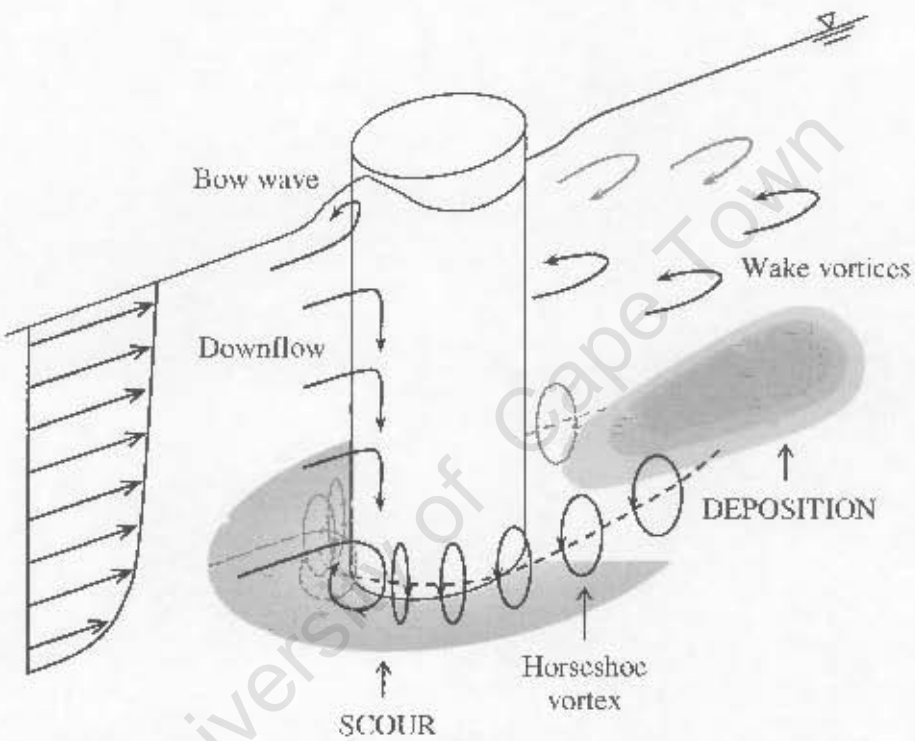

Figure 2.15: Flow features and scour patterns at a circular pier
(Graf, 1998; Hoffmans & Verheij, 1997; Raudkivi, 1998)

For the purpose of the discussion that follows, it is assumed that uniform flow with a logarithmic velocity profile approaches the pier. The velocity reduces to zero at the upstream pier face in the plane of symmetry giving rise to a stagnation pressure of magnitude ρu^2, which decreases from the free surface to the channel bed. This pressure gradient gives rise to a downflow in front of the pier. The maximum vertical velocity, v_{max}, occurs $0.02d_p$ to $0.05d_p$ upstream of the pier face where d_p is the pier diameter (Ettema,

1980; Raudkivi, 1986). If there is no scour hole present, $v_{max} \approx 0.4U$. When $y_s > 2d_p$ at the pier face, a maximum downflow of $v_{max} \approx 0.8U$ occurs approximately one pier diameter below the bed of the approach flow (Raudkivi, 1998).

A horseshoe vortex forms as a result of flow separation at the upstream edge of the scour hole. The axis of the horseshoe vortex is horizontal and concentric with the pier around the upstream face (Dey *et al.*, 1995; Hoffmans & Verheij, 1997). This vortex extends a few pier diameters downstream of the pier before becoming part of the general wake turbulence further downstream (Breusers & Raudkivi, 1991). Breusers & Raudkivi (1991) indicate that the horseshoe vortex is a consequence rather than a cause of scouring although its helical flow patterns aid in the transportation of sediment out of the scour hole. Graf & Isitiarto (2002), however, state that the horseshoe vortex is active in the local scour process.

A bow wave, rotating in the opposite sense to the horseshoe vortex, develops near the free surface at the upstream face of the pier and helps to drive the downflow in front of the pier. There is a rise in the free surface associated with stagnation of the flow at this point. The importance of the bow wave depends on the flow depth and pier geometry. If the flow depth is small relative to the pier diameter, the bow wave interacts with the horseshoe vortex and reduces the strength of the downflow (Raudkivi, 1998).

Flow separation occurs in the horizontal plane downstream of the pier to generate wake vortices with vertical axes of rotation. These wake vortices may be shed alternately from the pier sides to form a Von Karman vortex street. The wake vortices interact with the horseshoe vortex to lift sediment off the bed. Accelerated flow around the cylinder sides also assists wake scouring (Dargahi, 1990).

b) Scour hole development at a circular pier

In an experimental study, Dargahi (1990) found that scour is initiated at two small lateral scour holes at approximately 45° to the pier centreline as the flow accelerates around the pier sides. These holes migrate rapidly upstream and around the upstream face of the pier

(Graf, 1998). The horseshoe vortex then develops and a shallow scour hole concentric with the cylinder then extends around approximately 120° of the perimeter of the cylinder on the upstream side (Breusers & Raudkivi, 1991).

There is conflict in the literature as to the location at which scour commences. Some investigators suggest that scour is initiated at the upstream face of the pier on the symmetry plane by downflow impinging on the bed (Graf, 1998; Graf & Istiarto, 2002) while others describe the formation and upstream migration of two lateral scour holes due to flow acceleration around the pier sides (Breusers & Raudkivi, 1991; Raudkivi, 1998). Dargahi (1990) proposes that both mechanisms simultaneously promote initial scouring but the latter mechanism dominates as the maximum shear stress in fixed bed experiments is found at approximately 45° to the symmetry plane.

The downflow excavates a groove at the upstream face in which the flow is turned 180°. The horseshoe vortex forces the maximum vertical downflow velocity closer to the pier so that the flow acts as a vertical jet impinging on the sediment bed (Breusers & Raudkivi, 1991). The scoured sediment is transported by the horseshoe vortex and wake vortices and is deposited to form a bar in the wake of the pier.

Hoffmans & Verheij (1997) categorise the temporal development of local scour holes into four phases; an initial phase, a development phase, a stabilisation phase and an equilibrium phase. They suggest that local scour around bridge piers is a relatively rapid process. Raudkivi (1998), however, notes that the development of the maximum clear-water scour depth can take several days. This is a very long period of time in the context of numerical modelling if the temporal development of the equilibrium scour hole is to be simulated in real time. Live-bed scour reaches equilibrium more rapidly (Raudkivi, 1998).

Dargahi (1990) found that the time evolution of the rate of scouring and deposition were well described by a logarithmic relationship.

The upstream portion of the equilibrium scour hole is similar in shape to an inverted cone and has side slopes on the upstream side equal to the angle of repose of the sediment (Graf, 1998; Raudkivi, 1998). The maximum scour depth is found at the upstream face of the

pier (Graf & Istiarto, 2002). The peak clear-water scour depth is of the order of $2.3d_p$ to $2.4d_p$ if the flow is deep and the sediment grain size is small relative to the pier diameter (Raudkivi, 1998).

Dargahi (1990) indicates that experimental investigations have shown that the maximum scour depth is strongly dependent on the pier diameter and shape and that other variables such as the flow velocity, depth and sediment size are of less importance. The size of the pier influences the strength of the horseshoe vortex at the pier base and this horseshoe vortex is most influential in the scouring process (Hoffmans & Verheij, 1997).

2.10.2 Flow features and scour hole development at an abutment

Abutments create both a horizontal constriction of the flow and the three-dimensional flow patterns associated with local scouring. Raudkivi (1998) estimates that about one third of bridge failures in floods are due to abutment scour.

The importance of different flow features at an abutment and their role in scouring depends strongly on the abutment geometry. Dimensionless ratios between parameters such as the flow depth, abutment dimensions and sediment particle sizes are frequently used to describe the relative importance of flow features and their interaction with one another (Hoffmans & Verheij, 1997).

Abutments may be classified as submerged or non-submerged, streamlined or sharp-nosed and long or short depending on their protrusion into the flow. Common types are wing-wall and spill-through abutments (Raudkivi, 1998). Sharp-nosed vertical wall abutments, such as the rectangular plate modelled in this study, are almost never employed in the field (Hoffmans & Verheij, 1997) but provide a convenient reference for more common designs. A generic description of the flow patterns and scouring at a non-submerged abutment follows.

a) Flow features at an abutment

A number of investigators have drawn comparisons between the flow and scour patterns at piers and abutments (Melville, 1997). This comparison is particularly valid for "short" abutments which protrude, in the transverse direction, a relatively small distance into the flow. Dey & Barbhuiya (2004) define a "short" abutment as one at which the ratio of the abutment length L_a, measured perpendicular to the mean flow direction, to the approach flow depth h, does not exceed unity. In this instance, the flow patterns at a short abutment are like those at half a pier.

The flow features evident at a typical abutment are illustrated in Figure 2.16.

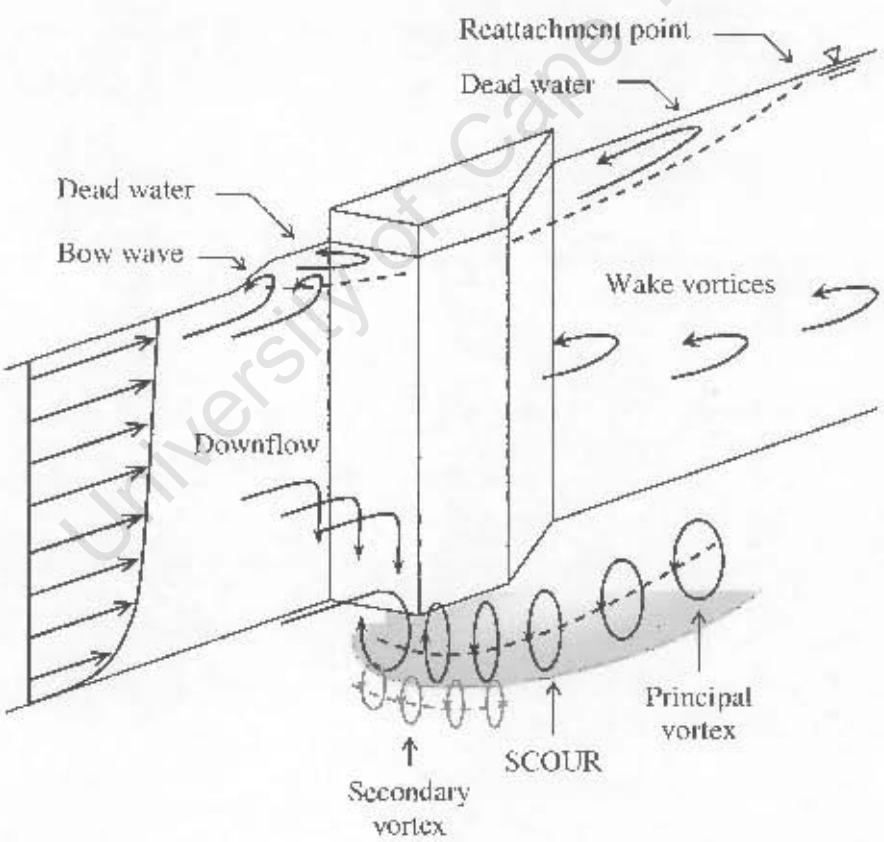

Figure 2.16: Flow features and scour patterns at an abutment
(Graf, 1998; Hoffmans & Verheij, 1997; Melville, 1997; Raudkivi, 1998)

Depending on the abutment geometry, a dead water region and eddy may develop upstream of the abutment, adjacent to the channel wall. A surface roller develops at the boundary of this dead water region where downflow takes place. As at piers, in shallow flow the surface roller or bow wave reduces the strength of the downflow and principal vortex as these two vortices rotate in the opposite sense.

The downflow generates a principal vortex which is analogous to the horseshoe vortex at a circular pier (Section 2.10.1). As in the horseshoe vortex, strong spiralling flow in the principal vortex, aided by the downflow, causes scouring around the abutment and transports sediment downstream. The principal vortex induces development of a weaker secondary vortex (shown in Figure 2.16) which rotates in the opposite sense and may also cause some scouring if sufficiently strong.

Downstream of the abutment, the main flow region is separated from the eddies in the downstream dead water region by a trail of wake vortices. Uniform flow is established some distance downstream of the reattachment point.

b) Scour hole development at an abutment

Scour at short abutments may be likened to that at bridge piers (Raudkivi, 1998). Kwan (1984) compared scour depths at a circular pier and semi-circular abutment of the same diameter. As expected, the maximum equilibrium scour depth at the abutment was less than that at the pier due to formation of a boundary layer on the wall adjacent to the abutment. Flow retardation at the wall reduces downflow upstream of the abutment but these wall effects becomes less significant for "long" abutments where $L_a / h > 25$ (Melville, 1992).

The principal vortex, driven by downflow near the upstream abutment face, is active in the scouring process (Graf, 1998).

The maximum scour depth is often found at the protruding tip of the abutment. Breusers & Raudkivi (1991) note that experimental investigations indicate that the slope of the

abutment and ratio of the abutment length to flow depth, L_a / h, are important in scour depth estimation.

Due to the constriction effects caused by abutments, even if clear-water conditions prevail upstream, live-bed scour may still take place in the constriction and for some distance downstream. Raudkivi (1998) notes that local scour at the abutment will not fully compensate for the effects of the constriction.

2.10.3 Limitations of empirical formulae for prediction of scour depth

Many investigators have developed empirical formulae for local scour depths from experimental measurements and dimensional analysis. Hoffmans & Verheij (1997) and Graf (1998) present summaries of selected formulae and Raudkivi (1998) discusses the effects of specific variables on computed scour depths. Empirical formulae are, however, notoriously inconsistent in the scour depths they predict and have a limited range of application.

Johnson (1995) gives a summary of seven commonly used empirical formulae for scour depth estimation at bridge piers. Johnson compared scour depths predicted by these formulae to field measurements and found that the calculated and observed depths differed by up to a factor of 10. All seven formulae over or under-predicted scour depths by a factor of 5 under certain conditions. Such large uncertainties are unacceptable for the purpose of engineering design.

Consistent and accurate methods for local scour prediction need to be developed. Three-dimensional numerical modelling using Computational Fluid Dynamics (CFD) has become increasingly attractive with advances in computer hardware.

CFD has the advantage that, once a working model has been developed, sensitivity studies may be conducted with relatively little additional effort. Very large systems can be analysed where controlled experiments would be difficult (e.g. large river systems) and output may be generated to an almost unlimited level of detail. This eliminates scale

effects in experimental models. Hazardous conditions where field measurements are difficult, such as during large floods, can also be safely simulated in a numerical model (Versteeg & Malalasekera, 1995).

2.11 Conclusions

An overview of sediment transport theory relevant to clear-water local scouring was presented in this chapter. The concept of incipience and the Movability Number and unit stream power models for incipient sediment motion were introduced. Flow features and typical local scour patterns at piers and abutments were also reviewed.

Empirical formulae for local scour depth estimation are inconsistent and unreliable. Numerical modelling using CFD is an alternative which may yield more reliable and accurate scour depth predictions.

Chapter 3
Numerical Modelling of Local Scour using CFD

Computational Fluid Dynamics (CFD) is a tool for the analysis of systems involving fluid flow, heat transfer and related phenomena by means of computer simulation (Versteeg & Malalasekera, 1995).

In this chapter the structure of commercial CFD codes and the governing equations of fluid flow underlying the numerical algorithms are discussed. The Navier-Stokes equations are presented and the three-dimensional unit stream power function is linked to the energy equation. Turbulent closure schemes for the analysis of turbulent open channel flow are considered. Past work in numerical modelling of local scour is also reviewed.

The focus of this chapter is the theory underlying CFD codes in general. Practical application of CFD to the problem of local scouring in open channels using Fluent 6.2 and parameters relating specifically to the Fluent code are addressed in Chapter 4.

3.1 Structure of CFD codes

A CFD code consists of three components: a pre-processor, solver and post-processor. In the pre-processor, the user defines the problem inputs. The flow field is then computed by the solver and the results may be analysed in the post-processor.

3.1.1 Pre-processor

In the pre-processing phase, the user defines the problem though a user-friendly interface and this input is translated into a form which may be used by the solver. The geometry or computational domain is defined and sub-divided into a mesh of non-overlapping control volumes or cells in which the computation will take place.

The fluid flow phenomena to be modelled, such as free surface flow, particle-laden flow, chemical reactions or combustion, are specified. Fluid properties are selected and appropriate initial and boundary conditions imposed.

3.1.2 Solver

The solver computes the flow solution using numerical techniques to solve the equations governing fluid flow (Section 3.2). Solvers may be grouped into three different streams; finite difference methods, finite element methods and finite volume techniques.

Finite difference techniques employ truncated Taylor series to approximate governing differential equations. The derivative of an unknown variable is expressed in terms of the values of this variable at neighbouring points. The differential equations are thus converted to algebraic equations for the values of the unknown variable at each point and solved.

In *finite element* methods, which are more complex than finite difference techniques, variations of the unknown flow variables are represented by simple piecewise-defined functions. These functions will not satisfy the governing equations precisely so that there are some errors in the solution. These errors or residuals are minimised by multiplication with weighting functions and integration. A system of algebraic equations for the coefficients of the assumed piecewise functions is thus obtained and solved.

The *finite volume* method is the most well-established and comprehensively validated general purpose CFD technique (Versteeg & Malalasekera, 1995) and forms the basis of the code Fluent 6.2 applied in this study. The finite volume method is intermediate in complexity between finite difference and finite element techniques. The governing equations are integrated over the control volumes into which the domain was subdivided. Finite difference approximations are substituted for terms in the integral equations which are then converted into algebraic equations and solved iteratively. Versteeg & Malalasekera (1995) comment that the finite volume method is an attractive approach as its

formulation demonstrates a clear link between the numerical algorithm and underlying conservation principles.

3.1.3 Post-processor

The post-processor facilitates visualisation and analysis of the solution data from a user friendly interface. The user may generate alphanumeric reports, graphs, shaded contour and vector plots and animations.

3.2 Governing equations of fluid flow

3.2.1 Control volume and Cartesian co-ordinate system

The conservation principles presented in the following sections refer to a control volume with dimensions dx, dy and dz in the mutually-perpendicular Cartesian co-ordinate directions x, y and z respectively (Figure 3.1). The velocity vector **u**, which is defined at the control volume centre, has components u, v and w in the respective x, y and z directions.

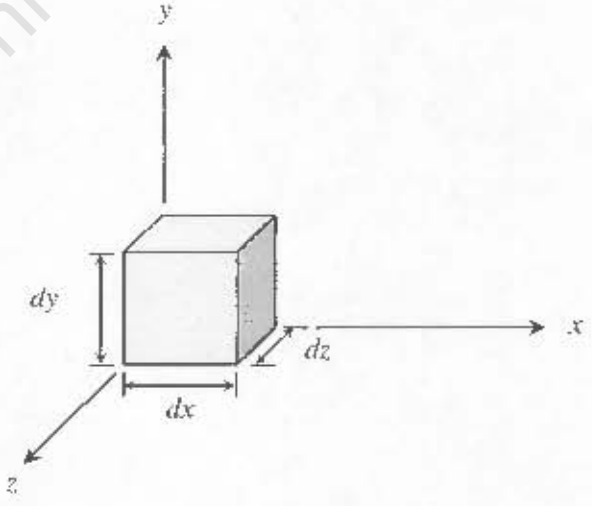

Figure 3.1: Control volume in the Cartesian co-ordinate system

3.2.2 Navier-Stokes equations

The Navier-Stokes equations are the equations for the conservation of mass (continuity equation) and momentum (Newton' Second Law). Details of the derivations of these equations are not given here but may be found in Patankar (1980), Versteeg & Malalasekera (1995) or White (1991).

The unsteady, three-dimensional mass conservation equation at a point in a compressible fluid is given by Versteeg & Malalasekera (1995) as:

$$\frac{\partial \rho}{\partial t} + div(\rho \mathbf{u}) = 0 \tag{3.1}$$

For an incompressible fluid with constant density, the continuity equation becomes

$$div\mathbf{u} = 0 \quad \Rightarrow \quad \frac{\partial u}{\partial x} + \frac{\partial v}{\partial y} + \frac{\partial w}{\partial z} = 0 \tag{3.2}$$

Newton's Second Law, or the momentum equation, states that the rate of change of momentum of a fluid particle is equal to the resultant force acting upon it. Versteeg & Malalasekera (1995) express the momentum equations for the x, y and z co-ordinate directions in the following way:

$$\rho \frac{Du}{Dt} = -\frac{\partial p}{\partial x} + div(\mu grad u) + S_{Mx} \tag{3.3}$$

$$\rho \frac{Dv}{Dt} = -\frac{\partial p}{\partial y} + div(\mu grad v) + S_{My} \tag{3.4}$$

$$\rho \frac{Dw}{Dt} = -\frac{\partial p}{\partial z} + div(\mu grad w) + S_{Mz} \tag{3.5}$$

where p is the pressure or normal stress applied to the control volume and S_M is a source term which would be used to incorporate body forces such as gravity which act on the entire mass of the fluid element. Surface forces acting on the faces of the control volume are treated separately in the derivation of the momentum equations to facilitate linking of the shear stresses to deformation rates and hence the flow velocity by assumption that the fluid is Newtonian. In a Newtonian fluid, the viscous stresses are linearly proportional to the rates of deformation. Details may be found in White (1991).

Considering gravity as the only body force acting on the control volume, White (1991) expresses the momentum equation in the following vector form:

$$\rho\frac{D\mathbf{u}}{Dt} = \rho\mathbf{g} - \nabla p + \frac{\partial}{\partial x_j}\left[\mu\left(\frac{\partial u_i}{\partial x_j} + \frac{\partial u_j}{\partial x_i}\right) + \delta_{ij}\lambda div\mathbf{u}\right] \tag{3.6}$$

where λ is the coefficient of bulk viscosity or Lamé's constant.

Substituting $div\mathbf{u} = 0$ (Equation 3.2) for incompressible flow and assuming a constant viscosity μ, Equation 3.6 may be restated as follows:

$$\rho\frac{D\mathbf{u}}{Dt} = \rho\mathbf{g} - \nabla p + \mu\nabla^2\mathbf{u} \tag{3.7}$$

3.2.3 Energy equation and power dissipation function in three dimensions

The first law of thermodynamics states that the rate of change of energy of a fluid particle is equal to the rate of heat addition plus the rate of work done on the particle. Versteeg & Malalasekera (1995) use the Newtonian model for viscous stresses to state the energy equation as follows:

$$\rho\frac{Di}{Dt} = -pdiv\mathbf{u} + div(kgradT) + \Phi + S_i \tag{3.8}$$

where i is the internal energy, k is the conduction coefficient, T is the fluid temperature, Φ is the dissipation function and S_i accounts for any external energy sources.

Open channel flow is isothermal and temperature variations and heat transfer are therefore not of interest in this study. The dissipation function, which accounts for the work done by viscous stresses in the energy equation, is, however, in fact an expression of the applied unit stream power in three dimensions (Armitage, 2002). Φ is defined as (White, 1991):

$$\Phi = \tau_{ij}\frac{\partial u_i}{\partial x_j} \tag{3.9}$$

Versteeg & Malalasekera (1995) indicate that Φ represents a source of internal energy due to the deformation work on the fluid particle. This work is extracted from the mechanical agent causing motion which in this instance is gravitational potential energy. This coincides with the one-dimensional unit stream power theory of Rooseboom (1992) (Section 2.6) where the power made available through the release of potential energy P_i and power dissipated through shearing in the flow P_t were given by:

$$P_i = \rho g S_0 u \tag{2.42}$$

$$P_t = \tau_{xy}\frac{\partial u}{\partial y} \tag{2.43}$$

The viscous stresses, denoted by τ_{ij} in Equation 3.9 and illustrated in Figure 3.2, may be expressed in terms of the fluid velocity components, by the assumption of some deformation law as assumed for derivation of the momentum and energy equations.

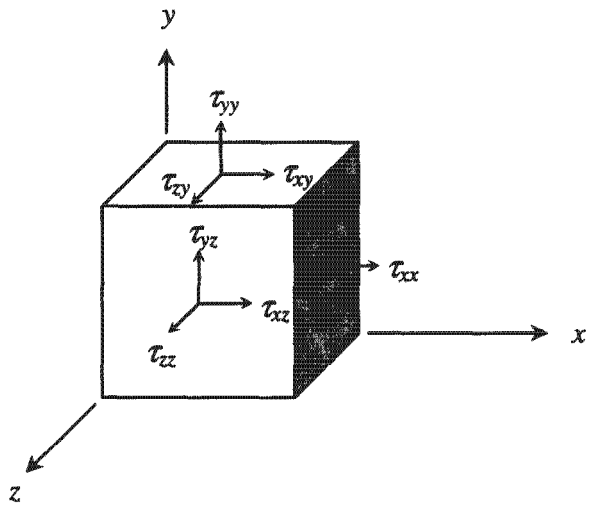

Figure 3.2: Viscous stresses acting on the faces of the control volume

For an incompressible, Newtonian fluid, the nine viscous stresses represented by the symmetric stress tensor τ_{ij} are given by (Schlichting, 1979):

$$\tau_{xx} = 2\mu\frac{\partial u}{\partial x}$$

$$\tau_{yy} = 2\mu\frac{\partial v}{\partial y}$$

$$\tau_{zz} = 2\mu\frac{\partial w}{\partial z}$$

$$\tau_{xy} = \tau_{yx} = \mu\left(\frac{\partial u}{\partial y} + \frac{\partial v}{\partial x}\right)$$

$$\tau_{xz} = \tau_{zx} = \mu\left(\frac{\partial u}{\partial z} + \frac{\partial w}{\partial x}\right)$$

$$\tau_{yz} = \tau_{zy} = \mu\left(\frac{\partial v}{\partial z} + \frac{\partial w}{\partial y}\right) \qquad (3.10)$$

Substitution of τ_{ij} (Equations 3.10) for an incompressible Newtonian fluid into Φ (Equation 3.9) yields the power dissipation function in terms of flow velocity which is a three-dimensional expression of the applied stream power P_t. The three-dimensional form of the applied unit stream power is thus (Armitage, 2002; White, 1991; Yang & Song, 1979; Versteeg & Malalasekera, 1995):

$$P_t \equiv \Phi = \mu\left[2\left(\left(\frac{\partial u}{\partial x}\right)^2+\left(\frac{\partial v}{\partial y}\right)^2+\left(\frac{\partial w}{\partial z}\right)^2\right)+\left(\frac{\partial u}{\partial y}+\frac{\partial v}{\partial x}\right)^2+\left(\frac{\partial u}{\partial z}+\frac{\partial w}{\partial x}\right)^2+\left(\frac{\partial v}{\partial z}+\frac{\partial w}{\partial y}\right)^2\right] \tag{3.11}$$

3.2.4 Transport of scalar quantities

The conservation equations for mass, momentum and energy can be stated in a common form which is also applicable to the conservation of scalar quantities such as pollution concentration and secondary phases in a continuous fluid. Versteeg & Malalasekera (1995) state the conservation equation for a general scalar quantity φ as follows:

$$\frac{\partial(\rho\varphi)}{\partial t} + div(\rho\varphi\mathbf{u}) = div(\Gamma grad\varphi) + S_\varphi$$

Time rate of change of φ	+	Convection of φ due to flow out of element	=	Rate of increase of φ due to diffusion	+	Rate of increase of φ due to sources

(3.12)

where Γ is a diffusion coefficient and S_φ represents sources of the scalar quantity φ.

The Volume of Fluid (VOF) method (Hirt & Nichols, 1981) for the free surface tracking employed in this study to model open channel flow, computes the volume fraction of water in cells using a scalar transport equation similar to Equation 3.12.

3.3 Turbulence modelling

3.3.1 Need for turbulence modelling

The fluid motion in turbulent flows is highly random, unsteady and three-dimensional in nature. Turbulent flow is characterised by eddying motion at a wide range of length and time scales (Rodi, 1984). Versteeg & Malalasekera (1995) suggest that a domain measuring 0.1 m x 0.1 m may contain eddies as small as 10 μm in size and the fastest events would take place with a frequency in the order of 10 kHz. A computational mesh with 10^9 to 10^{12} grid points and time steps of 100μs would thus be required to capture events at all length and time scales.

Although the exact equations describing turbulent flow, the Navier-Stokes equations (Section 3.2.2), are known and form a closed system, their solution by direct numerical simulation (DNS) for engineering problems of practical relevance demands computing power far in excess of what is currently available.

Reynolds therefore adopted a statistical approach, averaging the Navier-Stokes equations over a finite time step which is long compared to the time scales associated with turbulent fluctuations. The Reynolds Stress Model was introduced in Section 2.4.1. The instantaneous velocities u_i and value of any arbitrary scalar variable φ, were represented as the sum of a temporal mean and turbulent fluctuating component.

$$u_i = \overline{u}_i + u_i' \tag{3.13}$$

$$\varphi = \overline{\varphi} + \varphi' \tag{3.14}$$

Substitution of Equations 3.13 and 3.14 into the Navier-Stokes equations yields the Reynolds-Averaged Navier-Stokes (RANS) equations. Versteeg & Malalasekera (1995) write the time-averaged transport equation for an arbitrary scalar φ as follows:

$$\frac{\partial(\rho\overline{\varphi})}{\partial t} + div(\rho\overline{\varphi}\mathbf{u}) = div(\Gamma grad\overline{\varphi}) + \left[-\frac{\partial(\rho\overline{u'\varphi'})}{\partial x} - \frac{\partial(\rho\overline{v'\varphi'})}{\partial y} - \frac{\partial(\rho\overline{w'\varphi'})}{\partial z} \right] + S_{\varphi} \tag{3.15}$$

The complete set of three RANS equations for momentum conservation is not given here but is obtained by simply substituting u, v and w for φ in Equation 3.15.

The time averaging procedure introduced by Reynolds introduces six unknown Reynolds Stress terms (Section 2.4.1) into the Navier-Stokes equations. The RANS equations thus do not constitute a closed system.

A *turbulence model*, consisting of algebraic or differential equations and empirical coefficients, is therefore required to determine the turbulent transport terms containing the fluctuating velocity components to close the RANS set of equations. These fluctuating components are usually expressed as functions of the mean flow properties (Schlichting & Gersten, 2000). The details of turbulent motion are not simulated by a turbulence model but the effects of turbulence on the mean motion are accounted for (Rodi, 1984). Modelling of only the effects of turbulence on the mean flow is adequate for many engineering applications.

Intermediate in complexity and computational expense between DNS and approximation of turbulent fluctuating terms in the RANS equations are the large eddy simulation (LES) and very large eddy simulation (VLES) models. In LES and VLES, the exact Navier-Stokes equations are solved for the larger eddies in the flow which are also associated with longer time scales. Approximations are introduced to model smaller eddies and their associated shorter time scales and higher frequency events. The trade-off between computational expense and the degree of turbulence modelling or approximation is shown in Figure 3.3.

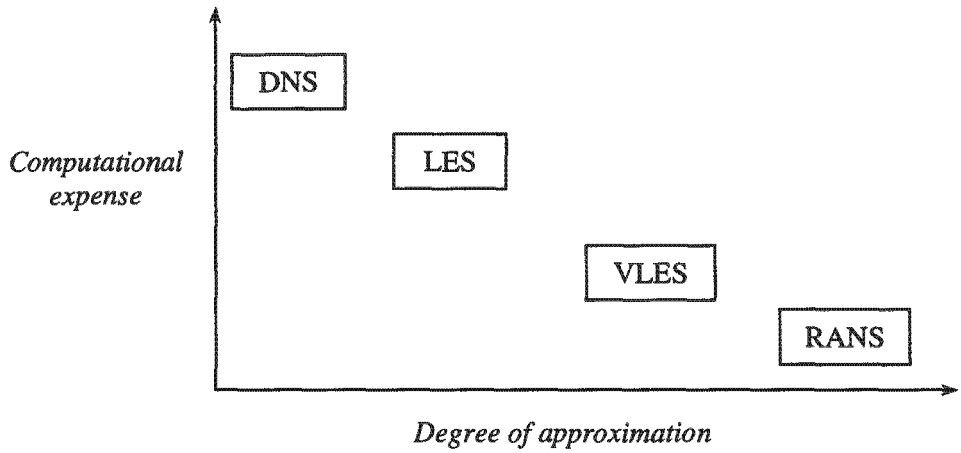

Figure 3.3: Trade-off between computational expense and degree of approximation in turbulence modelling (McGahey, 2001)

3.3.2 Common turbulence closure schemes

An overview of selected turbulence models commonly used for closure of the RANS equations in commercial CFD codes is given in this section. As a thorough investigation of turbulence modelling options for local scour prediction did not form part of this study, the discussion that follows is kept brief. Rodi (1984) provides a more detailed summary of turbulence models and their application to hydraulic problems.

Turbulence models are often called *one-equation models*, *two-equation models* and so on according to the number of partial differential equations solved in the model (Schlichting & Gersten, 2000). Models such as the mixing length model which solve algebraic equations for turbulent quantities are termed *zero-equation models*.

a) Zero-equation mixing length models

Mixing length models attempt to describe the turbulent stresses by means of simple algebraic formulae for the turbulent viscosity μ_t as a function of position. The Prandtl

(1925) mixing length model is an example that was introduced in Section 2.4.1. Most of the kinetic energy associated with turbulent flow is contained in the largest eddies. The velocity scales of these large eddies can thus be linked the mean flow properties.

Mixing length models are computationally economical and give good agreement between numerical models and experimental data for simple two-dimensional flows (Schlichting, 1979). They are widely used in the aerospace industry. They are, however, completely incapable of describing separating and recirculating flows (Versteeg & Malalasekera, 1995). Mixing length models would thus be inappropriate for the numerical modelling of local scour as flow separation occurs in the wake of piers and abutments, and the upstream flow separation in the horseshoe and principal vortices is key to the scouring process.

b) Two-equation models

The two-equation *k-ε model* (Launder & Spalding, 1972) computes the transport of turbulence properties by the mean flow and allows for the production and destruction of turbulence. Two partial differential equations (PDEs) are solved for the turbulent kinetic energy k and rate of dissipation ε.

As the k- ε model was applied in this study, the general transport equations for turbulent kinetic energy k and the dissipation rate ε are reproduced here:

$$\frac{\partial}{\partial t}(\rho k)+\frac{\partial}{\partial x_i}(\rho k u_i)=\frac{\partial}{\partial x_j}\left[\left(\mu+\frac{\mu_t}{\sigma_k}\right)\frac{\partial k}{\partial x_j}\right]+G_k+G_b-\rho\varepsilon-Y_M+S_k \tag{3.16}$$

$$\frac{\partial}{\partial t}(\rho \varepsilon)+\frac{\partial}{\partial x_i}(\rho \varepsilon u_i)=\frac{\partial}{\partial x_j}\left[\left(\mu+\frac{\mu_t}{\sigma_\varepsilon}\right)\frac{\partial \varepsilon}{\partial x_j}\right]+C_{1\varepsilon}\frac{\varepsilon}{k}(G_k+C_{3\varepsilon}G_b)-C_{2\varepsilon}\rho\frac{\varepsilon^2}{k}+S_\varepsilon \tag{3.17}$$

where σ_k and σ_ε are the respective turbulent Prandtl numbers for k and ε, G_k and G_b represent the generation of turbulent kinetic energy due to mean velocity gradients and buoyancy respectively and S_k and S_ε are source terms.

The turbulent viscosity is computed by combining k and ε as follows:

$$\mu_t = \rho C_\mu \frac{k^2}{\varepsilon} \tag{3.18}$$

The constant terms in Equations 3.16, 3.17 and 3.18 have the following default values (Rodi, 1984; Fluent, 2005):

$$C_{1\varepsilon} = 1.44\,,\ C_{2\varepsilon} = 1.92\,,\ C_\mu = 0.09\,,\ \sigma_k = 1.0\,,\ \sigma_\varepsilon = 1.3$$

Versteeg & Malalasekera (1995) indicate that the mixing length and k-ε turbulence models are the most widely used and validated models. Both assume some analogy between viscous stresses and Reynolds Stresses. A limitation of these models is, however, that both assume μ_t to be isotropic, that is the ratio of the Reynolds Stress to the rate of deformation is the same in all directions.

The manner in which a turbulence model treats boundary layer or near-wall flows is very important for scour prediction. Near the boundaries in flows with high Reynolds Numbers, there is no need to integrate the k-ε model equations near the wall as the log-law for velocity (Equation 2.28) may be assumed to be valid where $30 < y^+ < 500$. At low Reynolds Numbers, however, account needs to be taken for viscous effects in the laminar sublayer. *Low Reynolds Number k-ε models* which compute the flow throughout the viscous sublayer have been developed for this purpose.

The Standard k-ε model and variations on the Standard k-ε model have been adopted in numerous studies of open channel flow as a compromise between desired accuracy and computational cost (Ali &Karim, 2002; Olsen & Kjellesvig, 1998; Ouillon & Dartus, 1997;

Rameshwaran & Naden, 2004). According to Rodi (1984), the k-ε model is one of the simplest models suitable for simulating flows involving complex geometries. This model has been successfully applied to the modelling of local scour by, amongst others, Nagata *et al.* (2002), Olsen & Melaaen (1993), Richardson & Panchang (1998) and Salehi Neyshabouri *et al.* (2003). There are, however, limitations in application of the Standard k-ε model to analysis of incipient motion where accurate representation of the turbulent boundary layer is essential. These limitations are discussed in Section 4.7.2 in the context of wall boundary conditions.

The *k-ω model* is a variation on the k-ε model where ω is the dissipation per unit turbulent kinetic energy. Another variation is the k-L model in which L introduces a length scale into the turbulence model. Details are given in Schlichting & Gersten (2000).

c) Turbulent stress models

The *Reynolds Stress Model* (RSM) is the most complex, but most general of the turbulence models discussed thus far. The RSM solves PDEs for the transport of the six Reynolds Stresses of the form:

$$\tau_{ij} = \rho \overline{u_i' u_j'} \tag{2.16}$$

In addition, a transport equation for the rate of turbulent dissipation ε is also solved. Solution of these seven PDEs results in a substantial increase in computational cost when compared to the two-equation k-ε model. The RSM, however, accounts for the anisotropy of μ_t which becomes significant near the boundaries. As already discussed, accurate representation of flow characteristics near boundaries is vital for scour prediction.

The PDEs for transport of the Reynolds Stresses may be reduced to algebraic equations under certain modelling assumptions and solved together with the transport equations for k and ε. These are called *Algebraic Stress Models* (ASMs) and provide the simplest method

of accounting for non-isotropic turbulent effects (Versteeg & Malalasekera, 1995). ASMs are more computationally economical than RSMs.

3.3.3 Choice of turbulence model

The computational economy and ease of use of a turbulence model are important for practical application to engineering problems. Rodi (1984) indicates that, although complex models that are applicable to a wide range of flows are available, such models require a substantial amount of computing power. The chosen turbulence model must achieve a balance between the desired accuracy of results and acceptable computational costs.

The turbulence models available in Fluent 6.2 are given in Section 4.5 and motivation is given for the choice of the Standard k-ε model for turbulent closure in this study based on its widespread validation, computational economy and satisfactory performance in previous numerical studies of local scour.

3.4 Past and recent research in numerical modelling of local scour

3.4.1 Numerical modelling of flow and local scour at piers

A key study in the early development of numerical models for the computation of local scour at piers was the investigation of Olsen & Melaaen (1993). The three-dimensional non-transient flow field was computed by a finite volume CFD code and the k-ε model was employed for turbulent closure. The sediment concentration in wall-adjacent cells was solved from a convection-diffusion equation based on bed shear stress. Solution of a continuity equation for sediment concentration gave changes in the bed elevation.

Although the computational grid and time steps employed by Olsen & Melaaen (1993) were coarse relative to those which can be used with greater computing power today, the model results were encouraging and in good agreement with experimental data. The

numerical model correctly predicted formation of the horseshoe vortex upstream of the pier and flow separation in the wake.

Olsen & Kjellesvig (1998) adopted an approach similar to that of Olsen & Melaaen (1993) but extended the model to simulate the temporal development of a local scour hole at a pier by incorporating time dependence and using an adaptive grid to follow the changes in bed and free surface elevation. Reasonable agreement with empirical formulae was reported. It is felt that comparison to empirical formulae is a poor method for evaluating the performance of numerical models for local scour and that comparison to field or physical model data is more appropriate. The inconsistency of empirical formulae and the need to move towards alternative methods for local scour prediction was highlighted in Section 2.10.3. The numerical model output in the current study is thus compared to physical model data.

Richardson & Panchang (1998) used the commercial CFD code FLOW-3D to model the flow field around a circular cylinder. The 3D model produced accurate representations of salient flow features such as vertical downflow at the upstream face of the pier, the horseshoe vortex and separation in the horizontal plane in the pier wake.

Ali & Karim (2002) used Fluent to simulate flow over rigid beds and in scour holes but they represented the free surface by means of a "rigid lid" boundary which did not allow water level fluctuations with scour hole development. McGahey (2001) modelled flow and incipient motion at piers and abutments using the CFD code CFX and employed a moving wall to represent the free surface. McGahey recommended investigation of alternative free surface routines which allow fluctuation of the water level around the obstacles to improve scour predictions. A multiphase free surface routine, in which the stratified flow of air and water are modelled, is employed in the current study in an attempt to account for the effects of the bow wave at the upstream face of the pier and downflow at the pier sides on the flow.

In more recent numerical models for local scour such as that of Nagata *et al.* (2002), investigators have attempted to simulate the temporal development of scour holes using automated procedures for channel bed deformation and mesh adjustment. Increases in

computing power and more sophisticated mesh generation routines continue to make unsteady simulation of scour hole development a more attractive option for local scour modelling.

Nagata *et al.* (2002) coupled a momentum equation for sediment motion to stochastic models for sediment entrainment and deposition. Reasonable agreement with laboratory data was obtained and it was noted that further development of the bed deformation model was necessary. The current study aims to investigate a very simplified manual bed deformation model.

3.4.2 Numerical modelling of flow and local scour at abutments

In the following review, the term "abutments" is used in a general sense to describe abutments and related structures such as spur dikes and groynes.

Ouillon & Dartus (1997) applied a three-dimensional model to computation of flow around a groyne and assessed the performance of a "rigid lid" model against a free surface model using the "porosity method" for free surface tracking. The free surface model produced a substantial improvement in prediction of the reattachment length compared to the rigid lid model. The rigid lid model also underpredicted bed shear stresses due to the artificial generation of shear stress at the upper rigid lid boundary.

Biglari & Sturm (1998) used a two-dimensional depth-averaged finite volume code to compute flow around abutments and validated the model against experimental data. Good agreement between the free surface variations and velocity fields found in the numerical and physical models was obtained. The investigators did, however, indicate the need to quantify the effects of "additional local hydraulic variables", which could only be accurately predicted by a three-dimensional model, on abutment scour.

A two-dimensional depth-averaged model was also applied to flow computation at a groyne by Tingsanchali & Maheswaran (1990). They introduced an empirical three-

dimensional correction factor to improve agreement between the bottom shear stresses computed by the numerical model and those measured in the laboratory.

3.5 Conclusions

The application of numerical models which solve the Reynolds-Averaged Navier-Stokes equations to solve hydraulic engineering problems such as prediction of local scour has undergone rapid development in the past few decades. The k-ε turbulence model has been widely applied to turbulence modelling in three-dimensional flows at obstacles such as pier and abutments as it provides fair computational economy whilst still preserving salient features of the flow important for scour estimation.

Studies in numerical modelling of local scour have recently become increasingly focussed on the three-dimensional representation of flow patterns at obstacles such as piers, abutments, groynes and spur dikes. The need for accurate reproduction of three-dimensional flow patterns responsible for local scouring and appropriate boundary conditions at the free surface has been recognised. Automation of the temporal evolution of local scour holes at piers and similar obstacles by coupling sediment transport routines to existing commercial numerical models is also under development.

Chapter 4
Methods Adopted for Numerical Modelling

Modelling procedures adopted in numerical simulation of fluid flow and local scouring have significant effects on the quality and reliability of the model output. In this chapter, the physical models selected for numerical simulation are described. The construction and subdivision of the computational domain, definition of fluid properties, choice of turbulence and free surface models, boundary conditions and solver controls are then discussed. Techniques investigated for manual bed adjustment to simulate temporal scour hole development are also detailed.

4.1 Physical models simulated and computational domain

Local scour studied in four small-scale physical models was simulated numerically in this investigation. Relevant details of the physical models and the geometries of the computational domain adopted for numerical modelling are described below. Motivation for the selection of the domain extents is given in later sections in the context of free surface modelling and boundary conditions.

4.1.1 Initiation of scouring at a circular pier (Midgely, 2000)

Midgely (2000) investigated the initiation of scouring of a thin layer of uniform quartzitic sand subject to steady flow at a 45 mm diameter circular pier placed centrally in a 0.610 m wide laboratory flume. The extent of the scoured area after equilibrium had established was measured for different flow rates and sediment particle diameters.

The test case simulated numerically had a flow rate of 7.69 l/s, flow depth of 74.4 mm and Froude Number of 0.20. The median sediment particle diameter was 0.55 mm and the sand had a settling velocity of 0.089 m/s. This test case was selected as it was also

modelled numerically by McGahey (2001). The findings of this study are therefore compared to both the physical data of Midgely (2000) and numerical scour predictions of McGahey (2001) in Chapter 5.

The computational domain defined for numerical simulation of the Midgely experiment is shown in Figure 4.1. The flow was assumed to be symmetrical through the pier centreline allowing only half of the flume width to be modelled.

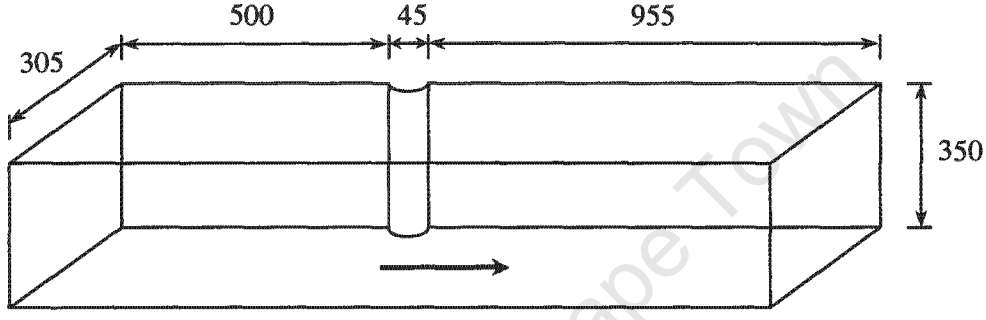

Figure 4.1: Computational domain for initiation of local scouring at a circular pier (Midgely, 2000). All dimensions are in millimetres.

4.1.2 Initiation of scouring at a rectangular abutment (Mitchell, 2000)

The initiation of local scouring of uniform quartzitic sand at a rectangular abutment was studied experimentally by Mitchell (2000). A rectangular abutment 35 mm thick and protruding 220 mm into the flow at a right angle to the channel wall was fixed in an 820 mm wide flume. The lateral extent of the scoured region established under steady flow conditions was measured for a range of flow rates and sediment particle sizes.

For numerical simulation, the test case with a flow rate of 10.2 l/s, flow depth of 100.0 mm and Froude Number of 0.13 was chosen. The median sand particle diameter was 0.55 mm and the sediment had a settling velocity of 0.089 m/s. The computational domain is illustrated in Figure 4.2. This case was also modelled numerically by McGahey (2001).

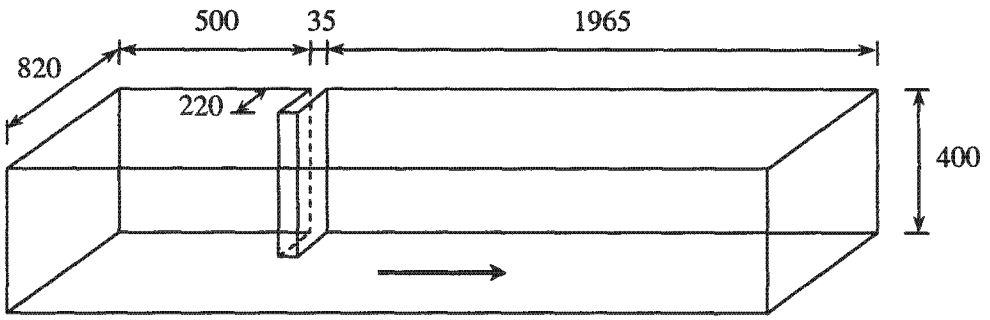

Figure 4.2: Computational domain for initiation of local scouring at a rectangular abutment (Mitchell, 2000). All dimensions are in millimetres.

4.1.3 Scour hole development at a semi-circular abutment (Unger & Hager, 2005)

Unger & Hager (2005) studied internal flow features in a clear-water scour hole at a semi-circular abutment using Particle Image Velocimetry (PIV). The flow features were recorded during development of the scour hole at nine intervals from $t = 60$ s to $t = 86\,400$ s (24 hours). The experiment was conducted in a 1000 mm wide flume with a flow rate of 70 l/s, flow depth of 182 mm and Froude Number of 0.29. Scouring of uniform quartzitic sand with a median diameter of 1.1 mm around the 260 mm diameter abutment was measured. The scour hole which had developed after 24 hours was not an equilibrium clear-water scour hole.

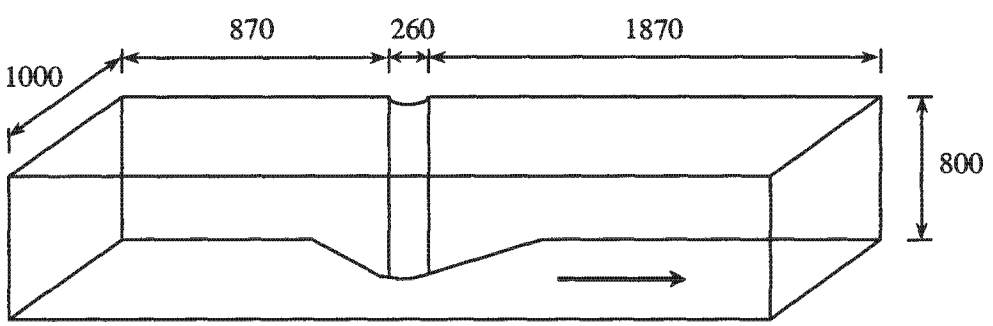

Figure 4.3: Computational domain for simulation of flow in a developed scour hole at a semi-circular abutment (Unger & Hager, 2005). All dimensions are in millimetres.

Steady flow through the scour hole measured by Unger & Hager (2005) after 24 hours was simulated numerically in this study as a rigid bed model. The computational domain and assumed bathymetry of the scour hole are shown in Figures 4.3 and 4.4 respectively.

The precise bathymetry measured in the physical model was available for the grey shaded region of Figure 4.4. Extrapolation of the measured depth contours outside this region was necessary for generation of the complete scour hole in the pre-processing stage.

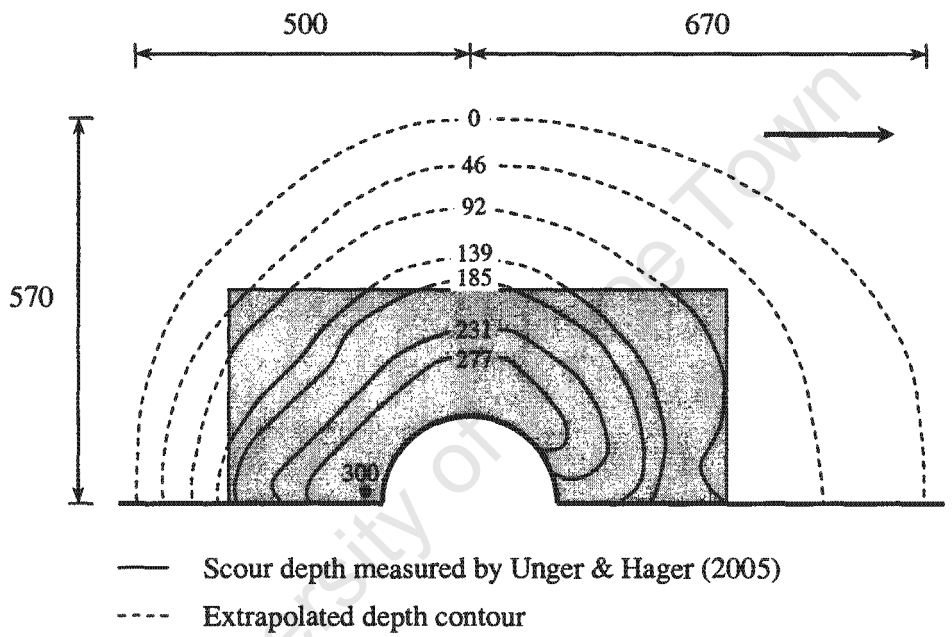

Figure 4.4: Bathymetry of scour hole at semi-circular abutment after 24 hours (Unger & Hager, 2005). All dimensions are in millimetres.

4.1.4 Scour hole development at a circular pier (Ahmed, 1995)

Ahmed (1995) investigated the flow features and patterns of erosion and deposition around a circular pier by means of physical models. The test case selected for numerical simulation involved scouring of uniform quartzitic sand with a median diameter of 0.88 mm and 35° angle of repose at a 64 mm diameter pier placed centrally in a 1.22 m

wide flume. A steady flow rate of 50 l/s, approach depth of 182 mm and Froude Number of 0.17 were used.

The scour hole bathymetry was measured at ten intervals during the experiment along the flume centreline upstream and downstream of the pier and at right angles to this centreline. An equilibrium clear-water scour hole with a maximum depth of 54 mm was established after approximately 220 hours in the physical model.

This test case studied by Ahmed (1995) was chosen for numerical modelling using manual bed adjustment to simulate scour hole development. The extent of the computational domain is illustrated in Figure 4.5. For the manual bed adjustment simulations, the scour hole bathymetry at each step was computed from the applied stream power on the channel bed from the previous step. Methods for computing the scour hole geometry are detailed in Section 4.10 and the computed results are presented in the findings of Chapter 5.

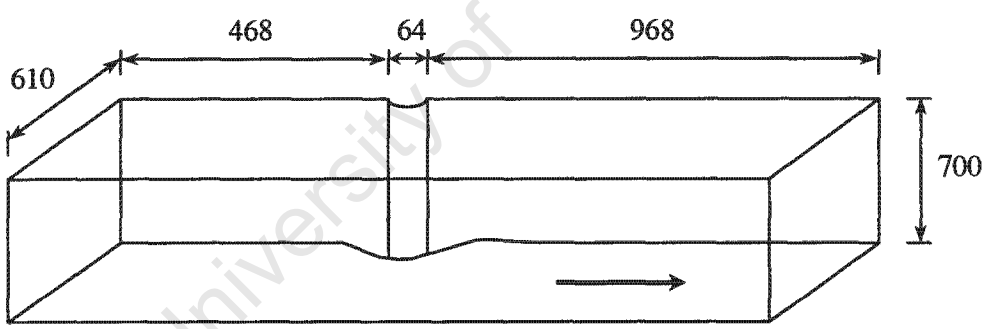

Figure 4.5: Computational domain for scour development at a circular pier employing manual bed adjustment (Ahmed, 1995)

4.2 Fluent 6.2 CFD code and problem dimensionality

Fluent 6.2 is a general finite volume CFD code with a wide range of applications. This code was used for numerical simulations which were implemented on a personal computer with a 2.8 GHz Pentium 4 processor and 2 GB RAM.

The three-dimensional version of Fluent 6.2 was applied model the flow features associated with local scour which are strongly three-dimensional. The importance of full three-dimensional representation in local scour modelling has been recognised by previous investigators (Section 3.4). Richardson & Panchang (1998) criticised two-dimensional depth-averaged approaches to simulating local scour as two-dimensional models are incapable of representing the partial reversal of the pressure distribution at the upstream faces of obstacles such as piers and the associated downflow which is key to the development of the horseshoe vortex and local scour.

4.3 Domain subdivision and mesh generation

The pre-processor Gambit 2.2 was used to generate the geometry of the computational domain and subdivide this domain into a mesh of control volumes or cells. The number of cells varied from 400 000 for the pier of Ahmed (1995) to 800 000 for the rectangular abutment (Mitchell, 2000). The chosen number of cells was limited by the available computational capacity. Memory problems were encountered when more than 10^6 cells were used for simulation of flow around the rectangular abutment.

Quadrilateral mesh elements were used throughout and, where possible, cells were aligned with the flow to minimise false diffusion. Structured meshes were used in the vertical x-y and z-y planes.

The mesh was refined around the obstacles where large velocity gradients were expected and, where relevant, in the scour holes where details of the flow features are of interest. The vertical cell dimensions were dictated by the chosen free surface model and the boundary conditions, which are discussed in Sections 4.6 and 4.7 respectively.

4.4 Fluid and sediment properties

4.4.1 Properties of water and air

a) Density

At atmospheric pressure and an ambient temperature of 20°C, the density of water, ρ, is 998.2 kg/m^3 (Chanson, 2004). The variation of ρ with pressure and temperature may frequently be neglected in open channel flow problems and the simplification $\rho = 1000$ kg/m^3, which is valid at 0°C and 1.0 atm, is frequently used (Chadwick & Morfett, 1998; Raudkivi, 1998). Fluent uses $\rho = 998.2$ kg/m^3.

The density of air ρ_a varies markedly with changing pressure, temperature and humidity (Raudkivi, 1998). The value of ρ_a at atmospheric pressure and 20°C is approximately 1.2 kg/m^3 (Chanson, 2004). Values of ρ_a at various pressures, temperatures and humidities are tabulated by Raudkivi (1998).

b) Viscosity

The dynamic molecular viscosity of water at 20°C and 1.0 atm is 1.005 x 10^{-3} Ns/m^2 (Chanson, 2004). It is a function of temperature T (°C) and may be evaluated from the following relationship presented by Raudkivi (1998):

$$\mu_l = \frac{1.79 \times 10^{-3}}{1 + 33.68 \times 10^{-3} T + 2.21 \times 10^{-4} T^2} \tag{4.1}$$

For water, Fluent uses $\mu_l = 1.003$ x 10^{-3} Ns/m^2. The turbulent viscosity μ_t is computed in the solution process from Equation 3.18 in the k-ε turbulence model.

4.4.2 Sediment properties

It must be emphasised that the presence of sediment particles in the flow was not accounted for. Instead, the fluid flow was computed by the numerical model and the scour and deposition estimated from the Movability Numbers and power dissipation at the channel bed. The only way in which sediment properties were included in the numerical model was in the channel bed roughness which is required for the calculation of the velocity distribution in the boundary layer. Since uniform sediments were used throughout, it was assumed that the roughness height k_s could be set equal to the median diameter d_{50} of the sediment.

4.5 Turbulence modelling

4.5.1 Available turbulence models in Fluent 6.2

A selection of classical turbulence models was reviewed in Section 3.3.2. The following turbulence closure schemes are available in Fluent 6.2 (Fluent, 2005):

Spalart-Allmaras Model: A one-equation model originally developed for aerospace applications that solves for the turbulent eddy viscosity.

Standard k- ε model: A two-equation model that solves transport equations for the turbulent kinetic energy k and dissipation rate ε.

Renormalization-Group (RNG) k-ε model: A modified k- ε model giving better accuracy than the standard model in rapidly-strained flows.

Realizable k-ε model: A k- ε model with different formulations for the turbulent viscosity and dissipation rate. This model satisfies certain mathematical constraints on the Reynolds stresses, consistent with the physics of turbulent flows.

Standard k-ω model: A two-equation model that solves transport equations for the turbulent kinetic energy k and dissipation per unit turbulent kinetic energy ω and includes modifications for low Reynolds Number effects.

Shear-stress transport (SST) k-ω model: A model combining the k-ω model which is accurate in the near-wall region and the k-ε model in regions further from walls.

Reynolds Stress Model (RSM): The RSM is the most complex turbulence model supported by Fluent 6.2 and solves transport equations for the Reynolds Stresses and dissipation rate ε.

Large Eddy Simulation (LES): Intermediate between DNS and RANS turbulence modelling in terms of the degree of modelling. The Navier-Stokes equations are solved for the largest eddies in the flow and smaller eddies are modelled.

Detached Eddy Simulation (DES): A coupling of the LES and the Spalart-Allmaras model for applications in which classical LES is computationally unaffordable.

4.5.2 Selection of the standard k-ε turbulence model

The turbulence model is generally considered to be the most sensitive factor in numerical studies of flow features (Ouillon & Dartus, 1997). A number of comparative studies on the performance of various turbulence models for application to local scour prediction have been undertaken (Christian & Corney, 2004; Karim & Ali, 2000; Liang & Cheng, 2005; Liang *et al.*, 2005; Richardson & Panchang, 1998).

As the computational expense of direct numerical simulation (DNS) of turbulent open channel flow is currently excessive, turbulence models and in particular the k-ε model and its variations have been adopted in numerous studies as a compromise between the desired accuracy and computational cost (Ali & Karim, 2002; Olsen & Kjellesvig, 1998; Ouillon & Dartus, 1997; Rameshwaran & Naden, 2004). According to Rodi (1984), the k-ε model is one of the simplest models suitable for simulating flows involving complex geometries.

This model has been successfully applied to the modelling of local scour by, amongst others, Nagata *et al.* (2002), Olsen & Melaaen (1993), Richardson & Panchang (1998) and Salehi Neyshabouri *et al.* (2003).

Ali & Karim (2002) compared the Standard and RNG k-ε models in predicting flows in scour holes at a pier and found the flow patterns and shear stresses predicted by the two models to be "virtually identical".

Salaheldin *et al.* (2004) assessed the performance of the Standard, RNG and Realizable k-ε models and the RSM in Fluent for simulating separated turbulent flows at circular piers. They concluded that the Standard and RNG k-ε models can be used to compute flow near the pier although they slightly overestimate velocities near the bed. The Realizable k-ε model significantly overestimated velocities near the bed even though it is supposedly superior for flows in which there are vortices, rotation and strong streamline curvature. The study also suggested that further validation of the RSM is required before it can be used confidently for local scour modelling.

McGahey (2001) used the CFD code CFX 4.3 to simulate flow over bedforms analysed by means of a physical model by Cellino & Graf (2000). McGahey compared the shear stress and velocity distributions with depth predicted by the Algebraic Stress Model (ASM) and the Standard k-ε turbulence model. The k-ε model produced both shear stress and velocity distributions closer to the experimental measurements than the ASM did.

The Standard k-ε model was adopted for turbulent closure in this study based on its computational economy and extensive validation in application to open channel flows and local scour prediction. A number of variations on the Standard k-ε model and k-ω model are available in Fluent 6.2. These alternatives promise improved performance under certain flow conditions such as in near-wall regions or rapidly-strained and rotating flows. They have, however, not been as widely validated as the Standard k-ε model. The Standard k-ε model was thus selected.

4.6 Free surface modelling

A number of investigators (Ali & Karim, 2002; McGahey, 2001; Ouillon & Dartus, 1997) have noted the importance of accurate representation of the free surface in numerical models of open channel flow. Rameshwaran & Naden (2004) modelled the free surface variations in a meandering channel. Their results showed that the free surface treatment for the spatial variation of the water surface is vital for accurate prediction of bed shear stress. Appropriate representation of the free surface is thus crucial for accurate local scour prediction.

4.6.1 Available multiphase models in Fluent 6.2

The multiphase models available in Fluent 6.2 are listed below. Most are not suitable for application to stratified or free surface flow, but are nevertheless listed for completeness. The following multiphase models are available (Fluent, 2005):

Volume of Fluid (VOF) model: For simulation of the flow of two or more immiscible fluids, the VOF model solves an equation for the volume fraction of each fluid in each cell. This model is appropriate for stratified or free surface flows.

Mixture model: The mixture model, unlike the VOF model, allows the two fluids to interpenetrate and move at different velocities by specification of slip velocities. It is a simplified multiphase model, allowing differential movement between the phases but assuming equilibrium over short length scales.

Eulerian model: The Eulerian model is the most complex and computationally expensive multiphase model available in Fluent as it applies an Eulerian treatment to every phase defined. Details are given in the Fluent Users Guide (Fluent, 2005). Both the Mixture and Eulerian models are appropriate for flows in which the phases mix or separate and / or where the dispersed-phase volume fractions exceed 10%.

Discrete phase model: The discrete phase model is appropriate where the dispersed-phase volume fractions are less than or equal to 10% and it applies a Eulerian-Lagrangian treatment to the two phases. Details may be found in the Fluent Users Guide (Fluent, 2005).

Wet steam model: This model is applicable to simulation of vapour condensation in steam turbines.

4.6.2 Implementation of the VOF model for free surface flow

The VOF model was selected for free surface tracking. It is the only multiphase model in Fluent 6.2 suitable for simulating the stratified or free surface flow in open channels. In the VOF model, tracking of the interface between two phases is accomplished by solution of a scalar transport equation for one of the phases.

In this study, both the air and water phases were modelled as incompressible fluids. Air was specified as the primary phase and water as the secondary phase.

The height (in the *y*-direction) of the computational domain was dictated by the requirements of the free surface model. Salaheldin *et al.* (2004) modelled the three-dimensional flow field around circular piers and found that if, at the inflow boundary, the ratio of the air depth to the water depth exceeds one-third, there is no effect from the boundary at the top of the domain on the water flow.

Cunninghame (2003), however, found when using the VOF model for open channel flow in Fluent 6.1, that mixing of the air and water occurs in long domains if the air occupies less than about two-thirds of the domain depth. The height of the domain was thus chosen so that the air volume occupied at least three-quarters of the domain depth.

4.7 Boundary conditions

4.7.1 Upstream and downstream boundary conditions

a) Available inflow and outflow boundary conditions in Fluent 6.2

The following ten boundary conditions are available for specification of flow properties at flow inlets and outlets in Fluent 6.2 (Fluent 2005):

Velocity inlet: The velocity inlet condition is used to define the velocity distribution and scalar properties at flow inlets.

Pressure inlet: May be used to define the total pressure and other scalar quantities at flow inlets.

Mass flow inlet: This boundary condition is used in compressible flows to prescribe a mass flow rate at an inlet.

Pressure outlet: Used to define the static pressure at flow outlets as well as other scalar variables in case of backflow.

Pressure far-field: This boundary condition is available for free-stream compressible flows. Static conditions and a free-stream Mach number are specified.

Outflow: Used to model flow exits where details of the flow velocity and pressure are not known prior to solution. The outflow boundary condition assumes a zero normal gradient for all flow variables except pressure. It is thus appropriate where the exit flow is fully developed.

Inlet vent: This boundary condition is used to model an inlet vent with a specified loss coefficient, flow direction, and ambient total pressure and temperature.

Intake fan: Used to model an external intake fan with a specified pressure jump, flow direction, and ambient (intake) total pressure and temperature.

Outlet vent: For modelling an outlet vent with a specified loss coefficient and ambient (discharge) static pressure and temperature.

Exhaust fan: This boundary condition may be used to model an external exhaust fan with a specified pressure jump and ambient static pressure.

b) Application of the velocity inlet boundary condition

Initially, the *velocity inlet* condition was applied to the upstream flow inlet boundary and the *outflow* condition was used at the downstream outlet boundary. It was however found that, over the length of the domain, the water level dropped from the specified depth h at the inflow to approximately $h/2$ at the outflow. Application of the *velocity inlet* condition at both the inlet and outlet boundaries remedied this problem by enforcing the desired velocity distributions at both ends of the domain. The exit length was made sufficiently long to allow development of a reasonably uniform velocity profile downstream of the obstacle.

Point velocities, values of the turbulent parameters k and ε, and the water volume fractions were specified at the upstream and downstream boundaries. The values of k, ε and water volume fractions specified at the outlet were only used in the computation if backflow occurred through the outlet during the solution procedure.

The velocity distributions in the water at the upstream and downstream boundaries were computed from the following equations given by Rooseboom (1992) and also employed in the numerical model developed by McGahey (2001). For flow in an infinitely wide channel, the following velocity distribution was applied:

$$u(y) = \frac{\ln\left(\frac{y}{y_0}\right)}{\ln\left(\frac{h}{ey_0}\right)}U \tag{4.2}$$

Where the flow was subject to the influence of channel sidewalls, u was computed as:

$$u(y,z) = \frac{\ln\left(\frac{y}{y_0}\right)\ln\left(\frac{B/2-|z|}{z_0}\right)}{\ln\left(\frac{h}{ey_0}\right)\ln\left(\frac{B/2}{ez_0}\right)}U \tag{4.3}$$

where h and B are the water depth and channel breadth respectively and y_0 and z_0 are the distances from the walls at which the velocity magnitude is mathematically equal to zero. Simons & Senturk (1977) suggested that y_0 can be related to the wall roughness as follows:

$$y_0 = \frac{k_s}{29.6} \tag{4.4}$$

For a 1mm roughness height for example, $y_0 = 3.4 \times 10^{-5}$ m. It was assumed that for the flume walls, $z_0 = 10^{-6}$ m. The values of k and ε at the inflow were estimated from the following relationships (McGahey, 2001) and, like the velocities, were specified as point values:

$$k = 1.5(0.037u)^2 \tag{4.5}$$

$$\varepsilon = \frac{k^{1.5}}{0.3R} \tag{4.6}$$

where R is the hydraulic radius.

The inlet and outlet velocity distributions for the air region were estimated from those calculated for the water. The air velocity near the free surface was set equal to the free surface water velocity computed from Equation 4.2 or 4.3.

Identical u, k, ε and water volume fraction profiles were applied to both the inlet and outlet boundaries to ensure mass conservation across the domain. Point profiles of u, k, ε and water volume fraction were defined by means of .txt files which were read into Fluent. The profile files for the inlet and outlet velocity, for example, listed the point velocities at typically 100 points on the boundary faces in the format (x, y, z, u). Fluent would then assign a velocity to each cell face on the boundary from the nearest point in the profile file.

A reference pressure of 101.3 kPa was specified at the upper boundary of the domain at the inflow.

4.7.2 Wall boundary conditions

The *wall* boundary condition was applied to the channel bed, upper boundary of the domain enclosing the air volume and, where relevant, to channel walls. The faces of piers and abutments were also specified using the *wall* condition.

Attention was paid in particular to treatment of the channel bed. Accurate simulation of flow in the turbulent boundary layer is essential for accurate prediction of incipient motion and hence scour and deposition. In a numerical study of local scour at bridge piers, Richardson and Panchang (1998) observed that without fully-developed boundary layer flow upstream of the obstacle, the horseshoe vortex which is a key mechanism in scour development at piers, does not develop. This illustrated the importance of correct representation of the boundary layer for scour prediction.

Cunninghame (2003) found that the coupling of the standard k-ε model with inappropriate mesh vertical sizing in the vicinity of the channel bed can yield unrealistic velocity gradients near the bed and hence unreliable scour predictions.

There are generally two approaches to modelling the wall region (Figure 4.6). In a *wall function* approach, a coarse mesh and the log-law for velocity (Equation 2.28) are used to model flow in the boundary layer. Alternatively, a *near-wall* modelling technique may be adopted in which the viscous sublayer of the boundary is fully resolved by means of a very fine mesh.

The near-wall approach was adopted for simulation of incipient motion in the rigid flat-bed models of Midgely (2000) and Mitchell (2000). A boundary cell height of approximately 0.13 mm corresponding to $y^+ \approx 1$ at the wall-adjacent cell centre was applied. Cunninghame (2003) found that this near-wall approach gave a shear stress distribution closer to the theoretical linear distribution in uniform open channel flow than the wall function approach did.

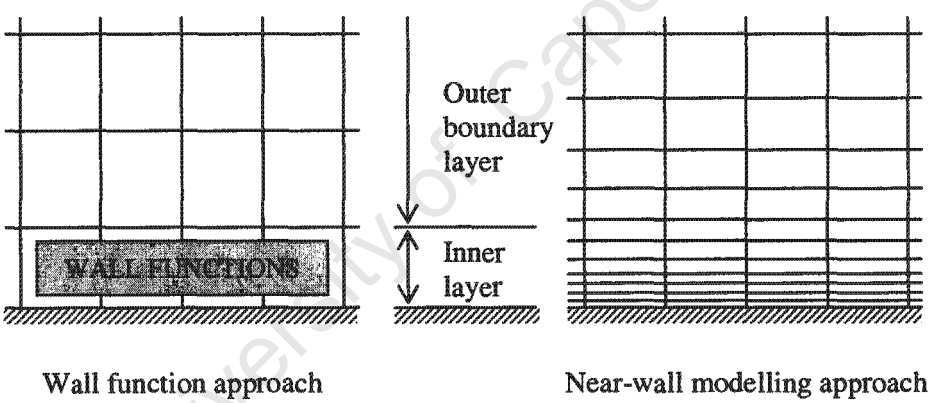

Figure 4.6: The wall function and near-wall approaches for modelling flow near wall boundaries

For simulation of flow over deformed channel beds and through scour holes in the models of Unger & Hager (2005) and Ahmed (1995), the wall function approach was applied. The height of bed-adjacent cells was chosen to correspond to $y^+ \approx 30$ so that the viscous and transitional regions of the turbulent boundary layer were enclosed in the wall-adjacent cells. It is difficult to implement the fine mesh required by the near-wall model on deformed channel beds as cells near the bed with high aspect ratios become excessively

skewed unless the mesh is as fine in the horizontal plane as it is in the vertical direction. The computational demands of simulation of flows with such a fine mesh would be immense. The wall function approach to modelling turbulent boundary layers has been adopted in a number of studies of local scour (Kajikawa *et al.*, 2004; Liang *et al.*, 2005; Ouillon & Dartus, 1997; Rameshwaran & Naden, 2004; Salaheldin *et al.*, 2004; Salehi Neyshabouri *et al.*, 2003).

4.7.3 Symmetry planes

The *symmetry* boundary condition was applied through the channel centreline for the simulation of flow around the piers of Midgely (2000) and Ahmed (1995) to reduce the domain size and hence computational demand.

The pier of Midgely was simulated in steady state simulations with and without the assumption of symmetry about the channel centreline. No difference could be discerned between the scour patterns predicted by the two models. The symmetry condition along the channel centreline was applied thereafter.

The *symmetry* condition in Fluent assumes zero flux of all quantities across the boundary. The normal velocities and gradients of all variables at symmetry planes are thus zero.

4.8 Solver controls

4.8.1 Precision

The double precision segregated solver was used in the solution process. This solver computes the values of variables to 12 as opposed to the 6 significant figures used by the single precision solver. Use of the double precision solver prevents mixing of the air and water phases due to cumulative rounding errors in the volume fraction calculations. Mixing of the two phases can occur in long domains and when fine meshes are used.

4.8.2 Time dependence

The pier of Midgely (2000) was simulated in both transient and steady state analyses to investigate whether it was necessary to perform time-dependant simulations. The results of the steady and unsteady analyses were virtually identical. Steady state models were therefore used for the remainder of the study.

4.8.3 Differencing schemes

In the finite volume method, the governing equations in integral form are discretised by means of differencing schemes which describe the way in which the unknown value of a variable is computed from known values in neighbouring cells. Details of the computation methods used in these discretisation schemes are not given here but may be found in, for example, Versteeg & Malalasekera (1995).

a) Pressure interpolation

The following schemes are available for pressure interpolation in Fluent 6.2:

Standard: Interpolates pressure values at cell faces using momentum equation coefficients. This is the default scheme in Fluent.

Linear: Computes face pressure as the average of values in neighbouring cells.

Second-order: This scheme reconstructs face pressures in the manner used for second-order accurate convection terms and is recommended for compressible flows.

Body-force-weighted: Computes the face pressures assuming that the normal gradient of the difference between pressure and body forces is constant. This scheme is recommended for flows involving large body forces.

PRESTO (Pressure staggering option): Applies a continuity balance to calculation of pressure in a "staggered" control volume to give face pressures on the actual grid.

The *PRESTO* scheme was applied in this study. It is recommended for pressure interpolation when using the VOF multiphase model (Fluent, 2005).

b) Pressure-velocity coupling

The following four pressure-velocity coupling methods are available with the segregated solver in Fluent 6.2:

SIMPLE: The default pressure-velocity coupling in Fluent.

SIMPLEC (Simple-Consistent): Contains modifications to the SIMPLE scheme which allows use of higher under relaxation factors to speed up convergence.

PISO: Commonly used for transient simulations.

FSM (Fractional Step Method): For time-dependant flows using non-iterative time advancement. The FSM is slightly less computationally expensive than PISO.

SIMPLEC was applied to the pressure-velocity coupling in this study. The default *SIMPLE* scheme applies larger velocity corrections at each iteration than the *SIMPLEC* scheme does. These larger corrections can cause oscillation of the solution, hindering convergence.

c) Momentum, velocity, k, ε and water volume fraction

There are about nine general discretisation schemes available in Fluent 6.2, only some of which are applicable to this study. The following schemes may be applied to discretisation

of momentum, velocity, turbulent quantities and the water volume fraction in the VOF model:

First-order upwind: Face values of variables are set equal to the values at neighbouring cell centres. The first-order upwind scheme is comparatively stable but gives relatively poor accuracy where the flow is not aligned with the cells.

Power law: The face value of a variable is interpolated by solution of a one-dimensional convection-diffusion equation.

Second-order upwind: This scheme employs a multi-dimensional linear reconstruction approach.

QUICK: The *QUICK* scheme fits a quadratic function to values of a variable at three neighbouring cells but is weighted towards the values in the upstream direction. It is thus based on a weighted average of the second-order-upwind and central interpolations of the variable.

Third-order MUSCL: This scheme is a blend of the central differencing and second-order upwind schemes.

Each problem was initially solved using the *first-order upwind* scheme as it is stable and computationally economical, though less accurate than other schemes. Thereafter the *QUICK* scheme was applied as it yields superior accuracy. The *QUICK* scheme is also recommended for discretisation of the volume fraction equation in the VOF model to sharpen the air-water interface.

4.8.4 Under-relaxation

Under-relaxation factors are employed to limit the amount by which the value of a variable is corrected from one iteration to the next to prevent solution oscillation and control convergence. Appropriate relaxation factors preventing numerical oscillation without

increasing solution time unnecessarily were determined through trial and error. Relaxation factors between 0.1 and 0.5 were used for all steady state simulations.

4.8.5 Solution initialisation and convergence criteria

At the start of the solution process the initial velocity, k and ε values throughout the domain were set equal to the average values specified at the inlet and outlet boundary faces. Water volume fractions of 0 and 1 were patched to the air and water volumes respectively.

Residuals were used to monitor solution convergence. A residual is the flux imbalance of a property summed over all cells in the computation domain and scaled by the flow rate through the domain. When all the residuals had decreased by three orders of magnitude, the solution was said to have converged.

4.9 Definition of the scour parameters and selection of critical values

Sediment transport parameters such as the Movability Number, power dissipation function and slope angles were defined through the *Custom Functions* panel in Fluent 6.2. The critical values of the Movability Number and applied stream power for incipience on flat beds are also discussed below.

4.9.1 Movability Number

The Movability Number was computed from the bed shear stress and shear velocity as follows:

$$\tau_0 = \tau_{xy} = \mu\left(\frac{\partial u}{\partial y} + \frac{\partial v}{\partial x}\right) \tag{4.7}$$

$$u_* = \sqrt{\frac{\tau_0}{\rho}} \tag{2.21}$$

$$Mn = \frac{u_*}{v_{ss}} \tag{2.36}$$

The particle settling velocity v_{ss} was either obtained from laboratory measurements (Midgely, 2000; Mitchell, 2000) or computed using the empirical formula of Cheng (1997) (Equation 2.9) where laboratory measurements were not available (Ahmed, 1995; Unger & Hager, 2005).

The critical value of *Mn* for incipience $Mn_{c,0}$ was selected from the numerical model output for incipient motion at the pier of Midgely (2000) and abutment of Mitchell (2000). Both models predicted *Mn* in the range 0.10 to 0.15 upstream of the respective obstacles. Adoption of the criterion of Rooseboom (1992) for turbulent boundaries, $Mn_{c,0} = 0.12$, would thus imply that live-bed conditions existed upstream of the pier and abutment. These were, however, both clear-water scour experiments. The criterion for incipience in turbulent boundaries $Mn_{c,0} = 0.17$, developed by Armitage (2002), which implies a higher intensity of motion, was thus adopted.

4.9.2 Power dissipation function

The applied stream power was computed as follows from the power dissipation function after Armitage (2002) using the velocity gradients determined in the solution:

$$P_t \equiv \Phi = \mu\left[2\left(\left(\frac{\partial u}{\partial x}\right)^2 + \left(\frac{\partial v}{\partial y}\right)^2 + \left(\frac{\partial w}{\partial z}\right)^2\right) + \left(\frac{\partial u}{\partial y} + \frac{\partial v}{\partial x}\right)^2 + \left(\frac{\partial u}{\partial z} + \frac{\partial w}{\partial x}\right)^2 + \left(\frac{\partial v}{\partial z} + \frac{\partial w}{\partial y}\right)^2\right] \tag{3.11}$$

The power required to suspend a sediment particle, P_r, was computed as:

$$P_r = (\rho_s - \rho) g v_{ss} \tag{2.48}$$

The settling velocity v_{ss} was obtained from laboratory measurements where these were available. It was otherwise calculated from the empirical formula of Cheng (1997) (Equation 2.9). The critical applied stream power for incipience on a flat channel bed $P_{t,c,0}$ was computed as follows:

$$P_{t,c,0} = \eta P_r \tag{2.50}$$

The η value determined by Armitage (2002) of 1/67 for turbulent boundaries was used in this study. This value was chosen to be consistent with the adopted value of $Mn_{c,0}$ in terms of the intensity of motion. In other words, the critical values $Mn_{c,0} = 0.17$ and $P_{t,c,0} = P_r / 67$ both imply an intensity of motion of $I = 2 \times 10^{-5}$ s^{-1}.

4.9.3 Slope correction

a) Longitudinal bed slope

The longitudinal slope β was computed from the angle the velocity vector makes with the horizontal plane. It was assumed that the velocity vector is approximately parallel to the channel bed. The angle β was computed from the velocity components as follows:

$$\beta = \arctan\left(\frac{-v}{\sqrt{u^2 + w^2}}\right) \tag{4.8}$$

β is measured positive downwards from the horizontal plane.

b) Transverse bed slope

The transverse slope γ was computed as the angle between a transverse vector **t** (t_x, t_y, t_z) in the plane of the boundary and the horizontal plane. The transverse vector **t** is perpendicular to **u** and was computed from the cross product of the boundary normal **n** (n_x, n_y, n_z) and **u** (u, v, w) as follows (McGahey, 2001):

$$\mathbf{t}(t_x, t_y, t_z) = (vn_z - wn_y, wn_x - un_z, un_y - vn_x) \tag{4.9}$$

The transverse slope angle γ was then given by:

$$\gamma = \arctan\left(\frac{t_y}{\sqrt{t_x^{\,2} + t_z^{\,2}}}\right) \tag{4.10}$$

Normal vectors are not readily accessible in Fluent 6.2. The boundary normal vector **n** was thus computed from the projected boundary face areas which are computed by the solver. If the face areas projected onto planes normal to the x, y and z co-ordinate directions are A_x, A_y and A_z respectively, the x-component of the normal, n_x, for example, was computed as follows:

$$n_x = \frac{A_x}{\sqrt{A_x^{\,2} + A_y^{\,2} + A_z^{\,2}}} \tag{4.11}$$

c) Slope correction

The slope correction factor accounting for both longitudinal and transverse bed slopes, β and γ respectively, is given by:

$$\psi = \sqrt{\cos\beta\left(1-\frac{\tan\beta}{\tan\phi}\right)\cos\gamma\left(1-\frac{\tan^2\gamma}{\tan^2\phi}\right)}^{1/2} \tag{2.58}$$

For turbulent boundaries the slope correction was applied to the critical values of Mn and P_t as follows:

$$Mn_{c,\beta\gamma} = \psi Mn_{c,0} \tag{2.59}$$

$$P_{t,c,\beta\gamma} = \psi^3 P_{t,c,0} \tag{2.61}$$

The slope correction could not be implemented directly into Fluent in the *Custom Functions* panel as an error is returned if any of the custom functions becomes undefined. ψ was found to become undefined at several points on the channel bed where the magnitude of β exceeded the sediment angle of repose. For the bed adjustment simulations using the geometry of Ahmed (1995), the slope angles β and γ computed in Fluent were therefore exported into MS Excel for evaluation of ψ.

4.10 Manual bed adjustment according to the unit stream power model

Local scour at a pier studied by means of a physical model by Ahmed (1995) was modelled numerically using manual boundary adjustment to simulate the scour hole development. The flow field over a flat channel bed prior to scouring was computed and the applied stream power on the channel bed was assessed. Vertical movement of the cell nodes on the channel bed was calculated as a function of this applied stream power. The domain geometry was modified according to the calculated bed adjustments and the flow field computed again. This procedure was repeated for six adjustments.

4.10.1 Calculation procedure for bed adjustment

A scour potential Ω was calculated as the difference between the applied stream power P_t computed by the solver and assumed critical stream power $P_{t,c,\beta\gamma} = \psi^3 P_{t,c,0}$.

$$\Omega = P_t - \psi^3 P_{t,c,0} \tag{4.12}$$

The critical scour potentials at which scour and deposition would commence, Ω_{scour} and Ω_{depo} respectively, were then defined. Therefore

$$\text{if} \quad \Omega > \Omega_{scour} \quad \text{scour occurs} \tag{4.13}$$

$$\text{if} \quad \Omega < \Omega_{depo} \quad \text{deposition occurs} \tag{4.14}$$

The vertical adjustment Δy applied to each node at which scour or deposition occurs was then computed as a function of the difference between the applied and critical scour potentials. Relaxation factors C_{scour} and C_{depo} for scour and deposition respectively, were applied to translate the difference in scour potential into a vertical node movement and to limit the amount of movement of any node. The bed adjustment was therefore computed as follows:

$$\text{if} \quad \Omega > \Omega_{scour}$$
$$\text{then} \quad \Delta y = -C_{scour}\left(\Omega - \Omega_{scour}\right) \tag{4.15}$$

$$\text{if} \quad \Omega < \Omega_{depo}$$
$$\text{then} \quad \Delta y = +C_{depo}\left(\Omega - \Omega_{depo}\right) \tag{4.16}$$

The linear adjustments described by Equations 4.15 and 4.16 were applied in the first four bed adjustments. It was found that with further adjustment, the channel bed became undulating with sharp peaks and troughs. For the fifth and sixth bed adjustments, functions of the form $\Delta y \propto \sqrt{\Omega - \Omega_{scour}}$ were employed in an attempt to generate a smoother channel bed. The following functions were applied in these final two adjustments:

$$\begin{aligned} &\text{if} \quad \Omega > \Omega_{scour} \\ &\text{then} \quad \Delta y = -C_{scour}\sqrt{\Omega - \Omega_{scour}} \end{aligned} \tag{4.17}$$

$$\begin{aligned} &\text{if} \quad \Omega < \Omega_{depo} \\ &\text{then} \quad \Delta y = +C_{depo}\sqrt{\Omega - \Omega_{depo}} \end{aligned} \tag{4.18}$$

The manual bed adjustments to generate the scour hole of Ahmed (1995) were stopped after the sixth adjustment as the process is extremely tedious when undertaken manually and problems were encountered with the slope correction which became undefined at an increasing number of points after each adjustment. These problems are discussed in the findings of Chapter 5.

4.10.2 Selection of critical sediment transport parameters and relaxation factors

The initial flat bed simulation indicated a maximum applied stream power of 17 W/m^3 while the critical value for incipience, according to the criterion of Armitage (2002) given in Equation 2.55, was approximately 29 W/m^3. This suggested that no scour would take place at all. However, as the manual bed adjustment model is considered exploratory rather than intended to give definitive solutions for local scour depths, a lower critical stream power of $P_{t,c,0} = 5$ W/m^3 was adopted to allow a working model to be developed. The Rooseboom (1992) criterion (Equation 2.52) which yields $P_{t,c,0} \approx 10$ W/m^3 may have been more suitable but would still have generated a very small region of scour initiation.

The critical scour potentials for scour and deposition Ω_{scour} and Ω_{depo} respectively, were chosen such that the region in which scour took place was approximately equal in area to the region in which deposition took place downstream. The assumption is that the material removed from the scour hole is deposited in the wake of the pier as the local scour is occurring under clear-water conditions.

The relaxation factors for scour and deposition, C_{scour} and C_{depo}, were calibrated to ensure that the maximum movement at any node at each adjustment did not exceed 5 mm. Excessive adjustment could produce unrealistically steep scour holes and deposition mounds and create problems in the implementation of the slope correction.

The critical values $P_{t,c,0}$, Ω_{scour} and Ω_{depo} and relaxation factors C_{scour} and C_{depo} were revised every adjustment to achieve equality in the areas subject to scour and deposition and to limit the magnitude of bed adjustment as already discussed. Details are given in the Appendix. Obviously these values would need to be carefully chosen and calibrated prior to solution if an automated bed adjustment model were applied.

4.10.3 Slope correction and mitigation of slope correction problems

The slope correction required by Equation 4.12 was implemented as described in Section 4.9.3. Since the *wall function* model (Section 4.7.2) was applied for representation of the turbulent boundary layer at the channel bed, relatively large cells with vertical dimensions in the order of 3 mm were used adjacent to the channel bed. The velocity vectors in wall-adjacent cells were thus not very close to parallel to the channel bed as was assumed in the formulation for β used by McGahey (2001). It was therefore found that the slope correction factor ψ became undefined at a number of nodes on the channel bed, making the calculation of Δy impossible. The bed adjustments at such nodes were thus estimated by taking averages of the vertical co-ordinates of neighbouring nodes.

Further discussion of the limitations of the slope correction formula used and slope correction problems encountered is given in the Chapters that follow.

4.11 Conclusions

Incipient sediment motion and local scour at piers and abutments investigated in four small-scale models was modelled numerically in this study. The general commercial CFD code Fluent 6.2 was applied to solve the steady Navier-Stokes equations and the standard k-ε model was used for turbulent closure. The Volume of Fluid (VOF) multiphase model was used to track the free surface in open channel flow. The Movability Number and unit stream power models were used to estimate scour and deposition. Manual bed adjustment according to the unit stream power model was applied to simulate local scour hole development at the circular pier of Ahmed (1995). Vertical adjustment of nodes on the channel bed was computed as a function of the scour potential on the bed.

Chapter 5
Numerical Model Output and Discussion

The numerical model output is presented and discussed in this Chapter. Comparison is made with experimental measurements, other numerical models and sediment transport theory where applicable.

5.1 Free surface flow and incipient motion at piers and abutments

5.1.1 Circular pier (Midgely, 2000)

The computational domain employed for simulation of incipient motion at the pier of Midgely (2000) was illustrated in Figure 4.1 and details of the mesh around the pier in plan are shown in Figure 5.1 below. In the vertical direction, the mesh was refined at the bed to give $y^+ \approx 1$ for the application of a *near-wall* modelling approach in the turbulent boundary layer. The mesh was also refined vertically around the expected elevation of the air-water interface to give good resolution of the free surface.

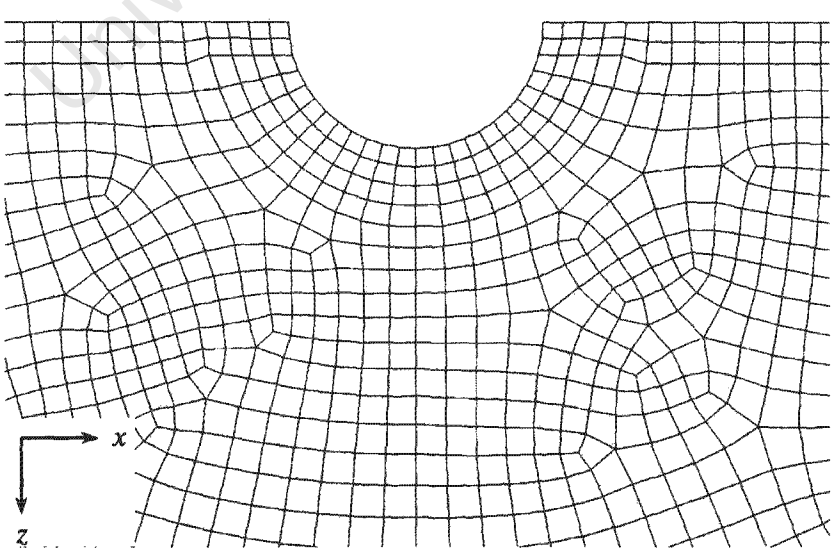

Figure 5.1: Plan view of mesh around the cylindrical pier

The VOF model computed the volume fraction of water in each cell in the domain. It was assumed that the free surface corresponded to the iso-surface where the water volume fraction was 0.5.

The free surface elevation is shown in Figure 5.2. The normal depth measured by Midgely (2000) and applied as boundary conditions at the inlet and outlet was 74.4 mm. A rise in the free surface associated with stagnation of the flow and formation of the bow wave at the upstream face of the pier is clearly evident as well as the drop at the side of the pier.

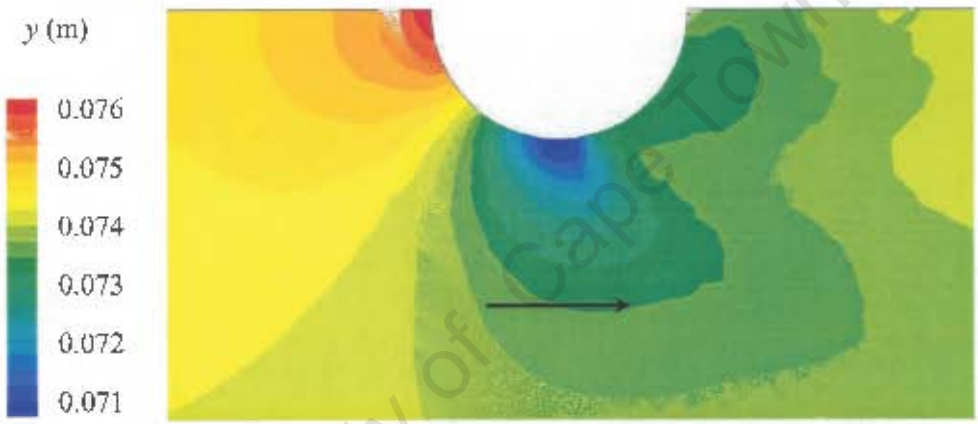

Figure 5.2: Elevation of the free surface around the circular pier

The velocity vectors in the horizontal *x-z* plane at the free surface and at the average sediment particle height are shown in Figures 5.3 and 5.4 respectively. Acceleration of the flow around the side of the pier at approximately 90° to the symmetry plane down the channel centreline is evident at both elevations.

The flow separation in the pier wake and formation of a recirculation zone are also shown.

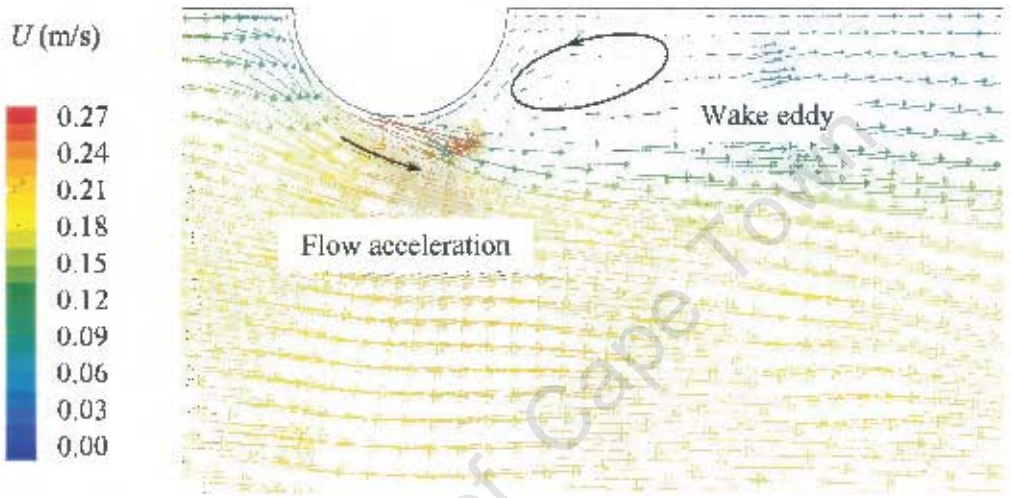

Figure 5.3: Velocity vectors at the free surface around the circular pier

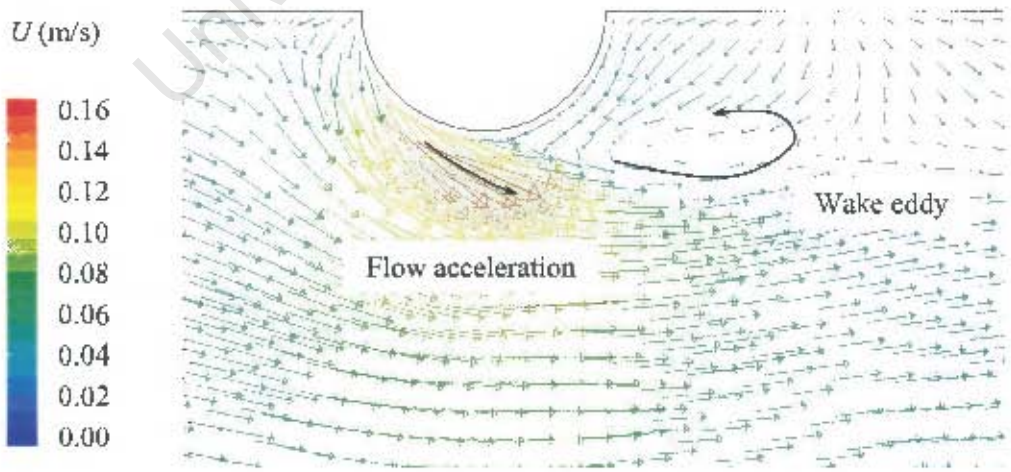

Figure 5.4: Velocity vectors at $y = k_s$ around a circular pier

The velocity vectors in the vertical *x-y* plane in Figures 5.5 and 5.6 clearly show downflow at the upstream face of the pier and the initial formation of the horseshoe vortex (Figure 5.6) even though there is no scour hole yet. Downflow at the pier side near the free surface is again evident in Figure 5.5 as was suggested by the free surface elevations in Figure 5.2.

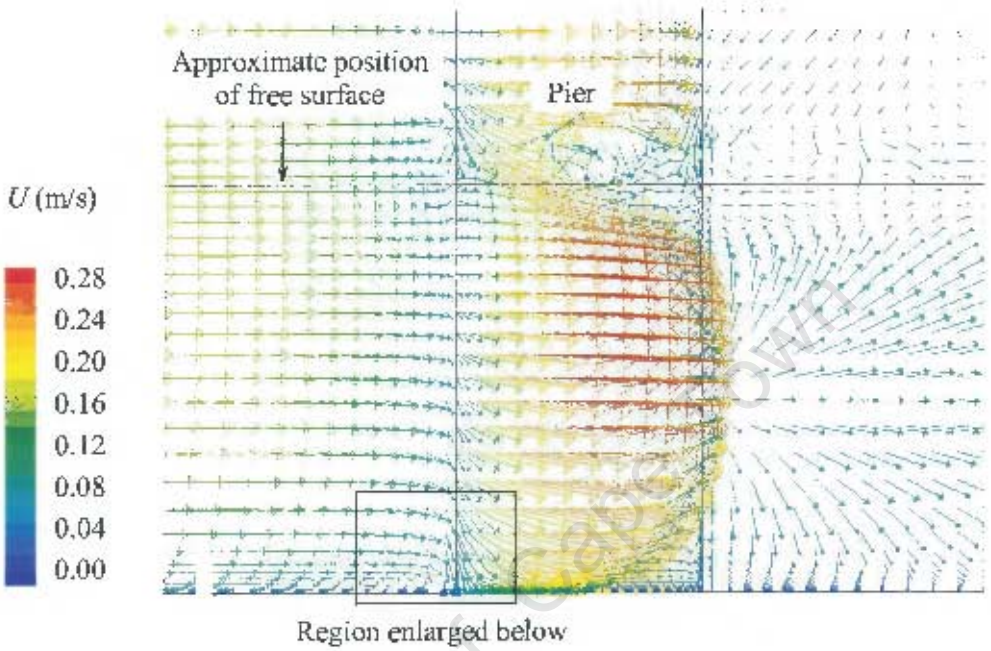

Figure 5.5: Velocity vectors on the symmetry plane and pier

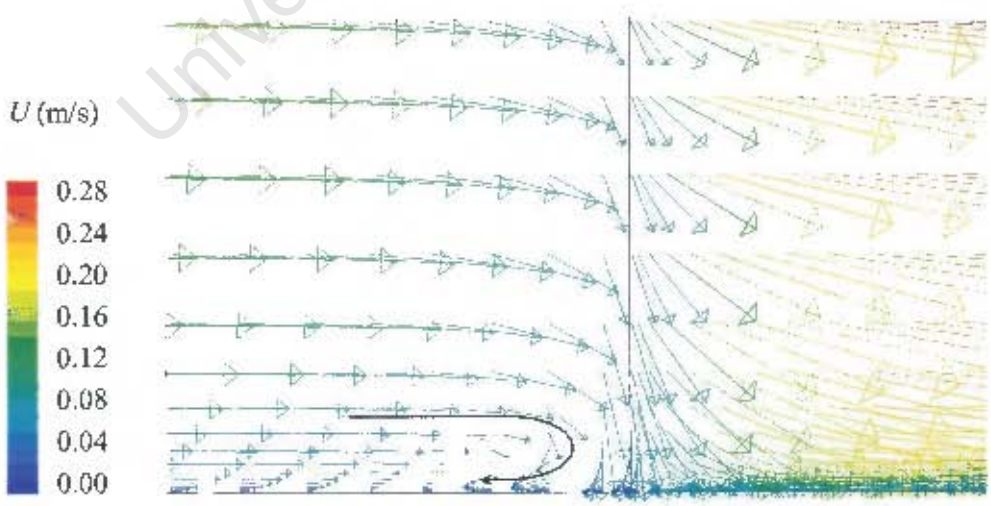

Figure 5.6: Downflow and beginning of horseshoe vortex at the pier base

The bow wave associated with a rise in the free surface at the upstream pier face is not shown by the velocity vectors in Figure 5.5. This is attributed to inadequate mesh refinement at the upstream pier face near the free surface. Some upward flow, which would be associated with formation of the bow wave is, however, evident at this point.

Figure 5.7 shows the variation of vertical velocity v with depth y at the pier nose. The negative values of v indicate downflow. According to Ettema (1980) and Raudkivi (1986), the maximum downflow velocity, v_{max}, occurs a distance $0.02d_p$ to $0.05d_p$ upstream of the pier face where d_p is the pier diameter. If there is no scour hole present, $v_{max} \approx 0.4U$ (Raudkivi, 1998).

The numerical model predicted a maximum downflow of $v_{max} = 0.048$ m/s $\approx 0.28U$ at a position 3.4mm $\approx 0.08d_p$ upstream of the pier face. The numerical model therefore underestimated the magnitude of the maximum downflow velocity.

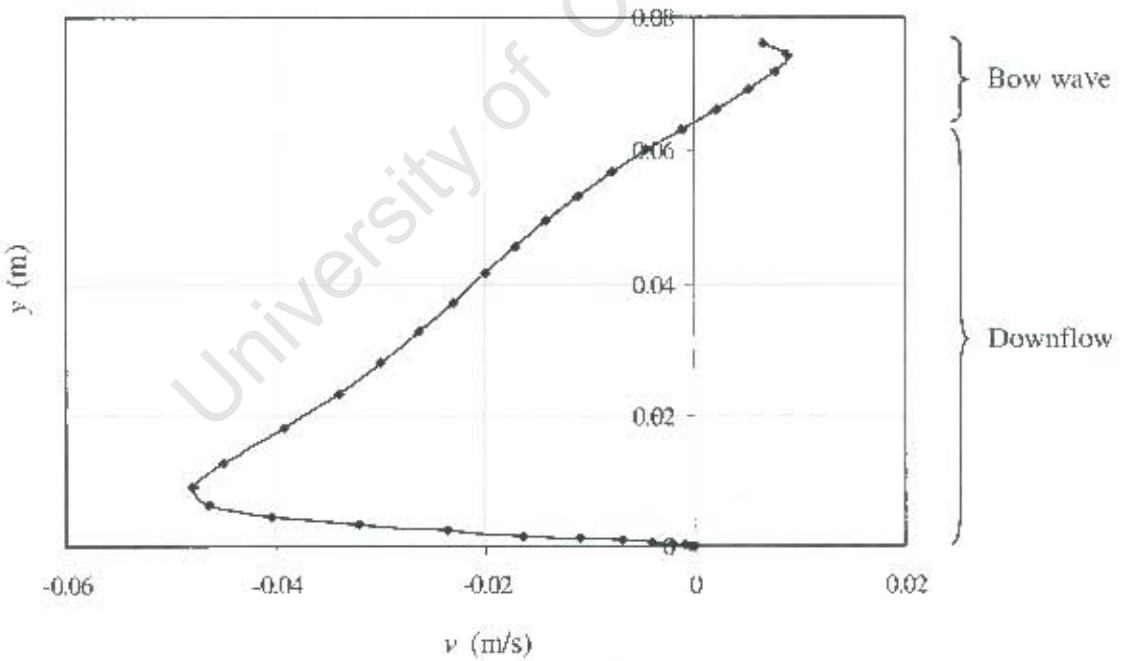

Figure 5.7: Downflow and bow wave at upstream face of the circular pier

Qualitatively, the flow patterns at the pier of Midgely (2000) predicted by the numerical model correspond well with the theory given in Section 2.10.1. Prominent flow features

such as stagnation and downflow at the upstream pier face, initial development of the horseshoe vortex, acceleration around the pier sides and formation of wake eddies are shown.

Incipient sediment motion at the pier is illustrated in the plots of Mn and P_t on the channel bed in Figures 5.8 and 5.9 respectively.

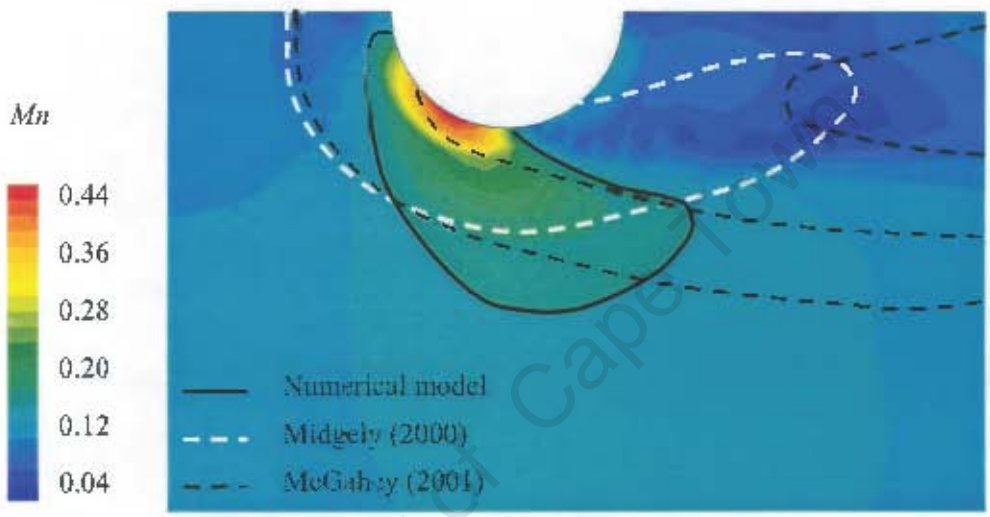

Figure 5.8: Movability Number distribution around pier at $y = k_s$ ($Mn_{c,0} = 0.17$)

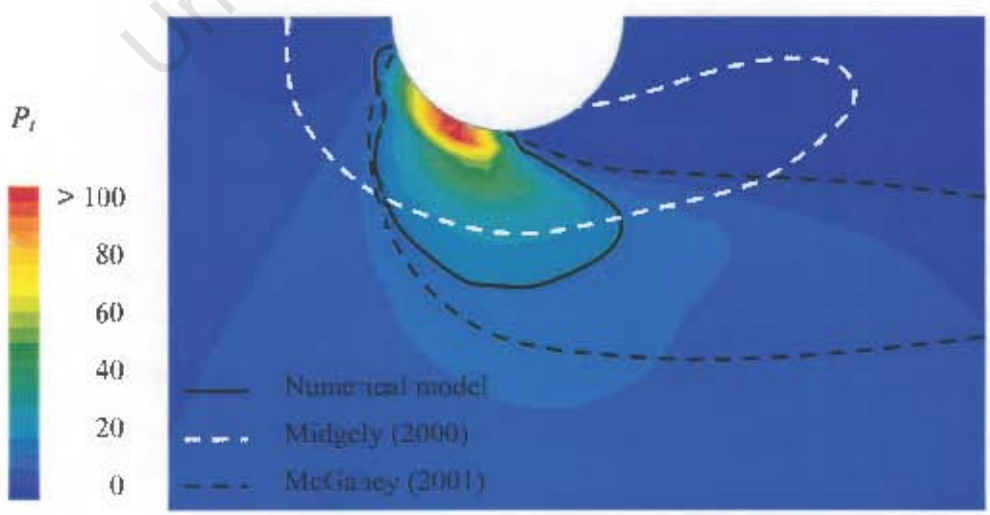

Figure 5.9: Applied stream power distribution around pier at $y = k_s$ ($P_{t,c,0} = 22$ W/m^3)

Critical values of $Mn_{c,0} = 0.17$ and $P_{t,c,0} = 22$ W/m^3 were computed for incipience (Sections 4.9.1 and 4.9.2 respectively) to delineate the regions which would be subjected to scour. The scoured region measured experimentally by Midgely and that predicted by the numerical model of McGahey (2001) are superimposed on the coloured contours of Mn and P_t computed by Fluent.

Both the plots of Mn and P_t computed by the numerical model indicate that scouring will commence at the foot of the pier at approximately 60 to 70 degrees to the symmetry plane. This is consistent with the theory of Breusers & Raudkivi (1991) and Raudkivi (1998) who suggest that scour is initiated at lateral scour holes which then extend in the upstream direction around the upstream pier face. Dargahi (1990) found that pier scour is initiated at two small lateral scour holes at approximately 45° to the pier centreline.

The scoured areas predicted by both the Movability Number and unit stream power models in this study are similar in shape and size. There are, however, some notable differences between this numerical model and the experimental measurements of Midgely (2000).

Midgely measured a scoured region concentric with the pier on the upstream side and extending downstream to form a horseshoe shape. Following the theory of Breusers & Raudkivi (1991), it is suggested that the scoured region measured by Midgely reflects a later stage of scour hole development than that shown by the numerical model since, in the physical model, there is already scour at the upstream face of the pier. A sand layer of only 1 mm to 2 mm in thickness was, however, used by Midgely in the physical model. It is therefore not possible that the horseshoe vortex was already well developed in the physical model.

The numerical model of McGahey (2001) predicted much larger scoured regions than those measured by Midgely and computed by the numerical model in the present study. The Movability Numbers computed by McGahey, however, agree very well with the physical model data upstream of the pier. It should be noted that McGahey assumed the same critical values for incipience used in this study; $Mn_{c,0} = 0.17$ and $P_{t,c,0} = 22$ W/m^3.

5.1.2 Rectangular abutment (Mitchell, 2000)

Flow and incipient motion at a rectangular abutment was simulated as described in Section 4.1.2. The mesh around the abutment in the horizontal x-z plane is shown in Figure 5.10. The mesh was refined near the channel walls and around the abutment. In the vertical direction, the mesh was generated to give $y^+ \approx 1$ at the bed and refined around the expected elevation of the air-water interface to give good resolution of the free surface. Due to the rectangular geometry of the domain and abutment, a structured, hexahedral mesh was used for simulation of flow around this obstacle.

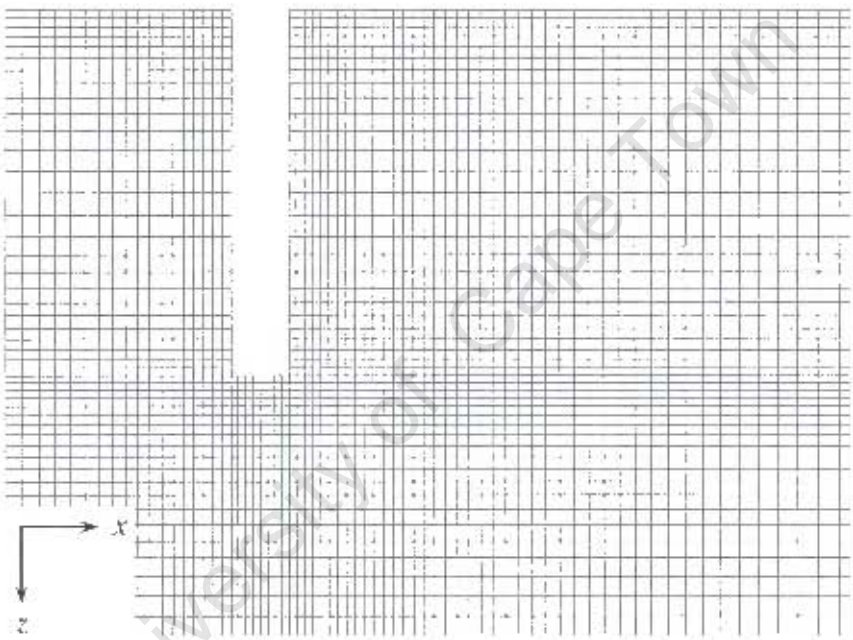

Figure 5.10: Plan view of the mesh at the rectangular abutment

The free surface elevations near the abutment are shown in Figure 5.11. A rise in the free surface occurs in the stagnating dead water zone on the upstream side (Section 2.10.2). There is a sudden drop in the water level at the abutment tip as the flow accelerates around the end of the obstacle. These flow features are analogous to the bow wave and acceleration of flow around the side of the pier discussed in the previous section. A long zone of recirculation and large, slowly-rotating eddy forms in the wake of the abutment (Figure 5.12). The minimum water level, indicated by the dark blue region in Figure 5.11, corresponds with the centre of this large eddy.

Figure 5.12 gives an overall view of velocity vectors on the free surface around the rectangular abutment. Details of particular flow features on the free surface in the horizontal plane are shown in Figure 5.13. The velocity vectors at the average sediment particle height, $y = k_s$ are shown in Figure 5.14. In all cases the mean flow direction is from left to right.

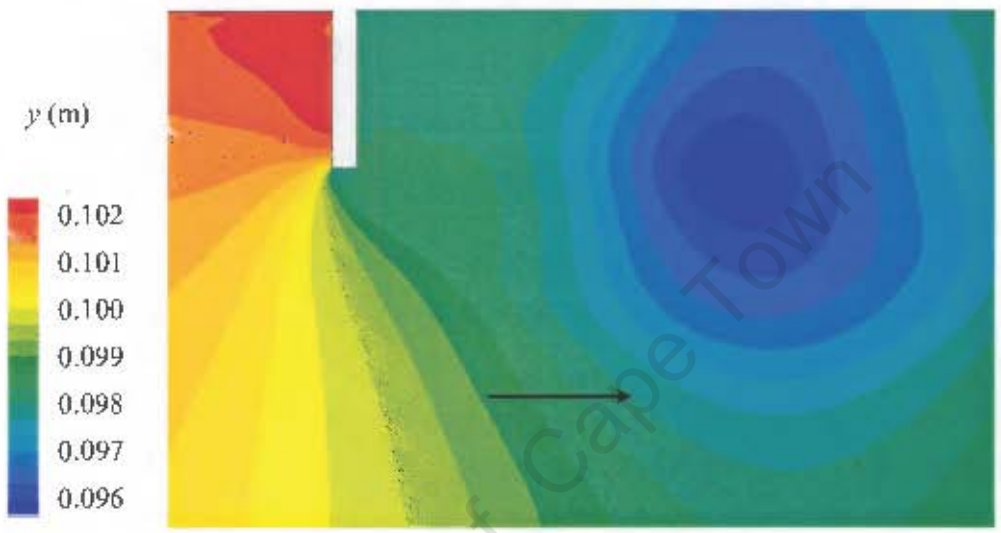

Figure 5.11: Elevation of the free surface at the rectangular abutment

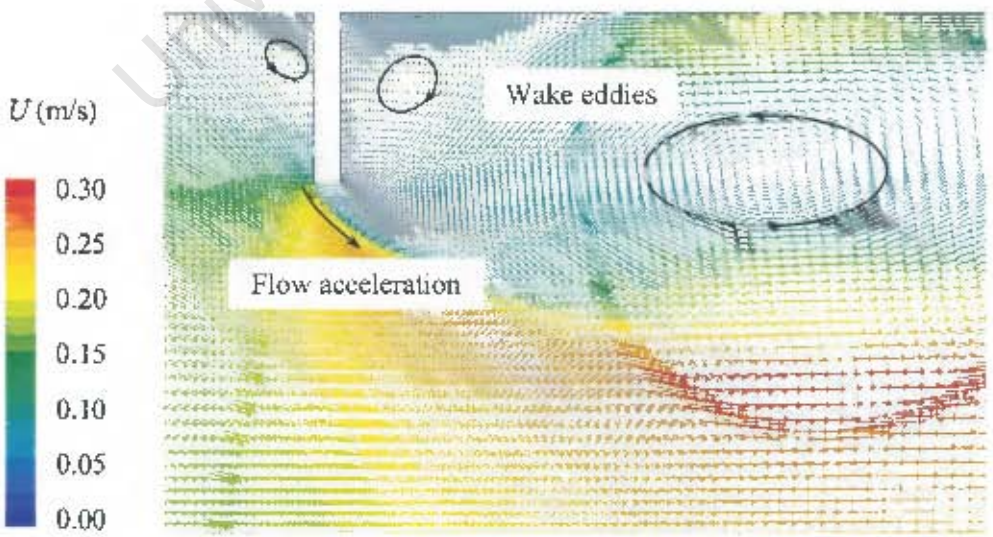

Figure 5.12: Velocity vectors at the free surface around the rectangular abutment

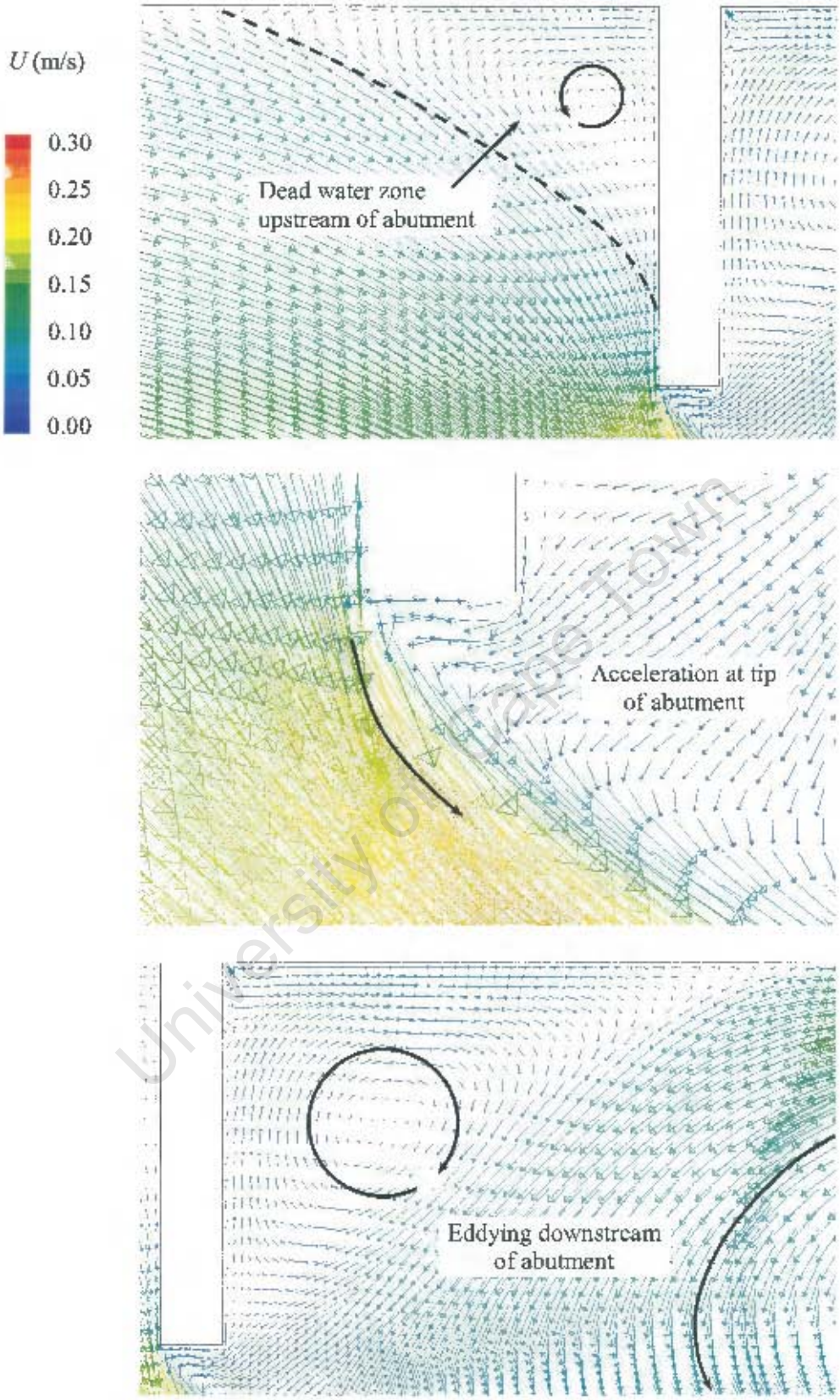

Figure 5.13: Details of velocity vectors on the free surface around rectangular abutment

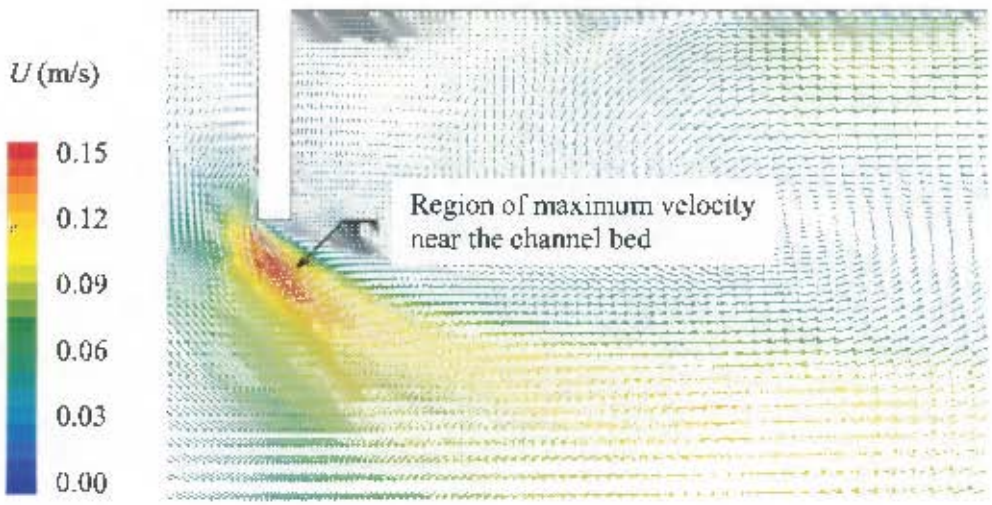

Figure 5.14: Velocity vectors at $y = k_s$ at the rectangular abutment

The velocity vectors on the free surface (Figure 5.12) and near the channel bed (Figure 5.14) show similar flow features such as the eddies downstream of the abutment. The maximum velocities, however, occur in different regions. At the free surface the maximum velocity, indicated by the red vectors, is evident some distance downstream of the abutment in the main flow region and is a consequence of the flow constriction caused by the protruding obstacle. At the channel bed, however, the maximum velocity occurs near the tip of the abutment.

Incipient motion predicted according to the Movability Number and unit stream power models is shown in Figures 5.15 and 5.16. Critical values of $Mn_{c,0} = 0.17$ and $P_{t,c,0} = 22$ W/m^3 were again assumed for incipience (Section 4.9). Solid black lines delineate the scoured regions predicted by the numerical model. For comparison, the experimental measurements of Mitchell (2000) and numerical model predictions computed by McGahey (2001) are superimposed on the coloured contours generated by Fluent.

The maximum values of Mn and P_t predicted by the numerical model both occur at the tip of the abutment indicating that scour will commence here. The extents of the predicted scoured regions are overestimated although the shapes appear realistic. It is suggested that the constricting effects of the abutment on the flow are exaggerated by the numerical

model. The lateral (z-direction) extent of the zone of recirculation in the abutment wake is overestimated reducing the effective flow width and exaggerating the effects of constriction. Selection of higher thresholds for particle motion such as $Mn_{c,0} \approx 0.25$ and $P_{t,c,0} \approx 40$ W/m^3, for example, would yield better agreement with the experimental data of Mitchell (2000).

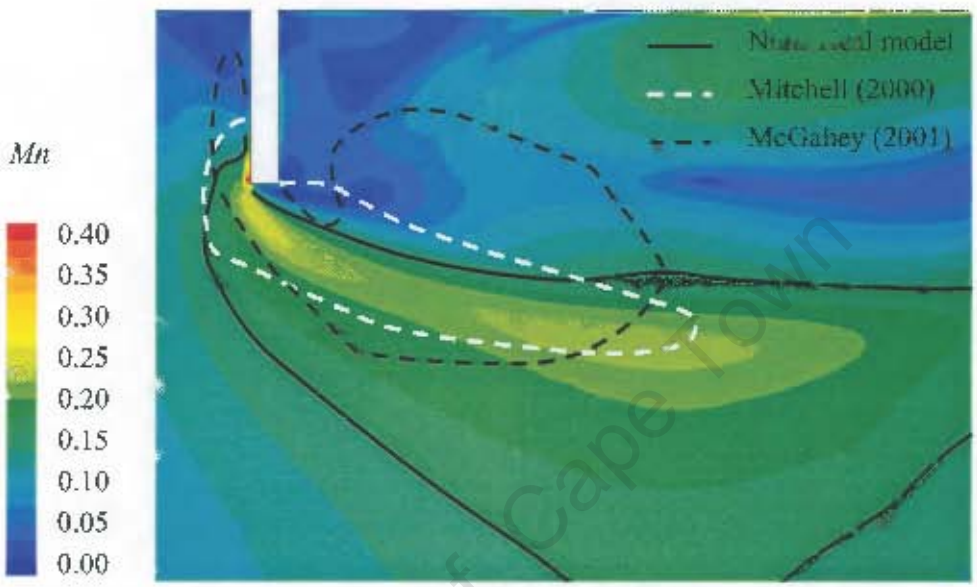

Figure 5.15: Movability Numbers around the rectangular abutment at $y = k_s$ ($Mn_{c,0} = 0.17$)

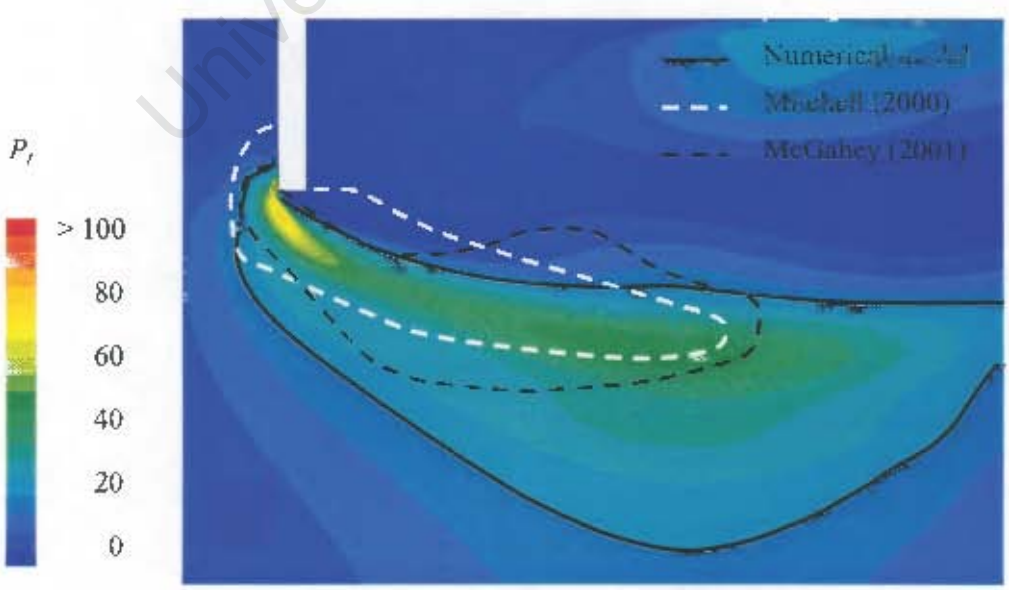

Figure 5.16: Stream power around the rectangular abutment at $y = k_s$ ($P_{t,c,0} = 22$ W/m^3)

5.2 Flow and scour in a developed scour hole

Flow through the developing, non-equilibrium clear-water scour hole at a semi-circular abutment measured by Unger & Hager (2005) was simulated and the values of Mn and P_t on the channel bed and in the scour hole were computed. The model was described in Section 4.1.3 and the scour hole bathymetry was illustrated in Figure 4.4.

The flow features at the semi-circular abutment were compared to those typically found at a circular pier due to the geometric similarity and availability of data for flow patterns at circular piers. At the upstream face of the semi-circular abutment, a maximum downflow velocity of $v_{max} = 0.32$ m/s $\approx 0.83U$ was found at a distance of 20 mm $\approx 0.08d_p$ upstream of the abutment face and at a distance of 164 mm $\approx 0.63d_p$ below the initial bed level. According to Raudkivi (1998), when $y_s > 2d_p$ at the pier face, a maximum downflow of $v_{max} \approx 0.8U$ occurs approximately one pier diameter below the bed of the approach flow.

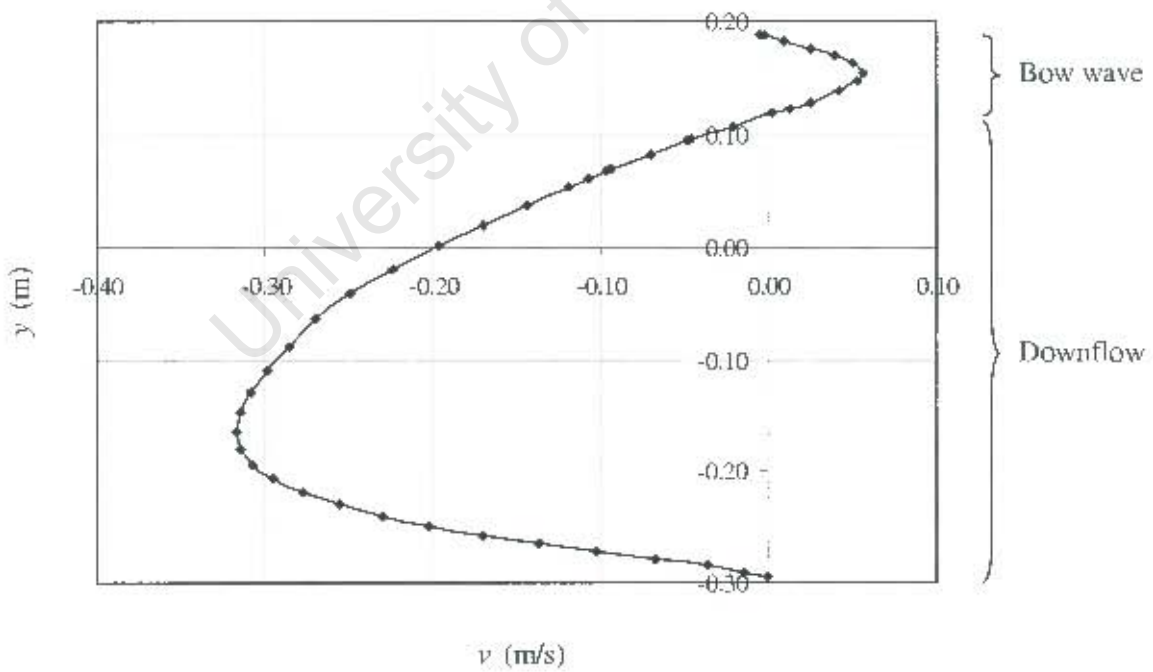

Figure 5.17: Downflow and bow wave at the upstream face of the semi-circular abutment

The maximum downflow predicted by the numerical model agrees very well with the theoretical value of $v_{max} \approx 0.8U$. The location of v_{max}, however, differs from published values. It must be noted that, firstly, the scour hole modelled numerically had not reached its maximum equilibrium depth and, secondly, that the influence of the channel wall at the abutment will cause flow patterns at the semi-circular abutment to differ from those typically found at a circular pier.

A plot of the computed downflow against depth is shown in Figure 5.17. The initial bed level prior to scour is at $y = 0$. It can be seen that the maximum downflow occurs roughly at the mid-depth of the scour hole. Upward flow associated with formation of a bow wave is evident near the free surface at $y = 186$ mm.

The flow through the scour hole measured by Unger & Hager (2005) is shown in Figures 5.18 and 5.19. Vector plots along the channel wall and on the abutment surface (Section A-A) and on vertical planes at 45 degrees (Section B-B) and 90 degrees (Section C-C) to the channel wall show various pertinent flow features associated with local scouring at an abutment. In Sections B-B and C-C the mean flow direction is out of the page.

A bow wave can be seen near the free surface on the channel wall in Section A-A. Development of the horseshoe vortex in the scour hole is clearly evident in all three cross sections in Figure 5.19. Downflow adjacent to the abutment impinges on the channel bed to aid the local scouring process. As expected, cross-sections taken further downstream of those shown in Figure 5.19 did not exhibit the horseshoe vortex clearly.

The paths that would be followed by imaginary fluid "particles" travelling through the scour hole are shown in Figure 5.20. The helical or spiralling path that such particles would follow around the abutment side confirms the development of the horseshoe vortex. Sediment particles would be transported out of the scour hole by the helical flow during the scouring process. The particles shown in the figure were "released" at the upstream edge of the scour hole a distance 2 mm above the channel bed.

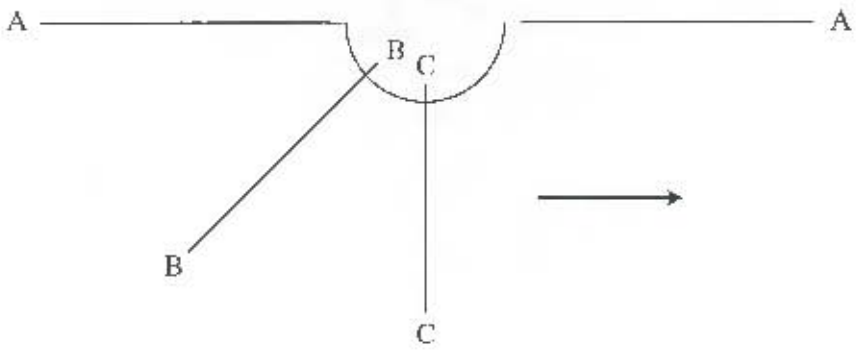

Figure 5.18: Sections for vector plots showing horseshoe vortex at semi-circular abutment

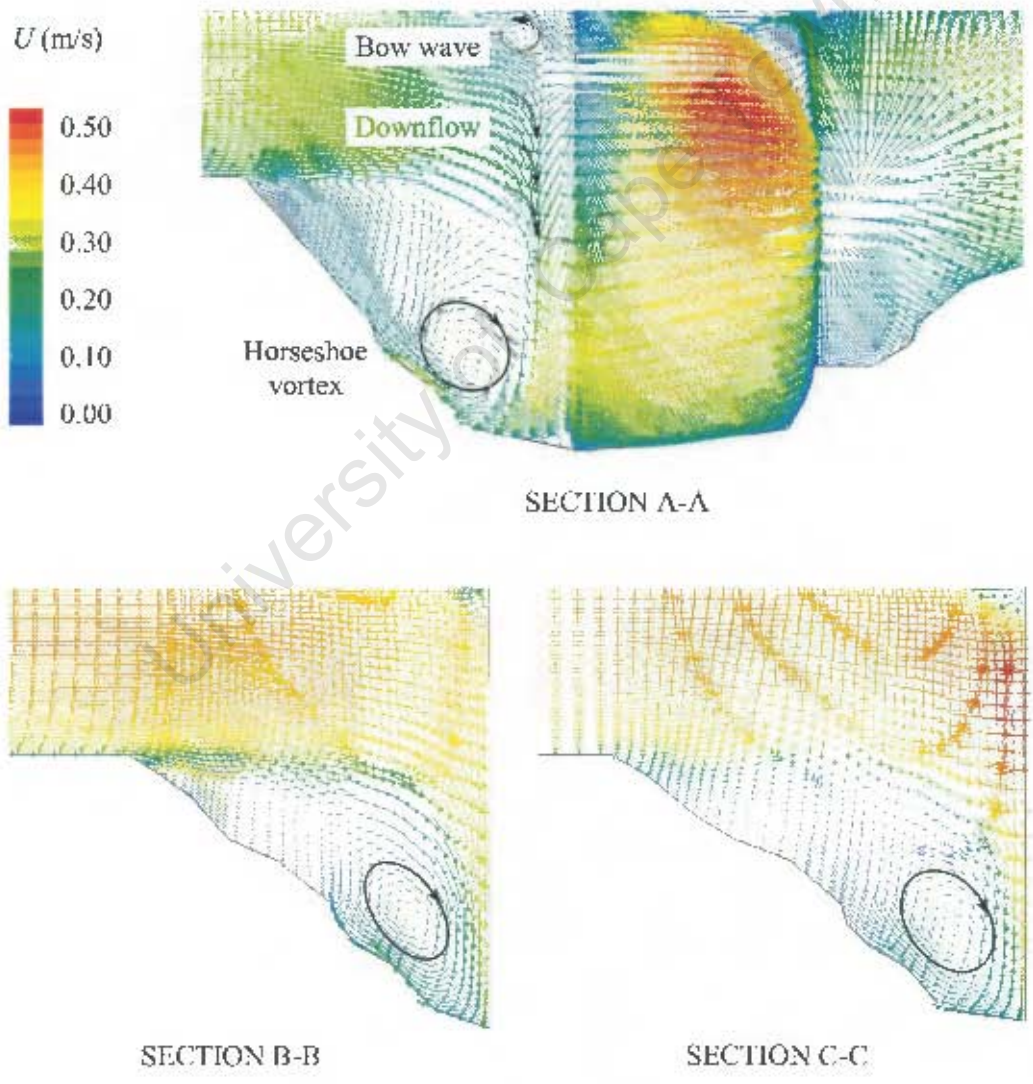

Figure 5.19: Vectors illustrating the development of the horseshoe vortex at the semi-circular abutment

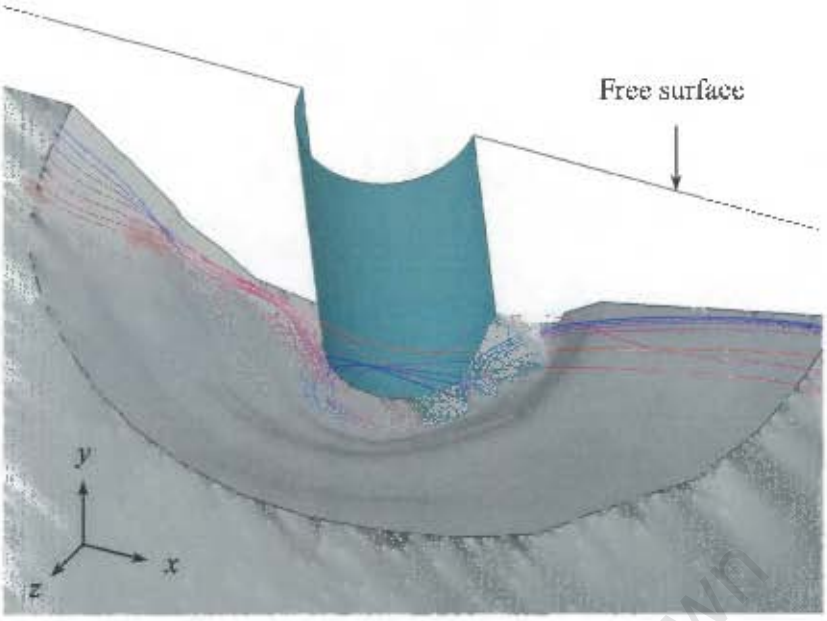

Figure 5.20: Pathlines of "fluid particles" released from upstream edge of scour hole

Patterns of scour and deposition computed according to Mn and P_t are shown in Figures 5.21 and 5.22 respectively. Contour lines indicating the scour hole bathymetry are superimposed on the coloured contour plots of Mn and P_t. It must be noted that comparisons between the computed and critical values of Mn and P_t are only meaningful on the flat region of the channel bed and in the deepest parts of the scour hole where $\psi \approx 1$. It should also be remembered that much of the scour hole bathymetry was generated from extrapolated rather than measured depth contours (Section 4.1.3).

The Movability Numbers on the flat bed surrounding the scour hole are in the region of $Mn = 0.16$ to $Mn = 0.20$. This suggests that threshold conditions have already been reached on the channel bed upstream of the scour hole since $Mn_{c,0} = 0.17$. In the deepest part of the scour hole, $Mn \approx 0.20 > Mn_{c,0}$ which indicates that equilibrium has not yet been reached and further scouring will take place. The critical applied stream power for the sediment of Unger & Hager (2005) is $P_{t,c,0} = 33$ W/m^3 (Section 4.9.2). It is clear that the numerical model underestimates P_t since, at the deepest point of the scour hole, $P_t \approx 3$ W/m^3 $\ll P_{t,c,0}$ suggesting that scouring has taken place beyond an equilibrium state as the applied stream power is much lower than the critical value for incipience. The

stream power model thus contradicts the Movability Number model in this instance. For convenience, P_t in this deformed bed simulation was computed on the channel bed rather than at the average sediment particle height. This is a possible source of error as P_t is very sensitive to the depth at which it is computed near the bed.

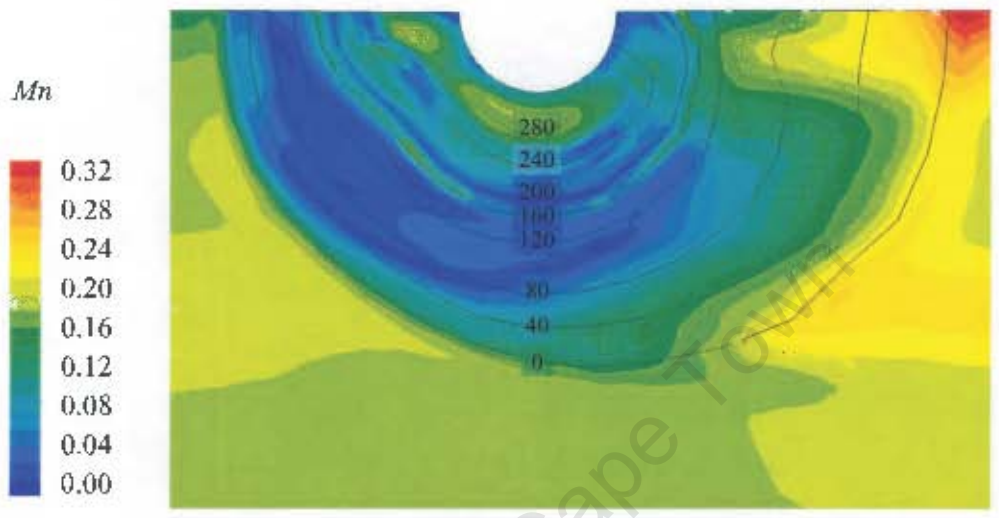

Figure 5.21: Movability Number distribution in the scour hole at a semi-circular abutment ($Mn_{c,0}$ = 0.17; Superimposed contour lines indicate scour hole depth in millimetres)

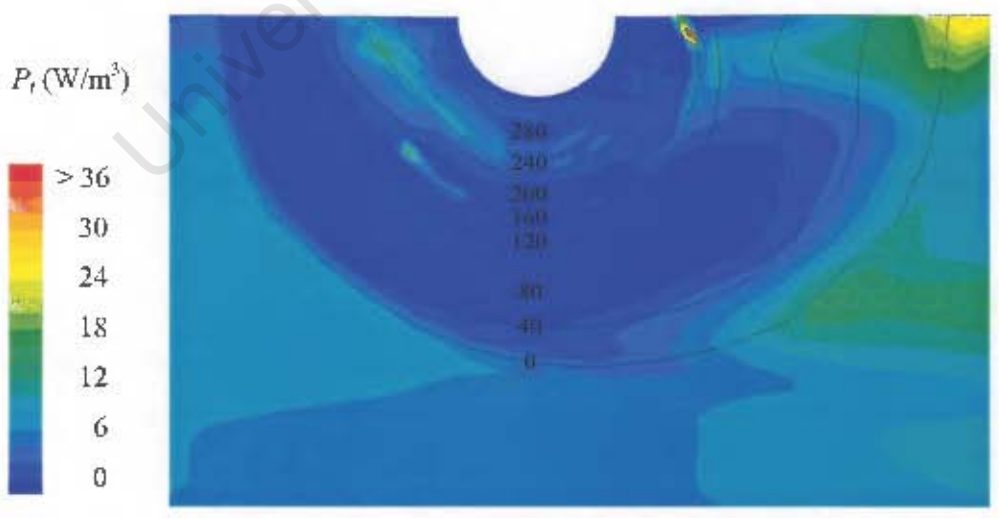

Figure 5.22: Stream power distribution in the scour hole at a semi-circular abutment ($P_{t,c,0}$ = 33 W/m^3; Superimposed contour lines indicate scour hole depth in millimetres)

5.3 Scour hole development by manual bed adjustment

Figures 5.23 and 5.24 show the computational mesh used for simulation of flow around the circular pier studied by means of a physical model by Ahmed (1995). A radial mesh structure was used in the horizontal plane for the convenience of calculating node co-ordinates in the bed adjustment process. The cell height at the bed was chosen to give $y^+ \approx 30$ for application of the *wall function* approach in the turbulent boundary layer.

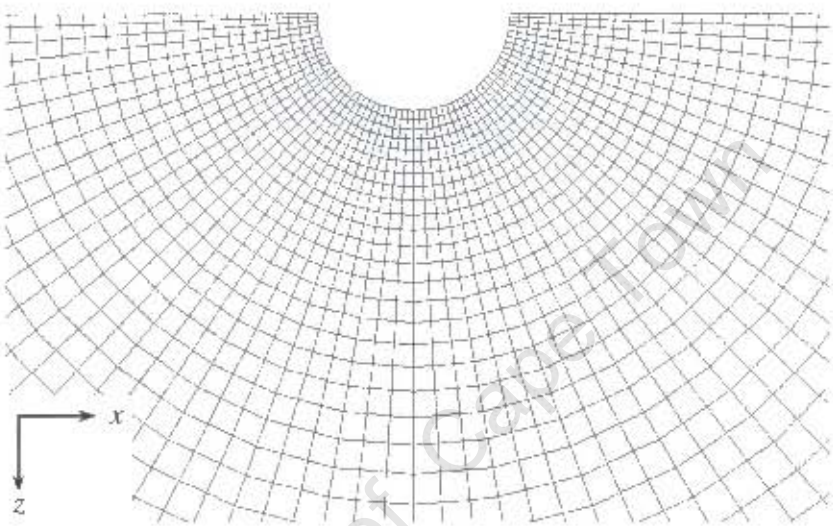

Figure 5.23: Plan view of mesh at the pier for manual bed adjustment simulations

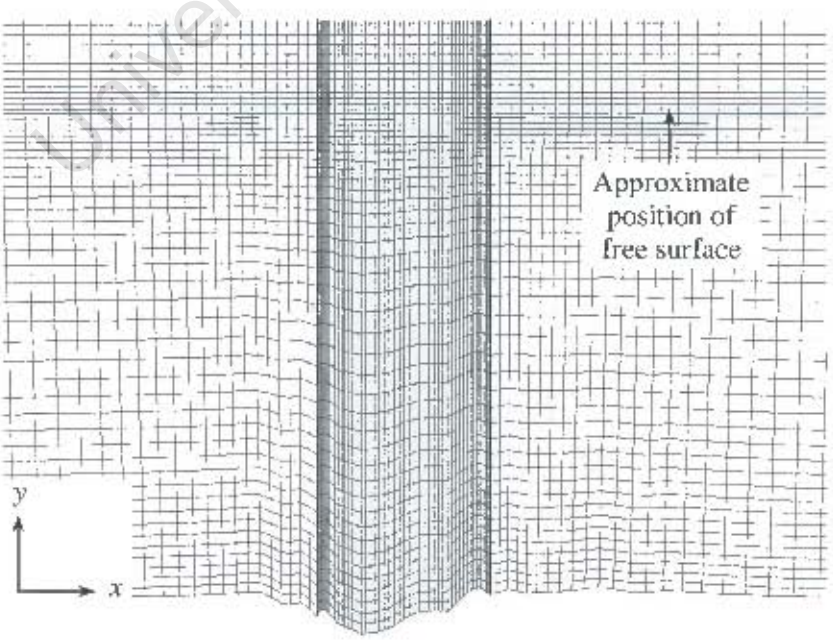

Figure 5.24: Typical mesh around the pier in the x-y plane

The experimental setup used by Ahmed (1995) was described in Section 4.1.4. Manual bed adjustment was performed according to the unit stream power approach as detailed in Section 4.10.

The initial distribution of P_t on the channel bed is shown in Figure 5.25 below. The critical stream power for incipience on a flat channel bed was $P_{t,c,0} = 29$ W/m^3. The maximum stream power on the bed computed by the numerical model was 17 W/m^3 which suggested that threshold conditions required for sediment movement had not been attained. To facilitate development of the bed adjustment model, a critical stream power of $P_{t,c,0} = 5$ W/m^3 was simply assumed for the calculation of the first bed adjustment.

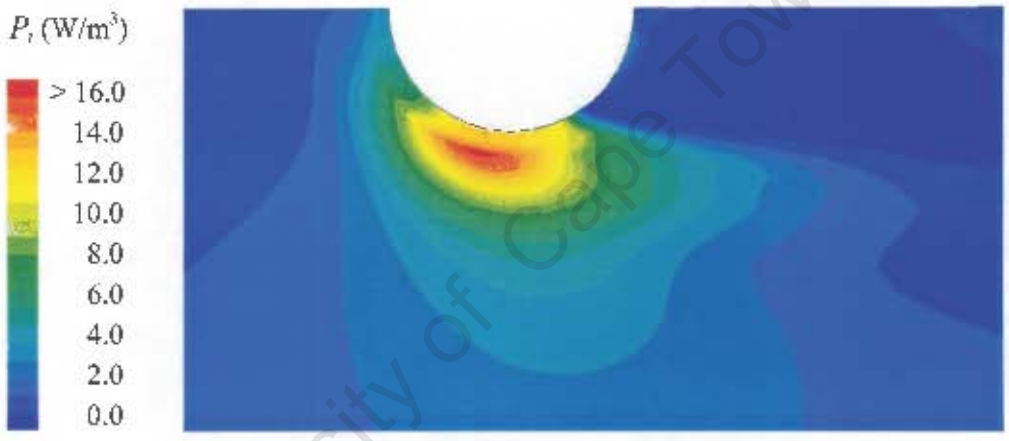

Figure 5.25: Initial distribution of applied stream power on the undeformed channel bed

The scour hole bathymetry computed in the each of the six adjustments is shown in Figures 5.26 a - f. Coloured plots of P_t are superimposed on the scour hole bathymetry and use the same colour scale as that for the initial unscoured bed in Figure 5.25. The maximum scour and deposition depths in millimetres are also given for each adjustment. Negative depth values indicate scour and positive values indicate deposition.

Initial development of the scour hole took place adjacent to the pier at approximately 70 to 80 degrees to the symmetry plane used to represent the channel centreline. Migration of this lateral scour hole upstream with development of the local scour is shown in the figures. The maximum scour depth, however, remained at the side of the pier.

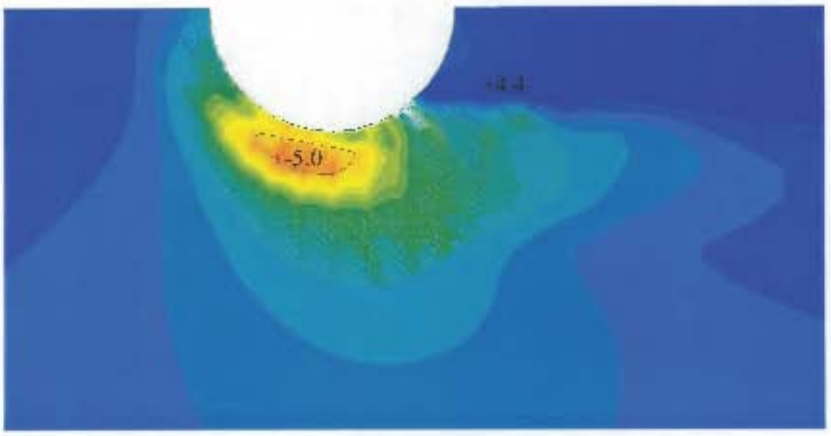

a) Adjustment 1

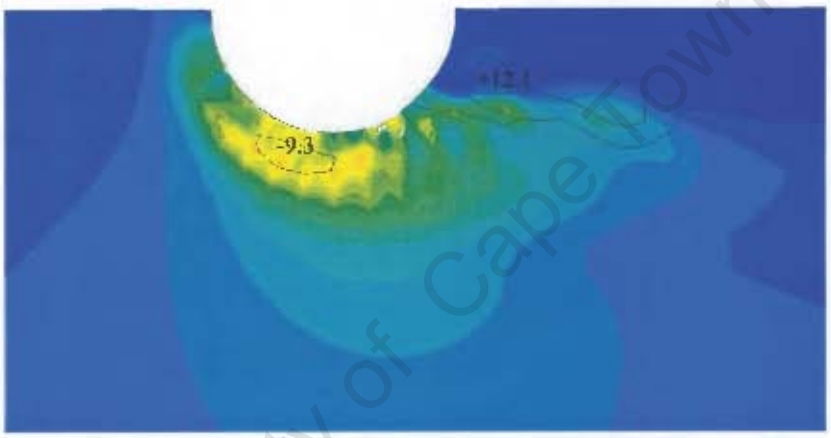

b) Adjustment 2

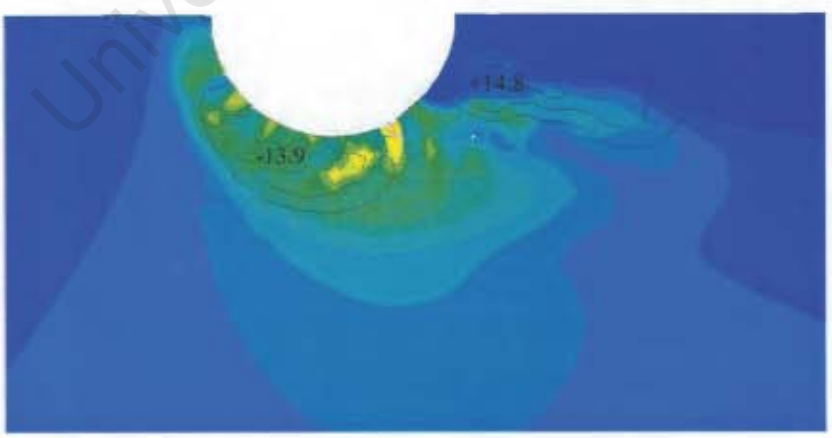

c) Adjustment 3

Figure 5.26: Distribution of applied stream power at the channel bed
(Contour lines indicate bed elevation in millimetres, contour interval = 4 mm)

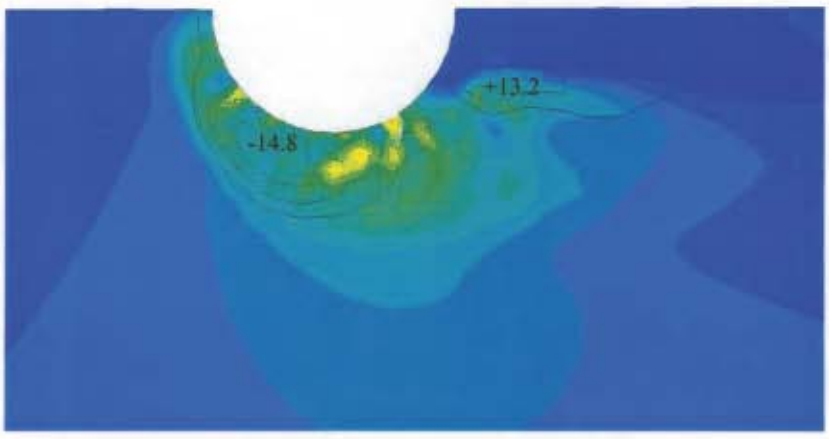

d) Adjustment 4

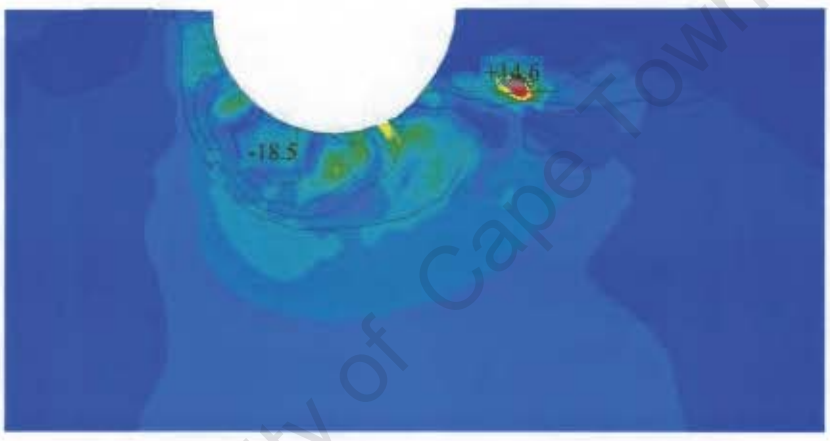

e) Adjustment 5

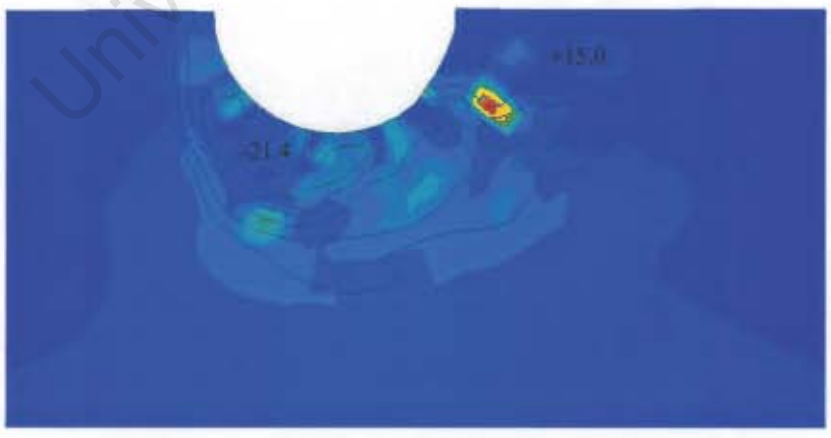

f) Adjustment 6

Figure 5.26 (continued): Distribution of applied stream power at the channel bed (Contour lines indicate bed elevation in millimetres, contour interval = 4 mm)

The flow patterns around the pier after the 4th adjustment are shown in Figures 5.27 and 5.28. The beginning of a horseshoe vortex is evident. The mesh near the bed is, however, too coarse to show this clearly. It was not possible to use a finer mesh near the bed as the cells would have had undesirably large aspect ratios and become highly skewed with increasing bed deformation.

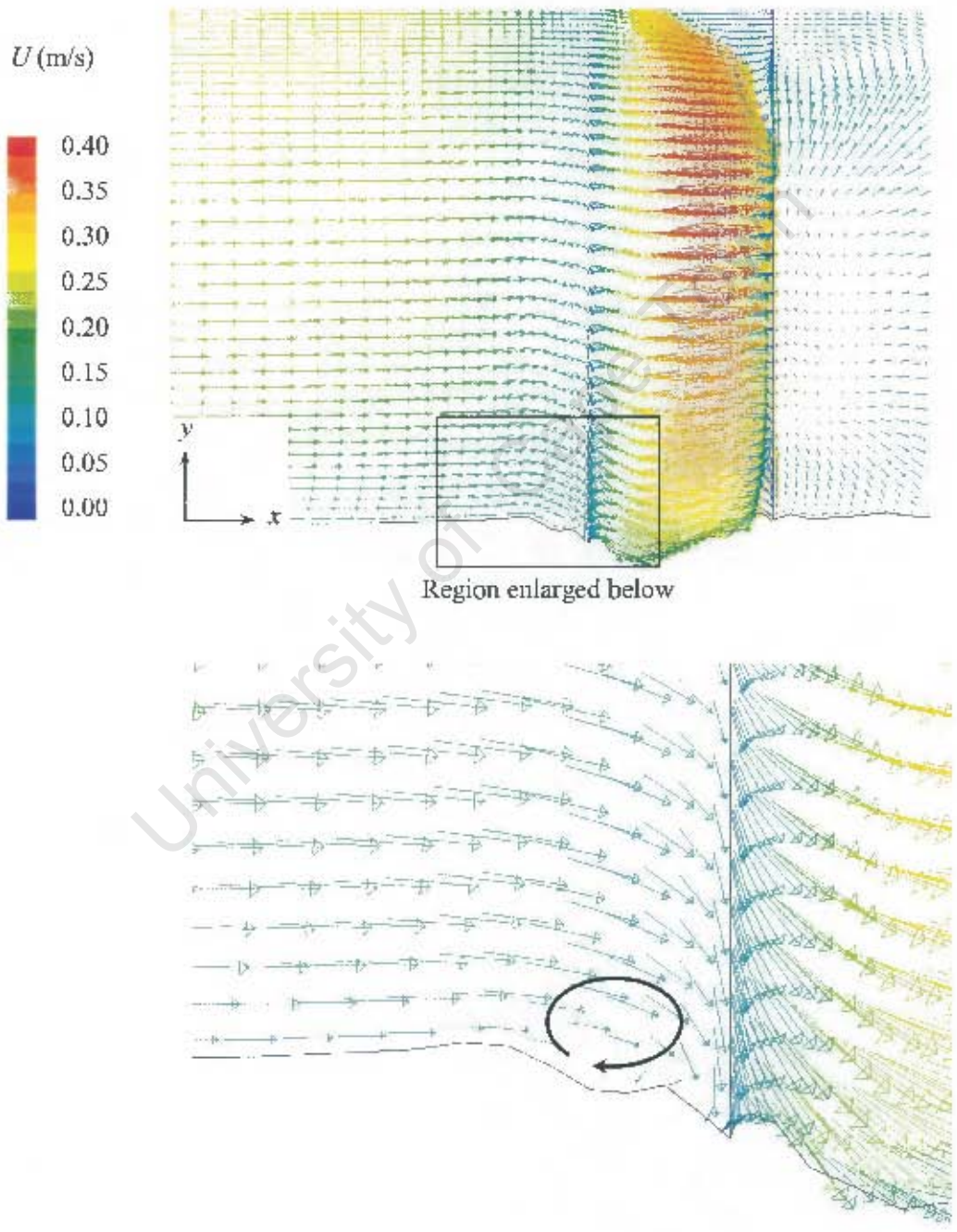

Figure 5.27: Vectors on the symmetry plane and pier at Adjustment 4

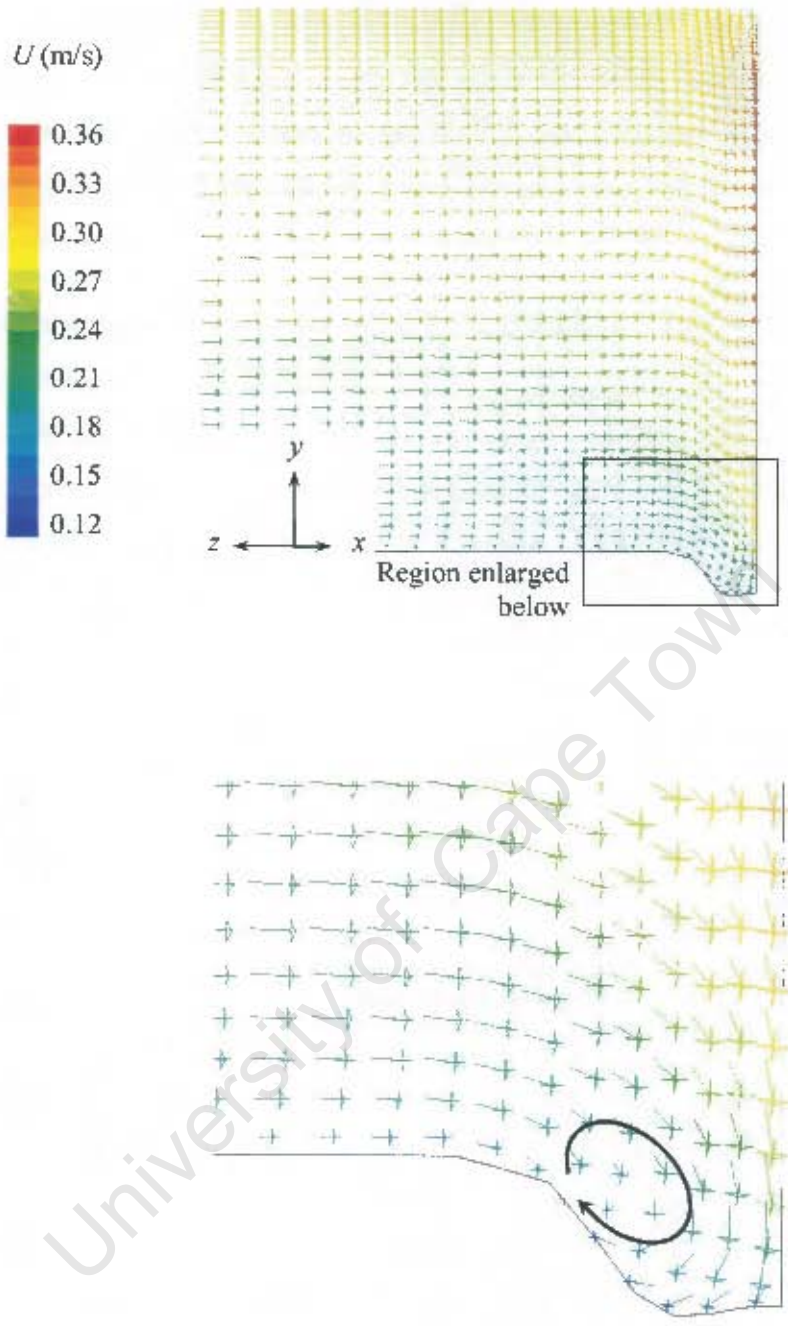

Figure 5.28: Vectors on a plane at 60 degrees to the symmetry plane at Adjustment 4

The maximum downflow at the pier increased steadily from $v_{max} = 0.34U$ prior to bed deformation to $v_{max} = 0.42U$ after the 6th adjustment. These values correspond well with the theoretical value $v_{max} \approx 0.4U$ suggested by Raudkivi (1998) for a flat channel bed.

The bed adjustment model was stopped after six adjustments as the manual process became very tedious and because the slope correction factor became undefined at an increasing number of nodes with continuing bed deformation as the bed slopes exceeded the sediment angle of repose. At the first adjustment ψ was undefined at 3 nodes but by the 6th adjustment, ψ could not be computed and therefore had to be estimated at 40 nodes.

The computed values of β and γ on the bed at the 4th adjustment are shown in Figures 5.29 and 5.30. Contours indicating the scour hole bathymetry in millimetres are superimposed. The sediment angle of repose was approximately 35° (Ahmed, 1995).

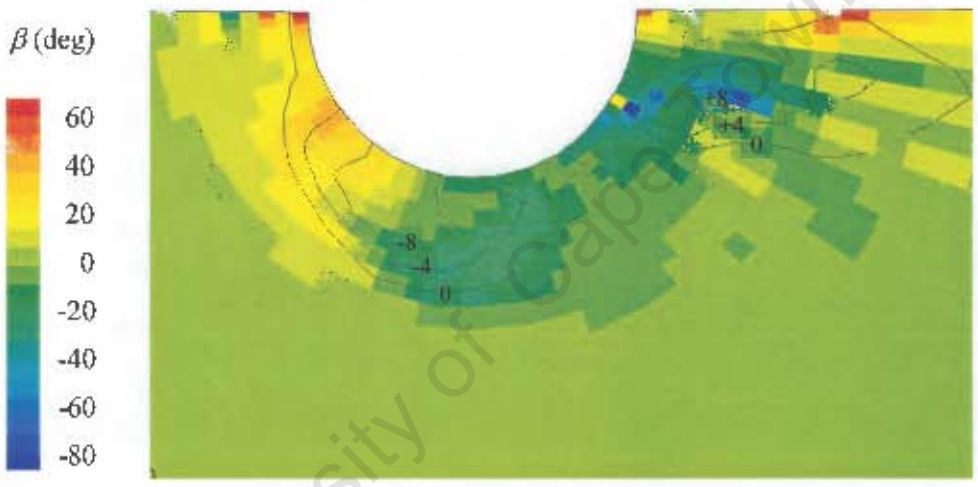

Figure 5.29: Distribution of streamwise bed slope angle β for Adjustment 4 ($\phi = 35°$)

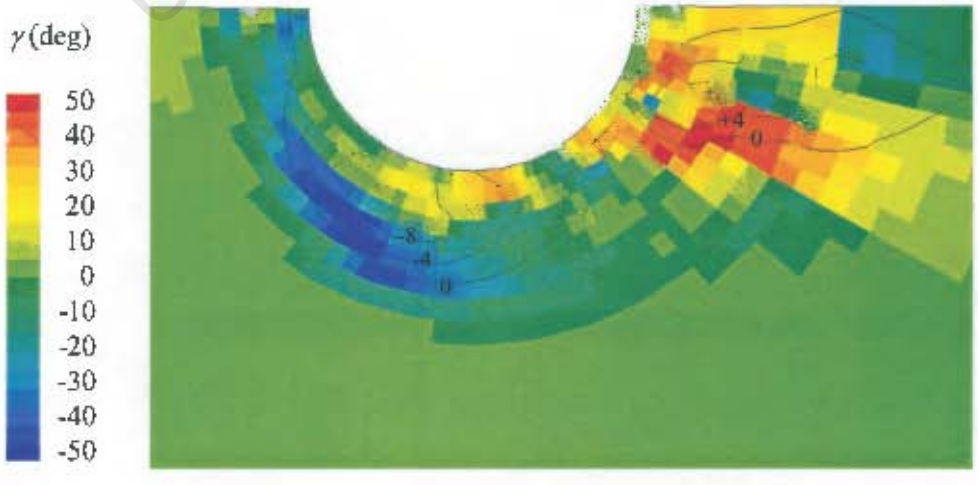

Figure 5.30: Distribution of transverse bed slope angle γ for Adjustment 4 ($\phi = 35°$)

Possible remedies for the slope correction problems include:

- Use of smaller bed adjustments in the order of 1 to 3 mm for example. This would, however, have to be implemented in an automated bed deformation model as many adjustments would be required to deform the bed until an equilibrium state is reached.

- Vertical mesh refinement to ensure velocity vectors are in fact parallel to the channel bed as assumed in the slope correction formulation. The problem with vertical mesh refinement is that the mesh must be refined by a similar amount in the horizontal plane to prevent generation of skewed cells with very high aspect ratios.

- Development of an alternative slope correction formula or modification of the existing formula so that it is defined for all possible values of β and γ.

The manual bed adjustment simulations were carried out on meshes containing approximately 400 000 cells. Each simulation took about 4 hours to converge. A further 3 hours was then required per adjustment to export numerical model output to MS Excel spreadsheets, perform the bed adjustment calculations, make manual adjustments to any nodes at which ψ was undefined and recreate the domain geometry and mesh.

It is clear that manual bed adjustment is too tedious for application to local scour problems in practice. Automated procedures are required. The adjustment technique used is, however, useful for simulating scour hole development given the current computational constraints which would not allow simulation of time-accurate scour hole development. Clear-water local scour holes can take several days to reach equilibrium. The scour hole modelled experimentally by Ahmed (1995) took 220 hours to reach an equilibrium depth. A maximum scour depth of 54 mm was reached upstream of the pier.

5.4 Conclusions

The numerical model produced realistic predictions of flow features at the variety of piers and abutments simulated. Incipient motion predictions according to the Movability

Number and unit stream power approaches in the physical models of Midgely (2000) and Mitchell (2000) were fair. The stream power model tends to underestimate the applied power on the channel bed and is very sensitive to the depth at which the power dissipation is computed.

Flow features which are important in the formation and development of local scour holes were clearly evident at the semi-circular abutment of Unger & Hager (2005). Downflow at the abutment tip and formation of the horseshoe vortex and its associated helical flow patterns were clearly shown in the numerical model.

The manual bed adjustment model investigated for simulating temporal development of local scour holes shows promise for future use. The bed adjustment process needs to be automated and alternative slope correction formulations must be developed.

Chapter 6
Conclusions

A numerical model for the prediction of local scour based on the Movability Number and unit stream power models for sediment transport was investigated using a general CFD code. Numerical model predictions of the free surface variations and flow patterns around various piers and abutments showed promise for use of the model in simulating local scour and deposition in open channels. A significant amount development is, however, still needed to facilitate simulation of the temporal development of local scour.

6.1 Application of Fluent 6.2 to local scour prediction

The general commercial CFD code Fluent 6.2 was employed to compute the flow field around the piers and abutments by solving the three-dimensional Navier-Stokes equations. The k-ε model was applied for turbulent closure as it has proven to offer a good compromise between accuracy and computational cost in many previous studies of local scour. The Volume of Fluid (VOF) model was employed for the stratified flow of air and water to simulate the free surface in an open channel. The VOF model is the recommended multiphase model for simulating open channel flows in Fluent.

Steady state simulations of the flows around piers and abutments were performed with flat and deformed channel beds and the results were compared to small-scale physical models (Ahmed, 1995; Midgely, 2000; Mitchell, 2000; Unger & Hager, 2005). Flow patterns were compared qualitatively to theory and to measurements made in the laboratory studies. To indicate the tendency of the flow to scour or deposit sediment, the Movability Number and the applied unit stream power on the channel bed were calculated from the fluid properties (viscosity) and the velocity gradients computed by the numerical model. The incipient motion of sediment from flat, unscoured channel beds at a circular pier and a rectangular abutment was thus compared to the physical models of Midgely (2000) and Mitchell

(2000) respectively. The scour predicted was also compared to an earlier numerical model in which a "moving wall" free surface routine was employed (McGahey, 2001).

The dynamic mesh adjustment capability of Fluent 6.2, which may facilitate simulation of the temporal development of scour holes, was investigated but not implemented due to time limitations. Instead, steady state simulations of flow at a circular pier (Ahmed, 1995) were undertaken and manual bed adjustments performed according to the unit stream power approach. The change in vertical elevation of the channel bed at any point was computed as a function of the scour potential at the bed. Slope correction was performed where necessary according to the relationship developed by Armitage (2002). Six adjustments were performed in total.

6.2 Modelling of free surface flow

From a qualitative assessment, the VOF model appeared to produce realistic variations of the free surface elevation at piers and abutments. This suggested that this model for open channel flow is capable of correctly reproducing the pressure field at obstacles and hence the associated effects on flow patterns and scour.

The VOF model correctly showed the rise in water level immediately upstream of the circular pier associated with stagnation of the flow. Acceleration and downflow at the pier sides was also clearly evident. With a fine mesh and the high-order QUICK discretisation scheme, an upstream-facing surface roller could be seen at the pier side. The bow wave at the stagnation point was, however, not evident in most cases. A rise in the water level in the dead water zone upstream of the rectangular abutment was clearly shown.

The implicit VOF model for steady flows in Fluent, which solves a scalar transport equation for the volume fraction of each phase in the cells, produced a smeared interface between the air and water phases. This interface can be better resolved by use of a finer mesh and higher order discretisation scheme.

To maintain the desired water depth at the upstream and downstream boundaries of the domain, it was necessary to specify these boundaries as "velocity inlet" boundaries at which point velocities were specified.

6.3 Flow patterns around obstacles and in scour holes

The numerical model for flow around piers and abutments correctly predicted the principal features of the flow responsible for scouring and showed promise for use as a tool for local scour prediction.

Numerical simulation of the Midgely (2000) experiment of flow around a circular pier with a flat, unscoured channel bed showed acceleration of the flow around the side of the pier with maximum velocities at approximately 60° to the symmetry plane where local scour would commence. Downflow at the upstream face of the pier was clearly shown and there was also evidence of the initial formation of the horseshoe vortex even in this flat bed simulation. Separation of the flow and eddies in the pier wake were also evident.

For the rectangular abutment (Mitchell, 2000), the main features of the flow could be seen in the horizontal (x-z) plane, but the flow structures in the vertical (x-y and z-y) planes responsible for scouring, such as the principal vortex, were not evident in the flat bed simulation. The dead water zone upstream of the abutment and recirculation zone and reattachment point downstream could be clearly seen. Acceleration of the flow around the tip of the abutment and constriction of the flow at, and downstream of, the abutment was also correctly computed by the model. Some downflow was evident at the upstream edge of the abutment where the principal vortex would develop with the commencement of local scouring.

Flow patterns in, and particle tracks through, the scour hole at the semi-circular abutment of Unger and Hager (2005) clearly showed a developed horseshoe vortex around the upstream face and side of the abutment. A small circulating zone near the free surface at the upstream face of the abutment also indicated the formation of a bow wave.

The flow features computed by the numerical model in both the flat bed studies of incipient motion and the developed scour hole suggested that the numerical model is able to simulate both the initiation and development of local scour holes.

6.4 Scour prediction

6.4.1 Incipient sediment motion at a cylindrical pier and a rectangular abutment

The initiation of scouring at the circular pier predicted by the numerical model according to the Movability Number and stream power approaches, agreed well with theory and compared fairly well to observations made in the physical model (Midgely, 2000). Both the Movability Number and stream power models predicted that scour would commence at points approximately 60° to the symmetry plane and indicated similar extents of the scoured region. Midgely (2000), however, measured scour not only at the pier sides but also around the upstream face of the pier.

The numerical model of the Mitchell (2000) experiment, for the initiation of scouring at a rectangular abutment, produced reasonable approximations of the scour patterns observed in the laboratory. Maximum values of the Movability Number and applied stream power were correctly computed to occur at the upstream tip of the abutment. The extent of the scoured area predicted by each of these sediment transport models was, however, in excess of that observed in the physical model. It was suggested that the numerical model overestimated the lateral extent of the recirculation zone in the abutment wake, exaggerating the constricting effects of the abutment on the flow.

6.4.2 Scour prediction in a developed scour hole at a semi-circular abutment

Although the flow field computed for the scour hole of Unger & Hager (2005) showed, from a qualitative assessment, considerable promise for scour prediction, the scour potential indicated by the Movability Number and unit stream power approaches was lower than expected. The scour hole simulated had not yet reached equilibrium in the physical

model. The numerical model, however, suggested that an equilibrium clear-water scour hole had established as the scour potential according to both sediment transport parameters was approximately zero in the flat region at the bottom of the scour hole. The stream power at this point was, in fact, less than the critical value suggesting that the numerical model would predict a shallower scour hole.

Further development of the link between flow phenomena and sediment transport is necessary for implementation of sediment transport formulae in numerical models. Although the numerical model appeared to predict realistic flow patterns, the magnitude of the applied stream power was in error. The unit stream power was very sensitive to the depth at which it was computed in the region of the channel bed.

6.5 Scour hole development using manual bed adjustment

Manual bed adjustment was performed to simulate scour and deposition at a circular pier (Ahmed, 1995) according to the unit stream power approach. This model illustrated correct initial formation of the scour hole at the side of the pier and its migration upstream to the front of the pier with subsequent adjustments. There are, however, many problems and limitations associated with the repeated computation of the flow field and manual bed adjustment to simulate the temporal development of local scour.

The applied stream power at the channel bed was lower than the critical value for incipient motion of sediment as found previously in the analysis of flow through the scour hole of Unger & Hager (2005). The critical stream power therefore had to be reduced to be meaningful for scour prediction.

Manual bed adjustment is a very tedious procedure requiring a significant amount of time to be spent on processing simulation output. Automation of the bed deformation process is necessary if the bed adjustment technique is to prove useful for local scour prediction in future.

The large changes in bed elevation (up to 5 mm) employed in manual adjustments to accelerate scour hole development, generated an uneven bed topology and slopes in excess of the sediment angle of repose. Smaller adjustments not exceeding 1 mm, for instance, and the use of an automated adjustment procedure would be more appropriate.

The mathematical form of the function relating the scour potential to the channel bed deformation requires investigation. This function should not produce increasingly uneven bed topologies with repeated bed adjustment. The simple linear relationship assumed between Δy and Ω coupled with large node movements produced unrealistic sharp peaks and troughs in the channel bed. Smoothing of the bed, achieved by averaging the vertical co-ordinate of each node with those of its neighbours, was necessary after the fourth adjustment to prevent the bed slope angles from exceeding the sediment angle of repose at many points.

Alternative formulations of the slope correction factor, which are defined for bed slopes in excess of the angle of repose, or modifications to the existing formula, require investigation. The use of a finer mesh near the channel bed and smaller adjustment increments may mitigate the slope correction problems encountered.

6.6 Limitations

The CFD software was implemented on a personal computer with a 2.8 GHz Pentium 4 processor and 2 GB RAM in a Microsoft Windows operating system. The manual bed adjustment simulations each typically took 4 hours to compute the flow field. A further 3 hours was then required after each simulation to export the numerical model output, compute the bed deformations and regenerate the bed geometry and mesh. Manual bed adjustment is clearly not a suitable approach for computing the formation of local scour holes as a considerable amount of effort is required in processing simulation output. Automated procedures are needed.

The solution times for simulation of incipient sediment motion at the rectangular abutment (Mitchell, 2000) were in the region of 24 hours when employing the QUICK discretisation

scheme and a mesh consisting of approximately 800 000 cells. The long zone of recirculation downstream of the abutment, even at modest Froude Numbers, necessitates definition of an elongated computation domain as it is undesirable to have backflow through the outflow boundary.

Memory problems were encountered when attempting to simulate flow in domains which were discretised into more than one million cells.

Chapter 7
Recommendations for Further Research

Adaptation of a general CFD code for prediction of incipient sediment motion and scour according to the unit stream power model indicated that numerical models show considerable promise for use in local scour prediction. Further work is required in several areas to improve the reliability and efficiency of the models investigated in this study.

i) Errors in the computation of Movability Numbers and the applied stream power at the channel bed must be addressed. The applied power was lower than expected in most simulations and both parameters significantly overestimated the extent of the scoured area at the rectangular abutment. Systematic errors introduced by the numerical model should be investigated and the rationale behind the choice of critical values for incipience in the sediment transport models must be examined.

ii) Although the k-ε turbulence model has been successfully applied to many similar applications, other turbulence models which better account for the features of the flow in the turbulent boundary layer near the channel bed must be investigated. Improved treatment of the boundary layer may help to reduce errors in the computed sediment transport parameters discussed in (i).

iii) Adaptation of the dynamic mesh adjustment capabilities of Fluent 6.2 for scour prediction is the next step in development of a model for temporal scour development. This model will require subroutines to which the computed solver variables (e.g. fluid viscosity and velocity gradients) are passed and functions describing the bed deformation in terms of these solver variables. Only small changes in bed elevation must be permitted at each adjustment and the functions relating scour potential to changes in bed elevation should be appropriately chosen to produce "smooth" bed topologies.

iv) Formulation of the slope correction factor for dynamic bed adjustment requires consideration. Alternative slope correction methods which still permit calculation when the slope angle exceeds the sediment angle of repose require investigation and/or development.

v) Once a working dynamic bed adjustment model has been developed, sediment transport formulae used to define bed deformation may be modified to address more complex sediment transport problems such as the scouring of cohesive sediments or non-uniform material.

vi) The Euler-Euler granular phase multiphase model available in Fluent 6.2 should be considered as another option for simulating temporal evolution of scour holes. This would obviate the need for empirical sediment transport relationships as the physics of particle motion are computed directly in the solution.

References

Ahmed, F (1995). "Flow and erosion around bridge piers." PhD thesis, University of Alberta, Canada.

Ali, KHM & O Karim (2002). "Simulation of flow around piers." *J. Hydr. Res.*, 40:2, 161 – 174.

Armitage, NP (2002). "A unit stream power model for the prediction of local scour." PhD dissertation, University of Stellenbosch, South Africa.

Armitage, NP & C McGahey (2003). "A unit stream power model for the prediction of local scour in rivers." *Water Research Commission of South Africa*, Report 1098/1/03, Pretoria, South Africa.

Armitage, NP, ME Cunninghame & A Kabir (2005). "Local scour in rivers: The extent of the problem in South Africa; The state of the art of numerical modelling." *Water Research Commission of South Africa*, Report No. 565, Pretoria, South Africa (in press).

Bagnold, RA (1966). "An approach to the sediment transport problem from general physics." *US Geological Survey Professional Paper*, 422-J, 37 pages.

Biglari, B & TW Sturm (1998). "Numerical modelling of flow around bridge abutments in compound channel." *J. Hydr. Engrg,* ASCE, 124:2, 156 – 164.

Breusers, HNC & AJ Raudkivi (1991). "Scouring." IAHR Hydraulic Structures Design Manual 2, A.A. Balkema, Netherlands.

Cellino, M & WH Graf (2000). "Experiments on suspension flow in open channels with bed forms." *J. Hydr. Engrg*, ASCE, 38:4.

Chadwick, A & J Morfett (1998). "Hydraulics in Civil and Environmental Engineering." Third Edition, E&FN SPON, London, UK.

Chanson, H (2004). "The Hydraulics of Open Channel Flow: An Introduction." Second Edition, Elsevier, Oxford, UK.

Cheng, N-S (1997). "A simplified settling velocity formula for sediment particles." *J. Hydr. Engrg*, ASCE, 123:2, 149 – 152.

Chien, N & Z Wan (1999). "Mechanics of sediment transport." ASCE Press, USA.

Chiew, Y-M & G Parker (1995). "Incipient motion on non-horizontal slopes." *J. Hydr. Res.*, 32:5, 649 – 660.

Christian, CD & PA Corney (2004). "Three dimensional model of flow over a shallow trench." *J. Hydr. Res.*, 42:1, 71 – 80.

Coles, D (1956). "The law of the wake in the turbulent boundary layer." *J. Fluid Mechanics*, 1, 191 – 226.

Cunninghame, ME (2003). "Computational Fluid dynamics modelling of scour around engineering structures in rivers." BSc(Eng) thesis, University of Cape Town, Rondebosch, South Africa.

Dargahi, B (1990). "Controlling Mechanism of Local Scouring." *J. Hydr. Engrg*, ASCE, 116:10, 1197 – 1214.

Dey, S, SK Bose & GLN Sastry (1995). "Clear Water Scour at Circular Piers: A Model." *J. Hydr. Engrg*, ASCE, 121:12, 869 – 876.

Dey, S & AK Barbhuiya (2004). "Clear-Water Scour at Abutments in Thinly Armoured Beds." *J. Hydr. Engrg*, ASCE, 130:7, 622 – 634.

Einstein, HA (1942). "Formulae for transportation of bedload." *Trans. ASCE*, 107, 561 – 577. In Raudkivi, 1998.

Engelund, F & E Hansen (1967). "A monograph on sediment transport in alluvial streams." *Tekisk Forlag*, Copenhagen. In Raudkivi, 1998.

Ettema, R (1980). "Scour at bridge piers." Univ. of Auckland, New Zealand, School of Engineering, Report No. 216. In Raudkivi, 1998.

Featherstone, RE & C Nalluri (1995). "Civil Engineering Hydraulics." Third Edition, Blackwell Science Limited, UK.

Fluent (2005). "Fluent Users' Guide." Fluent Inc., UK.

Graf, WH (1998). "Fluvial Hydraulics: Flow and transport processes in channels of simple geometry." John Wiley & Sons, UK.

Graf, WH & I Istiarto (2002). "Flow pattern in the scour hole around a cylinder." *J. Hydr. Res.*, 40:1, 13 – 20.

Grass, AJ (1970). "Initial instability of fine bed sand." *J. Hydr. Div.*, ASCE, 96:HY3, 619 – 632.

Hinze, JD (1962). "Turbulent pipe flow." *Mechanique de la Turbulence*, 108, Editions du Centre National de la Recherché Scientifique, Paris, France, 129 – 165.

Hirt, CW & BD Nichols (1981). "Volume of fluid (VOF) method for the dynamics of free boundaries." *J. of Computational Physics*, 39, 201 – 225.

Hjulstrom, F (1935). "The morphological activity of rivers as illustrated by River Fyris." *Bulletin of the Geological Institute*, Uppsala, 25:3. In Yang, 1996.

Hoffmans, GJCM. & HJ Verheij (1997). "Scour Manual", A.A. Balkema, Netherlands.

Johnson, PA (1995). "Comparison of pier-scour equations using field data." *J. Hydr. Engrg*, ASCE, 121:8, 626 – 629.

Julien, PY (1995). "Erosion and sedimentation." Cambridge University Press.

Kajikawa, Y, M Michiue, Y Matsubara, O Hinokidani & H Nakamoto (2004). "Numerical simulation of complex flow over backward-facing step." *J. Hydroscience & Hydraulic Engineering*, 22:2, 11 – 24.

Karim, OA & KHM Ali (2000). "Prediction of flow patterns in local scour holes caused by turbulent water jets." *J. Hydr. Res.*, 38:4, 279 – 287.

Komura, S (1966). "Equilibrium depth of scouring in long constrictions." *J. Hydr. Div.*, ASCE, 86:HY5, 17 – 37.

Kwan, TF (1984). "Study of abutment scour." University of Auckland, Department of Civil Engineering, Report No.328. In Breusers & Raudkivi, 1991.

Launder, BE & DB Spalding (1972). "Lectures in mathematical models of turbulence." Academic Press, London, England.

Liang, D & L Cheng (2005). "Numerical modelling of flow and scour below a pipeline in currents. Part I: Flow simulation." *J. Coastal Engrg.*, 52(2005), 25 – 42.

Liang, D, L Cheng & F Li (2005). "Numerical modelling of flow and scour below a pipeline in currents. Part II: Scour simulation." *J. Coastal Engrg.*, 52(2005), 43 - 62.

Lim, S-Y & N-S Cheng (1998). "Scouring in long contractions." *J. Irrig. & Drainage Engrg.*, ASCE, 124:5, 258 – 261.

Liu, H-K (1957). "Mechanics of Sediment-Ripple Formation." *J. Hydr. Div.*, ASCE, 84:HY5, 1197-1 – 1197-23.

Lysne, DK (1969). "Movement of sand in tunnels." *J. Hydr Engrg*, ASCE, 95:6, 1835 - 1846.

M^{c}Gahey, C (2001). "A computational fluid dynamics model for sediment movement based on the unit stream power approach." MSc(Eng) dissertation, University of Cape Town, South Africa.

Melville, BW (1992). "Local scour at bridge abutments." *J. Hydr. Engrg*, ASCE, 118:4, 615 – 631.

Melville, BW (1997). "Pier and Abutment Scour: An Integrated Approach." *J. Hydr. Engrg, ASCE*, 123:2, 125 – 137.

Midgely, M (2000). "Sediment movement around piers in open channel flow." BSc(Eng) thesis, University of Cape Town, Rondebosch, South Africa.

Migniot, C (1968). "Etude des Proprietes Physiques de Differents Sediments Tres Fins et de Leur Comportement Sous des Actions Hydrodynamiques." *Houille Blanche*, 7, 591 – 620. In Chien & Wan, 1999.

Mitchell, A (2000). "Sediment transport around abutments in open channel flow." BSc(Eng) thesis, University of Cape Town, Rondebosch, South Africa.

Nagata, N, T Hosada, T Nakato, Y Muramoto (2002). "3D Numerical simulation of flow and local scour around a cylindrical pier." *J. Hydroscience & Hydraulic Engineering*, 20:1, 113 – 125.

Nikuradse, J (1933). "Stromungsgesetze in Rauben Rohren (Laws of turbulent pipe flow in rough pipes)." *VDI, Forschungsheft*, No. 361. In German; translated in NACA Tach. Memo No. 1292, 1950.

Olsen, NRB & MC Melaaen (1993). "Three-dimensional calculation of scour around cylinders." *J. Hydr Engrg*, ASCE, 119:9, 1048 – 1054.

Olsen, NRB & HM Kjellesvig (1998). "Three-dimensional numerical flow modelling for estimation of maximum local scour depth." *J. Hydr. Res.*, 36:4, 579 – 590.

Ouillon, S & D Dartus (1997). "Three-dimensional computation of flow around groyne." *J. Hydr. Engrg*, ASCE, 123:11, 962 – 970.

Patankar, SV (1980). "Numerical heat transfer and fluid flow." Taylor & Francis, UK.

Potter, MC & DC Wiggert (1997). "Mechanics of fluids." Second edition, Prentice Hall.

Prandtl, L (1925). "Uber die Ausgebildete Turbulenz." (On fully developed turbulence.) *Z.A.M.M.*, 5, 136 – 139 (in German). In McGahey, 2001.

Rameshwaran, P & PS Naden (2004). "Three-dimensional modelling of free surface variation in a meandering channel." *J. Hydr. Res.*, 42:6, 603 – 615.

Raudkivi, AJ (1986). "Functional trends of scour at bridge piers." *J. Hydr. Engrg*, ASCE, 112, 1 – 13.

Raudkivi, AJ (1998). "Loose Boundary Hydraulics." Fourth Edition, A.A. Balkema, Rotterdam, Netherlands.

Richardson, JE & VG Panchang (1998). "Three-dimensional simulation of scour-inducing flow at bridge piers." *J. Hydr. Engrg*, ASCE, 124:5, 530 – 540.

Rodi, W (1984). "Turbulence models and their application in hydraulics." State of the art review, second edition revised, *IAHR Section on Fundamentals of Division II: Experimental and Mathematical Fluid Dynamics*, Rotterdam, Netherlands.

Rooseboom, A. (1975). "Sediment Transport in Rivers and Reservoirs", D.Eng dissertation, University of Pretoria, South Africa.

Rooseboom, A & FJ Mülke (1982). "Erosion initiation." *Proc. Exeter Symposium*, July 1982, IAHS Publ. No. 137.

Rooseboom, A. (1992). "Sediment Transport in Rivers and Reservoirs – A Southern African Perspective." Report No. 297/1/92 of the Water Research Commission of South Africa.

Salaheldin, TM, J Imran & MH Chaudhry (2004). "Numerical modelling of three-dimensional flow field around circular piers." *J. Hydr. Engrg*, ASCE, 130:2, 91 – 100.

Salehi Neyshabouri, AA, AM Ferreira da Silva & R Barron (2003). "Numerical simulation of scour by a free falling jet." *J. Hydr. Res.*, 41:5, 533 – 539.

Schlichting, H (1979). "Boundary layer theory." Seventh edition, Mc Graw-Hill Inc., United States of America.

Schlichting, H & K Gersten (2000). "Boundary Layer Theory." Eighth edition, Springer-Verlag, Berlin, Germany.

Shields, A (1936). "Anwendung der Aenlichkeitsmechanik und der Turbulenzforschung auf die Geschiebebewegung." *Mitteilungen der Preussischen Versuchsanstalt für Wasserbau und Schiffbau*, Heft 26 (in German). English translation by WP Ott and JC van Uchelen, Hydrodynamics Laboratory Publication No. 167, Hydrodynamics Lab., California Institute of Technology, Pasadena.

Shvidchenko, AB & G Pender (2000a). "Flume study of the effect of relative depth on the incipient motion of coarse uniform sediments." *Water Resources Research*, 36:2, 619 – 628. In Armitage, 2002.

Shvidchenko, AB & G Pender (2000b). "Initial motion of streambeds composed of coarse uniform sediments." *Proc. Instn Civ. Engrs Water & Mar. Engrg*, 142, 217 – 227. In Armitage,2002.

Simons, DB & F Senturk (1977). "Sediment transport technology." US Water Resources Publications, Fort Collins, Colorado.

Tingsanchali, T & S Maheswaran (1990). "2-D Depth-Averaged Flow Computation near Groyne." *J. Hydr Engrg*, ASCE, 116:1, 71 – 86.

Unger, J & WH Hager (2005). "Spatial and temporal scour features of circular bridge piers." Paper submitted to XXXI IAHR Congress, September 2005, Seoul, Korea.

Van Rijn, LC (1993). "Principles of sediment transport in rivers, estuaries and coastal seas." Aqua Publications, Netherlands.

Vanoni, VA (Ed.) (1977). "Sedimentation Engineering." ASCE Manuals and Reports on Engineering Practice No. 54, *ASCE*, New York, USA.

Versteeg, HK & W Malalasekera (1995). "An Introduction to Computational Fluid Dynamics: The Finite Volume Method." Longman Group Limited, Essex, UK.

White, FM (1991). "Viscous Fluid Flow." Second edition, McGraw-Hill Inc., New York.

Yalin, MS (1972). "Mechanics of Sediment Transport." Pergamon Press, Oxford, UK.

Yalin, MS & AM Ferreira da Silva (2001). "Fluvial Processes." International Association of Hydraulic Engineering and Research Monograph, IAHR, Delft, Netherlands.

Yang, CT (1972). "Unit stream power and sediment transport." *J. Hydr. Div.*, ASCE, 98:HY10, 1805 – 1826.

Yang, CT (1973). "Incipient motion and sediment transport." *J. Hydr. Div.*, ASCE, 99:HY10, 1679 – 1703.

Yang, CT & JB Stall (1976). "Applicability of Unit Stream Power Equation." *J. Hydr. Div.*, ASCE, 102:HY5, 559 – 568.

Yang, CT & CCS Song (1979). "Theory of minimum rate of energy dissipation." *J. Hydr. Div.*, ASCE, 105:HY7, 769 – 784.

Yang, CT (1996). "Sediment Transport: Theory and Practice." McGraw-Hill, Singapore.

Appendix
Controls for Manual Bed Adjustment

Controls for Manual Bed Adjustment

Table A1: Controls for bed adjustment 1

Critical stream power, P_{tcr0} (W/m^3)	5.0
Critical scour potential, $\Omega_{cr,scour}$ (W/m^3)	0.0
Critical deposition potential, $\Omega_{cr,depo}$ (W/m^3)	-4.2
Relaxation factor for deposition, C_{scour} (m^4/W)	0.0004
Relaxation factor for scouring, C_{depo} (m^4/W)	0.0063
Bed adjustment function	$\Delta y \propto \Omega$
Number of nodes at which scour occurs, N_{scour}	83
Number of nodes at which deposition occurs, N_{depo}	66
Total number of nodes moving, N_{total}	149
Maximum scour, $\Delta y_{scour,max}$ (mm)	-5.0
Maximum deposition, $\Delta y_{depo,max}$ (mm)	4.4
Minimum bed elevation, $y_{bed,min}$ (mm)	-5.0
Maximum bed elevation, $y_{bed,max}$ (mm)	+4.4
Number of points where abs(β) > ϕ	0
Number of points where abs(γ) > ϕ	0
Number of points where ψ is undefined	0

Table A2: Controls for bed adjustment 2

Critical stream power, P_{tcr0} (W/m^3)	6.0
Critical scour potential, $\Omega_{cr,scour}$ (W/m^3)	0.0
Critical deposition potential, $\Omega_{cr,depo}$ (W/m^3)	-4.8
Relaxation factor for deposition, C_{scour} (m^4/W)	0.0004
Relaxation factor for scouring, C_{depo} (m^4/W)	0.0016
Bed adjustment function	$\Delta y \propto \Omega$
Number of nodes at which scour occurs, N_{scour}	80
Number of nodes at which deposition occurs, N_{depo}	78
Total number of nodes moving, N_{total}	158
Maximum scour, $\Delta y_{scour,max}$ (mm)	-5.0
Maximum deposition, $\Delta y_{depo,max}$ (mm)	7.9
Minimum bed elevation, $y_{bed,min}$ (mm)	-9.3
Maximum bed elevation, $y_{bed,max}$ (mm)	+12.1
Number of points where abs(β) > ϕ	3
Number of points where abs(γ) > ϕ	0
Number of points where ψ is undefined	3

Table A3: Controls for bed adjustment 3

Critical stream power, P_{tcr0} (W/m^3)	6.0
Critical scour potential, $\Omega_{cr,scour}$ (W/m^3)	0.0
Critical deposition potential, $\Omega_{cr,depo}$ (W/m^3)	-4.8
Relaxation factor for deposition, C_{scour} (m^4/W)	0.0005
Relaxation factor for scouring, C_{depo} (m^4/W)	0.0007
Bed adjustment function	$\Delta y \propto \Omega$
Number of nodes at which scour occurs, N_{scour}	85
Number of nodes at which deposition occurs, N_{depo}	49
Total number of nodes moving, N_{total}	134
Maximum scour, $\Delta y_{scour,max}$ (mm)	-5.0
Maximum deposition, $\Delta y_{depo,max}$ (mm)	5.0
Minimum bed elevation, $y_{bed,min}$ (mm)	-13.9
Maximum bed elevation, $y_{bed,max}$ (mm)	+14.8
Number of points where abs(β) > ϕ	3
Number of points where abs(γ) > ϕ	14
Number of points where ψ is undefined	16

Table A4: Controls for bed adjustment 4

Critical stream power, P_{tcr0} (W/m^3)	5.0
Critical scour potential, $\Omega_{cr,scour}$ (W/m^3)	0.0
Critical deposition potential, $\Omega_{cr,depo}$ (W/m^3)	-3.9
Relaxation factor for deposition, C_{scour} (m^4/W)	0.0005
Relaxation factor for scouring, C_{depo} (m^4/W)	0.0009
Bed adjustment function	$\Delta y \propto \Omega$
Number of nodes at which scour occurs, N_{scour}	96
Number of nodes at which deposition occurs, N_{depo}	53
Total number of nodes moving, N_{total}	149
Maximum scour, $\Delta y_{scour,max}$ (mm)	-5.0
Maximum deposition, $\Delta y_{depo,max}$ (mm)	5.0
Minimum bed elevation, $y_{bed,min}$ (mm)	-14.8
Maximum bed elevation, $y_{bed,max}$ (mm)	+13.2
Number of points where abs(β) > ϕ	5
Number of points where abs(γ) > ϕ	23
Number of points where ψ is undefined	28

Table A5: Controls for bed adjustment 5

Critical stream power, P_{tcr0} (W/m^3)	3.0
Critical scour potential, $\Omega_{cr,scour}$ (W/m^3)	0.0
Critical deposition potential, $\Omega_{cr,depo}$ (W/m^3)	-1.8
Relaxation factor for deposition, C_{scour} (m^4/W)	0.0016
Relaxation factor for scouring, C_{depo} (m^4/W)	0.0026
Bed adjustment function	$\Delta y \propto \sqrt{\Omega}$
Number of nodes at which scour occurs, N_{scour}	155
Number of nodes at which deposition occurs, N_{depo}	59
Total number of nodes moving, N_{total}	214
Maximum scour, $\Delta y_{scour,max}$ (mm)	-5.0
Maximum deposition, $\Delta y_{depo,max}$ (mm)	5.0
Minimum bed elevation, $y_{bed,min}$ (mm)	-18.5
Maximum bed elevation, $y_{bed,max}$ (mm)	+14.6
Number of points where abs(β) > ϕ	6
Number of points where abs(γ) > ϕ	16
Number of points where ψ is undefined	24

Table A6: Controls for bed adjustment 6

Critical stream power, P_{tcr0} (W/m^3)	3.0
Critical scour potential, $\Omega_{cr,scour}$ (W/m^3)	0.0
Critical deposition potential, $\Omega_{cr,depo}$ (W/m^3)	-1.9
Relaxation factor for deposition, C_{scour} (m^4/W)	0.0014
Relaxation factor for scouring, C_{depo} (m^4/W)	0.0026
Bed adjustment function	$\Delta y \propto \sqrt{\Omega}$
Number of nodes at which scour occurs, N_{scour}	154
Number of nodes at which deposition occurs, N_{depo}	48
Total number of nodes moving, N_{total}	202
Maximum scour, $\Delta y_{scour,max}$ (mm)	-5.0
Maximum deposition, $\Delta y_{depo,max}$ (mm)	5.0
Minimum bed elevation, $y_{bed,min}$ (mm)	-21.4
Maximum bed elevation, $y_{bed,max}$ (mm)	+15.0
Number of points where abs(β) > ϕ	7
Number of points where abs(γ) > ϕ	34
Number of points where ψ is undefined	40